ABSTRACT

Title of Dissertation:	ADVANCEMENT OF MOIRÉ INTERFEROMETRY FOR RATE-DEPENDENT MATERIAL BEHAVIOR AND MICROMECHANICAL DEFORMATIONS
	Bulong Wu, Doctor of Philosophy, 2018
Dissertation directed by:	Professor Bongtae Han Department of Mechanical Engineering

Moiré interferometry is an optical technique to map full field in-plane deformations with extremely high resolution and signal to noise ratio. The technique is advanced and implemented to study the rate-dependent thermo-mechanical behavior of Sn-based Pb-free solder alloys and micromechanical deformations.

In Part I, the mechanical/optical configuration of moiré interferometry for real-time observation of thermal deformations is enhanced to provide measurement capabilities required for the analyses. Two most notable advancements are (1) development of a conduction-based thermal chamber for a wide range of ramp rates with accurate temperature control, and (2) implementation of microscope objectives in the imaging system to observe a microscopic field of view. The advanced system is implemented to analyze the anisotropic behavior of Sn-based Pb-free solder alloys. A novel copper-steel specimen frame is developed to apply a controlled loading to single-grain solder joints. After measuring the grain orientation by electron backscatter

diffraction (EBSD), detailed in-situ deformation evolutions and accumulated deformations of solder alloys are documented during a thermal cycle of -40 °C to 125 °C. The results quantify grain orientation-dependent deformations that can lead more accurate anisotropic constitutive properties of Sn-based Pb-free solder alloys.

In Part II, an advanced immersion microscopic moiré interferometry system based on an achromatic configuration is developed and implemented for higher displacement sensitivity and spatial resolution. In order to achieve the desired displacement resolution, a high frequency grating (2500 lines/mm) is fabricated on a silicon substrate using lithography first. The square profile is subsequently modified by reactive-ion etching so that it can be used to produce a specimen grating by replication. Secondly, the algorithm of the optical/digital fringe multiplication method is improved to further enhance the measurement resolution of the immersion microscopic moiré interferometry. The system and the noise-free grating are used to analyze thermal deformations of micro-solder bumps. With the basic contour interval of 200 nm, the displacement resolution of 25 nm is achieved with the multiplication factor of 8.

ADVANCEMENT OF MOIRÉ INTERFEROMETRY FOR RATE-DEPENDENT MATERIAL BEHAVIOR AND MICROMECHANICAL DEFORMATIONS

By

Bulong Wu

Dissertation submitted to the Faculty of the Graduate School of the
University of Maryland, College Park, in partial fulfillment
of the requirements for the degree of
Doctor of Philosophy
2018

Advisory Committee:
Professor Bongtae Han, Chair/Advisor
Professor Abhijit Dasgupta
Professor F. Patrick McCluskey
Professor Miao Yu
Professor Sung Lee, Dean's Representative

© Copyright by

Bulong Wu

2018

Dedication

To

My father Mr. Zaigong Wu, my mother Mrs. Saiping Jiang, my brother Bufei Wu and sister Ai'xia Wu for all their support and love; and

My beloved wife, Wenjuan Zou, for her persistence, love and faith in me

Acknowledgements

I would like to express my deepest and sincere gratitude to my advisor Prof. Bongtae Han for giving me an opportunity to work with him and teaching me to be better not only in research but also in life. His advice focuses on logical thinking and "details" other than solution itself has been one of the most invaluable training I have gained. He spent a lot of time on me that I can't imagine during my PhD journey. His endless energy keeps inspiring me to tackle the difficulties that I encountered. My vocabulary is not enough to express my gratitude to Prof. Han for his support.

I would like to thank Prof. Abhijit Dasgupta, Prof. F. Patrick McCluskey, Prof. Miao Yu and Prof. Sung Lee for serving in my dissertation committee. I thank them for providing valuable guidance for my research and being very responsive to my dissertation needs despite of having their own busy schedules.

I would like to thank our wonderful LOMSS members: Yong, Dae-Suk, Kenny, Sean, Byung, Michelle, Bong-Min, Hyun-Seop, Jack, Ryan and Artur. Thank you for all your support and help. I would also like to thank Qian Jiang, Dengyun Chen, Jingshi Meng, Fei Chai, Wei He, Hao Huang, Abhishek and other CALCE members.

I would like to thank Dr. Sarah Penniston-Dorland from department of Geology, Mark Lecates from nanocenter FabLAB and Dr. Joshua Schumacher from NIST for their technical support and providing valuable inputs into my dissertation.

Finally, I would like to express my gratitude to my family. I am grateful to my parents, brother, sister and my parents-in-law for their endless support. My most heartfelt thanks go to my beloved wife, Wenjuan Zou, for her persistence, support and endless love. I love you all!

Table of Contents

Dedication ii

Acknowledgements iii

Table of Contents iv

List of Tables vii

List of Figures viii

Chapter 1 Introduction 1

- 1.1. Motivation and Objectives 1
- 1.2. Organization of Dissertation 3

Part I: Advancement of Moiré Interferometry for Rate-dependent Material Behavior 7

Chapter 2 Advanced Mechanical/Optical Configuration of Real-time Moiré Interferometry for Thermal Deformation Analysis of Fan-out Wafer Level Package 8

- 2.1. Introduction 8
- 2.2. Current Practice of Moiré Interferometry 10
  - 2.2.1. Principle of Moiré Interferometry 10
  - 2.2.2. Current Practice for Real-time Observation 11
- 2.3. Advancements of Real-time Moiré Interferometry 12
  - 2.3.1. Thermal Loading Chamber 12
  - 2.3.2. Imaging System Using Microscope Objectives 19
- 2.4. Thermo-mechanical Behavior of Fan-out Wafer Level Package 22
  - 2.4.1. Specimen Preparation 22
  - 2.4.2. Moiré Experiment and Results 23
- 2.5. Discussion: Effect of the Reworkable Underfill 31
- 2.6. Conclusion 32

Chapter 3 Measurement of Anisotropic Coefficients of Thermal Expansion of Single SAC305 Solder Grain 33

3.1. Introduction 33
3.2. Theoretical Derivation 35
3.2.1. Relationship between CTE Values and Surface Strains 35
3.2.2. Determination of Anisotropic CTE Values from Surface Strains 37
3.3. CTE Measurements 39
3.3.1. Experimental Method: Moiré Interferometry 40
3.3.2. Specimen Preparation: Solder Specimen with a Single Grain 42
3.3.3. Displacement Fields and CTE Values 44
3.4. Discussion: Grain Orientation 49
3.5. Conclusion 51

Chapter 4 Experimental Study of a Single SAC305 Grain Deformation under Thermo-Mechanical Loading 53

4.1. Introduction 53
4.2. Moiré Interferometry for Real-Time Deformation Observation 55
4.3. Specimen Design and Fabrication 56
4.3.1. Specimen Configuration 56
4.3.2. Specimen Fabrication 60
4.4. Moiré Experiments and Result Analyses 68
4.4.1. Moiré Experiment 68
4.4.2. Experimental Results and Analyses 70
4.5. Discussion 82
4.6. Conclusion 85

Part II: Advancement for Experimental Analyses of Micromechanical Deformations 87

Chapter 5 Advanced Immersion Microscopic Moiré Interferometer 88

5.1. Introduction 88
5.2. Principle of Immersion MMI and Limitations of Current MMI System 89
5.2.1. Principle and Implementation of Immersion MMI 89

5.2.2. Limitations of the current MMI system 91
5.3. Development of Advanced Immersion MMI 93
5.3.1. Optical Configuration 93
5.3.2. Optical and Mechanical Assembly 97
5.3.3. Mechanism of Fringe Phase Shifting Device 98
5.4. Bi-thermal Loading Experimental Procedure 103
5.5. Discussion 105
5.6. Application: Experimental Analysis of Redistribution Layer (RDL) Deformation in FO-WLP 106
5.6.1. Experiment and Results 107
5.7. Conclusion 110

Chapter 6 Fabrication of High Quality Grating and Improvement of O/DFM Algorithms for High Displacement Resolution 111

6.1. Introduction 111
6.2. Fabrication of High Quality Specimen Grating 111
6.3. Improved O/DFM Algorithms 116
6.3.1. O/DFM with $\beta = 2$ 117
6.3.2. O/DFM with $\beta = 2^m$ 118
6.4. Application: Thermo-mechanical Deformation of Solder Bumps in a Server Processor 121
6.5. Conclusion 126

Chapter 7 Contributions and Future Works 127

7.1. Dissertation Contributions 127
7.2. Future Works 128

Appendix I: Fringe Evolutions during Thermal Cycles 130

Appendix II: Constitutive Properties of SAC305 Solder 144

References 148

List of Tables

Table 3-1 Engineering strains obtained from fringe patterns of specimen 1 47

Table 3-2 Engineering strains obtained from fringe patterns of specimen 2 47

Table 3-3 Euler angles 47

Table 3-5 CTE values obtained from specimen 1 47

Table 3-6 CTE values obtained from specimen 2 48

Table 4-1 Material properties of AISI 1081 steel and OFC 101 Cu 58

Table 4-2 Isotropic material properties of SAC305 59

Table 4-3 Orthotropic elastic constants (components of stiffness tensor) of β-Sn crystal (unit: GPa) 84

Table 4-4 Transverse isotropic CTE values of SAC305 grain 84

Table II-1 Anand Model Constants 146

Table II-2 Plastic model constants for SAC305 $\tau = C_{pl} \gamma_{pl}{}^{n}$ [60] 146

Table II-3 Generalized exponential primary creep model constants for SAC305[33] 147

Table II-4 Garofalo secondary creep model constants for SAC305 147

Table II-5 Anand model constants for SAC305 147

List of Figures

Figure 2-1 Configuration of typical FO-WLP 8

Figure 2-2 Schematic illustration of the convection-based real-time moiré setup 12

Figure 2-3 (a) 3D view of chamber, (b) side view of the circled area in (a), and (c) thermal head 14

Figure 2-4 Temperature control setup using a continuous voltage............................ 16

Figure 2-5 A circuit designed to control the N-MOSFET at the high side of the H-bridge 17

Figure 2-6 Temperature loadings provided by the conduction chamber: (a) temperature profile with a ramp rate of 0.2 °C/sec, and (b) temperature variation at the steady state 18

Figure 2-7 Definition of numerical aperture.. 20

Figure 2-8 Illustration of the effect of out-of-plane displacements at the material interface 20

Figure 2-9 Fixture to accommodate microscope objectives; the objectives can be switched by rotating the lever. 21

Figure 2-10 Schematic illustration of the complete system with two cameras; use of the objective is illustrated in the figure. 21

Figure 2-11 Cross sections of the PoP specimens: (a) without underfill and (b) with underfill 23

Figure 2-12 Automatic shutter control for capturing the *U* and *V* field fringe patterns 24

Figure 2-13 Global deformation of PoP packages with and without underfill........... 25

Figure 2-14 Deformed configurations: (a) at -20 °C and (b) at 125 °C. Dashed lines represent the undeformed configurations 26

Figure 2-15 Bending displacements with and without underfill, caused by heating the specimen from - 20°C to 125°C (ΔT = 145 °C), are compared: along (a) the PCB centerline, (b) the FO-WLP centerline, and (c) the centerline of WB-BGA 28

Figure 2-16 Illustration of O/DFM with $\beta = 4$ 29

Figure 2-17 Fringe patterns of solder balls (#4 and #19) at: (a) -20 °C and (b) 125 °C. The contour interval is 104 nm per fringe 30

Figure 2-18 Average shear strains of solder balls.. 30

Figure 3-1 Illustration of β-Sn crystal structure... 33

Figure 3-2 Solder specimen coordinate (*o-xyz*) and grain coordinate (*o-x'y'z'*) 35

Figure 3-3 Coordinate transformation 36

Figure 3-4 Schematic illustration of (a) the principles of moiré interferometry and (b) the optical/mechanical configuration of an advanced portable moiré system 41

Figure 3-5 Solder specimen fabrication procedures 43

Figure 3-6 Solder reflow profile 43

Figure 3-7 Six surfaces of a specimen under the polarizing microscope ensuing a single grain 44

Figure 3-8 Moiré fringe patterns obtained from two surfaces of Specimen 1, where the counter interval is 417 nm/fringe: (a) on the *xy* plane; (b) on the *yz* plane................. 45

Figure 3-9 Moiré fringe patterns obtained from two surfaces of Specimen 2, where the counter interval is 417 nm/fringe: (a) on the *xy* plane; (b) on the *yz* plane................. 46

Figure 3-10 Comparison of anisotropic CTE values 49

Figure 3-11 Principle angles and grain orientation 50

Figure 3-12 EBSD result for specimen 1 on surface 1: (a) EBSD layered image, and (b) grain orientation 51

Figure 4-1 Schematic illustration of the optical/mechanical configuration of advanced portable moiré system 56

Figure 4-2 Solder specimen configuration 58

Figure 4-3 Schematic of specimen deformation under thermal loading ΔT 58

Figure 4-4 A quarter model for copper-steel specimen 59

Figure 4-5 Stress distribution of solder joint in copper-steel frame: (a) shear stress and (b) stress components along line AA' 60

Figure 4-6 Specimen fabrication procedures 61

Figure 4-7 Manual soldering procedure 62

Figure 4-8 Number of grain on SAC305 solder joints under polarizing microscope made at different cooling rates: (a) 25 °C/sec, (b) 3.5 °C/sec, (c) 0.8 °C/sec and (d) 0.1 °C/min 63

Figure 4-9 Specimen temperature during manual soldering process 64

Figure 4-10 Number of grains on the surfaces of solder joints under polarizing microscope: (a) specimen 1 and (b) specimen 2 65

Figure 4-11 Microstructure on the surface of solder joint #1 66

Figure 4-12 Schematic of EBSD measurement for grain orientation 67

Figure 4-13 EBSD layered images and grain orientations for solder joints: (a) #1, (b) #2, (c) #3 and (d) #4 68

Figure 4-14 Transformation from specimen coordinate to grain coordinate using Euler angles 68
Figure 4-15 Solder specimen inside conduction chamber 69
Figure 4-16 Temperature profile of thermal cycling loading applied on specimen ... 70
Figure 4-17 Representative fringe patterns of specimen 1 captured during the 1st cycle by zoom lens: (a) whole field, and (b) local solder joint and adjacent area 72
Figure 4-18 Representative fringe patterns of specimen 2 captured during the 1st cycle by zoom lens: (a) whole field, and (b) local solder joint and adjacent area 73
Figure 4-19 Fringe pattern evolution of solder joints during the six thermal cycles at 125 °C: (a) #1, (b) #2, (c) #3 and (d) #4 74
Figure 4-20 Fringe pattern evolution of solder joints during the six thermal cycles at -40 °C: (a) #1, (b) #2, (c) #3 and (d) #4 75
Figure 4-21 Fringe pattern evolution of solder joints after each cycle at 20 °C: (a) #1, (b) #2, (c) #3 and (d) #4 76
Figure 4-22 u_x displacement evolution of the solder joint #1 during each cycle at: 20 °C (a) (b), and 125 °C (c) (d) 79
Figure 4-23 Deformed configurations (X25) of solder joint # 1 recorded at different cycles: (a) at 125 °C and (b) at -40 °C 79
Figure 4-24 Displacements for each solder joint at 20 °C after the 6th thermal cycle: (a) #1, (b) #2, (c) #3 and (d) #4 80
Figure 4-25 Strains for each solder joint at 20 C after the 6th thermal cycle: (a) #1, (b) #2, (c) #2 and (d) #4 81

Figure 4-26 Deformed configurations (X25) of solder joints at 20 °C after thermal cycling: (a) #1, (b) #2, (c) #3 and (d) #4 82

Figure 4-27 FEA model and grain coordinate 84

Figure 4-28 FEA results of deformations at 125 C: displacements of upper joint (a) and lower joint (b), strains of upper joint (c) and lower joint (d) 85

Figure 5-1 Implementation of immersion interferometer [41, 66]: (a) Optical configuration, (b) four-beam immersion interferometer 91

Figure 5-2 Intensity of phase shifted fringe patterns with $\beta = 6$ [41] 91

Figure 5-3 Specimen gratings with a small angle error 92

Figure 5-4 Optical configuration of enhanced MMI 93

Figure 5-5 Diagram of light path 94

Figure 5-6 Mirror tilting angle vs specimen grating 96

Figure 5-7 Enhanced MMI assembly: (a) optical and mechanical configurations, (b) components inside MMI and light path 98

Figure 5-8 Schematics of phase shifting device (a) and its cross section (b) 99

Figure 5-9 Explanation for phase shifting mechanism: (a) Optical path length, (b) phase change for diffracted beam in $-m^{th}$ order 101

Figure 5-10 Specimen replication for bi-thermal loading experiment 103

Figure 5-11 New specimen grating replication procedure 105

Figure 5-12 Intensity distribution for interference with different light sources: (a) light source with a single wavelength: $\lambda_0 = 514$ nm, $\lambda_1 = 504$ nm, $\lambda_2 = 524$ nm; (b) laser diode: $\lambda = 514 \pm 10$ nm; (c) ion laser: $\lambda = 514 \pm 0.02$ nm 106

Figure 5-13 RDL structure in FO-WLP PoP specimen: (a) PoP Specimen cross section and area of interest, and (b) RDL microstructure 107

Figure 5-14 Fringe patterns for RDL layer with contour interval 26 nm/fringe: (a) #1, (b) #2, (c) #3, and (d) #4 108

Figure 5-15 Deformed configuration of RDL layer (RDL deformation magnified X100): (a) at die and EMC material interface area, and (b) at site #3 and #4 109

Figure 6-1 Comparison of fringe patterns: (a) an ideal fringe pattern and gray level distribution, (b) fringe pattern from photoresist grating and gray level distribution 112

Figure 6-2 Silicon grating and SEM image 113

Figure 6-3 Silicon grating: (a) fringe pattern and (b) gray level distribution 113

Figure 6-4 Silicon SEM images after etching for: (a) 1 min, (b) 2 min and (c) 4 min 114

Figure 6-5 Silicon grating after etching for 4 min: (a) fringe pattern (b) gray level distribution 114

Figure 6-6 Intensity distributions after O/DFM processing for fringe patterns with different optical noise levels: (a) zero noise, (b) low, and (c) high 121

Figure 6-7 Structure of a server processor: (a) package before and after cutting, (b) cross sections and target corner bump, and (c) specimen grating on the cross section 122

Figure 6-8 Global fringe patterns captured at 100 °C: (a) *U* field and (b) *V* field (contour interval: 417 nm/fringe)... 123

Figure 6-9 Fringe patterns at corner solder bump area: (a) original (417 nm/fringe), (b) O/DFM 2 (208 nm/fringe), (c) O/DFM 8 (52 nm/fringe)... 124

Figure 6-10 Fringe pattern captured in MMI system: (a) original (200 nm/fringe), (b) O/DFM 2 (100 nm/fringe), (c) O/DFM 4 (50 nm/fringe), and (d) O/DFM 8 (25 nm/fringe) 125

Chapter 1 Introduction

1.1. Motivation and Objectives

Miniaturization for portability but better performance and more functionality have been driving the semiconductor packaging industry for the last decade. Yet, the solder remains one of the most important materials for the package interconnection, and its reliability is still one of the major concerns. Since Pb was banned for the majority of manufactured electronics, hypoeutectic Pb-free solder, such as Sn3.0Ag0.5Cu (SAC305) and Sn1.0Ag0.5Cu (SAC105) solder alloys, have been widely accepted because they are cost-effective and offer performance like ternary near-eutectic SAC387 solder alloy [1]. Its mechanical behavior is quite different from the traditional eutectic Sn63Pb37 solder. The Sn63Pb37 solder contains soft islands of Pb embedded in Sn matrix [1], and it has been treated as a homogenous material with isotropic properties for stress analyses since its grain size is relatively small [2, 3]. However, hypo-eutectic SAC305 solder alloy contains 96.5% tin (Sn) material and intermetallic compounds (IMCs) of Ag_3Sn and Cu_6Sn_5 disperse around β-Sn grain matrix. β-Sn grains in SAC solders are large, and some solder joints of surface-mount components contain only one or a few grains [1, 4-10]. Sn crystal has a body-central tetragonal (BCT) structure (Figure 3-1) with the lattice constants of $a = b = 1.833c$. Anisotropic elastic modulus and the coefficient of thermal expansion (CTE) of Sn unit cell can vary by a factor of 3 and 2, respectively [7, 11].

Under the thermal loading condition, the solder joints experience complex deformations including elastic, plastic deformations and rate-dependent creep

deformation [1, 12, 13]. Numerous studies have been conducted to develop the creep models and obtain constitutive properties of SAC solder materials, which can be found in Ref. [14]. However, these material properties were obtained typically by conducting experimental tests in a macroscale, which described the deformations in an average sense. A few researchers [1, 4, 7, 11, 15] have investigated the vsicoplastic behavior of SAC solder considering the anisotropic properties of large Sn grains. It is very critical to have experimental work to investigate the deformations of SAC305 solder grains under the thermal cycling conditions to validate and improve the existing constitutive models. But, there are only limited reports about SAC solder deformation behavior under thermal cycling conditions [9, 16]. To the best knowledge of the authors, in-situ thermo-mechanical deformation behavior for a SAC305 joint with a single gain under thermal cycling conditions have not yet been investigated experimentally. Therefore, one of the objectives is to investigate the in-situ anisotropic thermo-mechanical behavior of Sn-based lead-free solder grain under the thermal cycling conditions considering different grain orientations.

With the advancements of microelectronic packaging, more and more innovative microstructures are introduced in the packaging such as through silicon via (TSV) in 2.5 D and 3D packaging, redistribution layer (RDL) in wafer level packaging, etc. The products based on these technologies are already introduced in the commercial sectors, but the reliability of these microstructures is not yet fully understood. The FEA modeling is a great tool to predict the deformation of the microstructures under mechanical and thermal loading conditions. However, it is very challenging to obtain accurate prediction due to the uncertainty in the non-linear mechanical behavior of

packaging materials such as epoxy molding compound (viscoelastic material) and solder (viscoplastic material) as well as approximations used in the complex 3-D models, albeit not impossible. Experimental investigations about the deformations of these microstructures are needed to complement the complex modeling efforts and to find design weak points if exist.

Special considerations arise for the deformation measurements of tiny specimens or tiny regions of large specimens. The relative displacement within a small field of view will be small, while, the strain can be large. A displacement measurement tool with high sensitivity and spatial resolution is required. It becomes another objective of this work.

Moiré interferometry is an optical technique to map the full filed in-plane deformations of advanced engineering structures with extremely high resolution and signal to noise ratio. It has been used extensively in electronic packaging for design and reliability assessment [17-32]. Moiré interferometry is advanced and implemented for complex deformation analyses in this work. Two major improvements include (1) the accurate control of ramp rates during thermal loading for rate-dependent deformation studies for SAC solder alloys, and (2) imaging capability and higher measurement sensitivity for micromechanical deformation analyses.

1.2. Organization of Dissertation

This first chapter introduces the reader to the motivation behind this work and describes the objectives sought to be accomplished by it. The remainder of the dissertation is divided into two parts: Part I - advancement of moiré interferometry for

rate-dependent material behavior study; Part II – advancement for experimental analyses of micromechanical defamations.

Chapter 2 presents the advancement of the moiré interferometry for real-time observation of thermal deformations. Two most notable advancements are (1) on the mechanical front: conduction-based thermal chamber for a wide range of ramp rates with accurate temperature control, and (2) on the optical front: microscope objectives to observe a microscopic field of view. The advancements enable the method to document the global and local behavior of a FO-WLP while it is subjected to a controlled thermal excursion. After describing the details of two advancements, a procedure of actual testing is presented. The advanced configuration is implemented to analyze a FO-WLP in a package-on-package (PoP) with and without a reworkable underfill. The results obtained from the global and local analyses are presented, and reliability implications are discussed. This advanced moiré system is used in the following studies of solder materials and microstructure deformations.

Chapter 3 introduces an experimental study to measure the anisotropic CTE values of SAC305 grains using the advanced moiré interferometry presented in Chapter 2. The theoretical relationships between the CTE values and the engineering surface strains are derived first. Cube shape solder specimens that contain a single grain of SAC305 are fabricated, and the thermally-induced displacements fields with a sub-micron resolution are measured on two perpendicular surfaces as a function of temperature. The CTE values and the *c*-axis direction are determined from the theoretical relationship. The test results are followed after the detailed description of

specimen preparation. The validity of the measurement is corroborated using the grain orientation measured by the electron backscatter diffraction (EBSD) method.

Chapter 4 presents the experimental investigation of the in-situ thermo-mechanical deformation behavior of anisotropic SAC305 solder grain using the advanced moiré interferometry system. A novel copper-steel specimen frame is designed to apply well-controlled mechanical loading on the single grain solder specimen. The cooling rate during solder solidification is controlled to make the solder specimen with a single grain. Both polarizing microscopy and EBSD technique are employed to identify the number of grains in the solder joint and detect the grain orientation. The detailed in-situ deformation evolutions of the single-grain solder joints with different grain orientations are documented during a thermal cycling of -40 °C to 125 °C. The results are analyzed and reveal that the deformations behavior and accumulated damage of the solder joint have strong grain orientation dependency. The methodology and experimental data shown in this work can lead more accurate anisotropic constitutive properties of Sn-based Pb-free solder alloys.

Chapter 5 focuses the development of an advanced immersion microscopic moiré interferometer system. It is based on an achromatic configuration and is implemented for higher displacement sensitivity and spatial resolution.

Chapter 6 present the efforts to further enhance the displacement measurement resolution in terms of high quality specimen gratings and improved optical/digital fringe multiplication (O/DFM) algorithms. To achieve the desired displacement resolution, a high frequency grating (2500 lines/mm) is fabricated on a silicon substrate using lithography first. The square profile is subsequently modified by reactive-ion

etching so that it can be used to produce a specimen grating by replication. Secondly, the algorithms of the optical/digital fringe multiplication method are improved to further enhance the measurement resolution of the immersion microscopic moiré interferometry. The system and the noise-free grating are used to analyze thermal deformations of micro-solder bumps. With the basic contour interval of 200 nm, the displacement resolution of 25 nm is achieved with the multiplication factor of 8.

Chapter 7 contains a summary of the contributions made by this study and a discussion for future studies that can be extended from the present study.

Part I: Advancement of Moiré Interferometry for Rate-dependent Material Behavior

Chapter 2 Advanced Mechanical/Optical Configuration of Real-time Moiré Interferometry for Thermal Deformation Analysis of Fan-out Wafer Level Package

2.1. Introduction

The fan-out wafer level packaging (FO-WLP) technology is emerging rapidly to provide a relatively low-cost packaging solution for high I/O, small footprint, low packaging profile, excellent electrical and thermal performance. It has been adopted in various mobile products, and its market is expected to grow continuously. FO-WLP is an enhancement of standard wafer level chip scale packaging. In the technology, individual chips are embedded into a low-cost epoxy mold compound (EMC) for additional area for I/O connections. A typical FO-WLP structure is shown in Figure 2-1 . It consists of a silicon chip, EMC, redistribution layer (RDL) and solder balls.

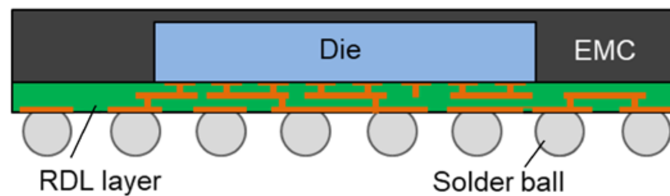

Figure 2-1 Configuration of typical FO-WLP

The results from various reliability tests including moisture, higher temperature storage, temperature cycle and drop, etc. indicated that FO-WLP would generally offer satisfactory component/package level reliability [33-36]. However, several failure modes were reported during the board level reliability tests [33-40]: e.g., solder crack

and RDL failure during the temperature cycle on board (TCoB) tests, intermetallic compound (IMC) crack failure after drop test, etc.

More quantitative analyses are warranted to understand the new failure mechanisms of FO-WLP. Two challenges are encountered when the thermo-mechanical behavior of FO-WLP is to be characterized quantitatively. Like other molded packages, the FO-WLP contains the temperature and rate dependent viscoelastic material (EMC) and viscoplastic material (solder). In addition, the package contains numerous microstructures in a small package dimension. A deformation measurement tool with extremely high displacement resolution and accurate thermal loading control is required.

Moiré interferometry is a full field optical technique to measure the in-plane deformations with high sensitivity and high signal-to-noise ratio. It has been widely used for electronic packaging design and reliability assessment [18-32, 41]. In this paper, moiré interferometry for real-time observation is advanced to quantify the thermo-mechanical deformation of FO-WLP. Two most notable advancements are (1) development of conduction-based thermal chamber for a wide range of ramp rates with accurate temperature control, and (2) use of microscope objectives to view microscopic fields of view. The details of the advancements will be described in Section 3 after presenting the limitations of the current practice in Section 2. The implementation of the advanced system for a FO-WLP in a package-on-package (PoP) will be presented in Section 4.

2.2. Current Practice of Moiré Interferometry

2.2.1. Principle of Moiré Interferometry

Moiré interferometry is an optical, full-field, in-plane measurement technique with high sensitivity, high spatial resolution, and excellent clarity. Moiré interferometry has the ability to map the deformations of advanced engineering structures with extremely high resolution. The data are output as contour maps of in-plane displacements. A detailed description of moiré interferometry can be found in Ref. [17].

In this method, a high frequency diffraction grating is replicated on a specimen, and it deforms together with the underlying specimen. A virtual reference grating is formed by two coherent beams of light. The deformed specimen grating and the uniform reference grating interact to produce moiré patterns of in-plane displacements. The resulting fringe patterns represent contours of constant U and V displacements, which are related to the fringe orders by [17]:

$$U\left(x,y\right)=\frac{1}{f}N_x\left(x,y\right),\quad V\left(x,y\right)=\frac{1}{f}N_y\left(x,y\right) \tag{2-1}$$

where N is the fringe order and f is the frequency of the virtual reference grating. In routine practice, a virtual reference grating with a frequency of 2400 lines/mm is used, which provides a contour interval of 417 nm per fringe order. The engineering in-plane strains can be determined by:

$$\varepsilon_x\left(x,y\right)=\frac{\partial U}{\partial x}=\frac{1}{f}\frac{\partial N_x\left(x,y\right)}{\partial x} \tag{2-2}$$

$$\varepsilon_y\left(x,y\right)=\frac{\partial V}{\partial y}=\frac{1}{f}\frac{\partial N_y\left(x,y\right)}{\partial y} \tag{2-3}$$

$$\gamma_{xy}(x,y) = \frac{\partial U}{\partial y} + \frac{\partial V}{\partial x} = \frac{1}{f}\left(\frac{\partial N_x(x,y)}{\partial y} + \frac{\partial N_y(x,y)}{\partial x}\right) \quad (2\text{-}4)$$

2.2.2. Current Practice for Real-time Observation

When deformations have to be documented as a function of temperature, it is necessary to implement moiré interferometry with an environmental chamber that provides heating and cooling. Several researchers have developed moiré setups for real-time observation [21, 25, 26]. Zou et al. developed a vacuum thermal chamber with radiation and conduction heating (plate heater) to produce a thermal loading of room to 260 °C [21]. Ham et al. developed a thermal chamber using tape-type heaters and thermoelectric modules, which provided a temperature range from -10 °C to 180 °C [26]. They achieved a heating and cooling rate up to 13.3 °C/min. Cho et al. used a microprocessor controlled convection oven to achieve a wider temperature range (-55 °C to 260 °C) [25, 28-32, 42]. The problems associated with vibration were circumvented by using a portable moiré interferometer and the specially-designed specimen holder that was connected directly to the interferometer.

The convection-based real-time moiré setup to circumvent the vibration problem is illustrated in Figure 2-2 [25]. Two major components are a portable moiré interferometer (PEMI II, Photomechanics Inc.) and a computer controlled environmental chamber (EC1A, Sun Systems). The maximum ramp rate of the chamber is 30 °C/min, but, the actual ramp rate is much smaller due to the large thermal mass of the specimen holder.

In the real-time moiré setups, commercial video camera lenses are used as an imaging system. They have limited numerical aperture and zoom capability, and it is difficult to document the global and local (microscopic) deformations simultaneously using the imaging system.

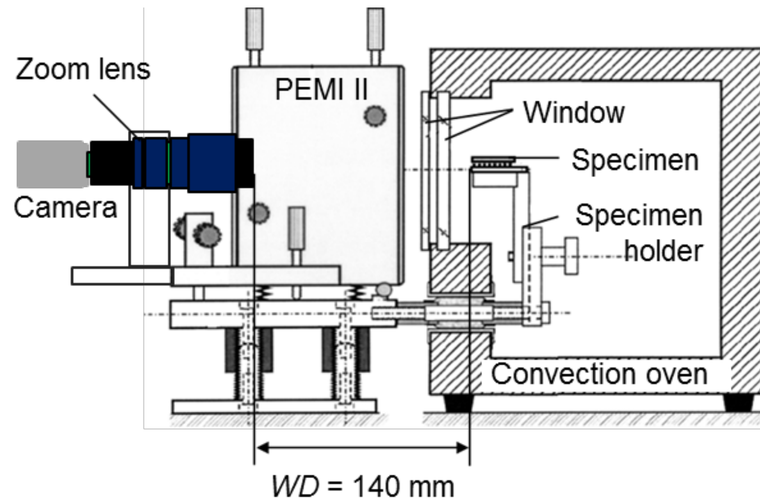

Figure 2-2 Schematic illustration of the convection-based real-time moiré setup

2.3. Advancements of Real-time Moiré Interferometry

Two major advancements are described in detail: (1) development of conduction-based thermal chamber for a wide range of ramp rates with accurate temperature control and (2) use of microscope objectives to view microscopic fields of view.

2.3.1. Thermal Loading Chamber

A compact conduction-based thermal loading chamber was developed. The targeted temperature range was -40 °C to 150 °C with the maximum ramp rate of 1 °C/sec. The configuration of the chamber is shown schematically in Figure 2-3a. A

high performance thermal head with Peltier modules (Silicon Thermal Company: thermal head TH220-2) is used to provide the required the heating/cooling power.

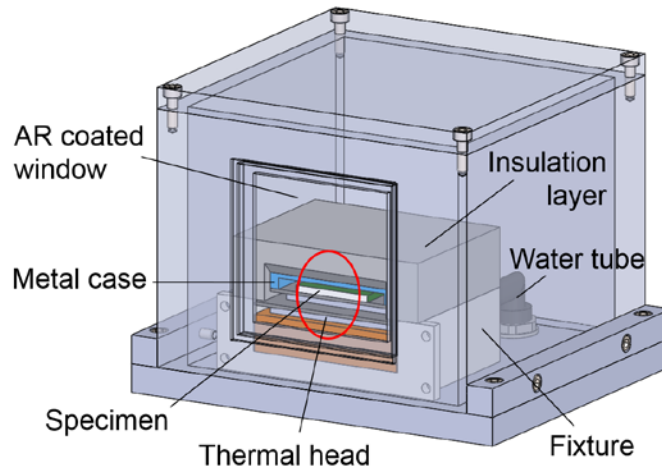

(a)

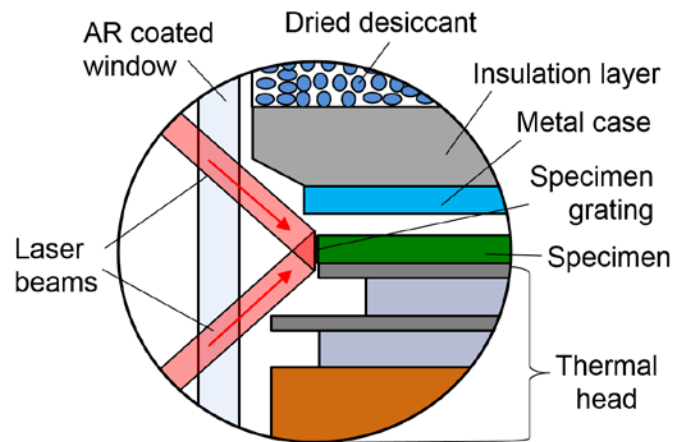

(b)

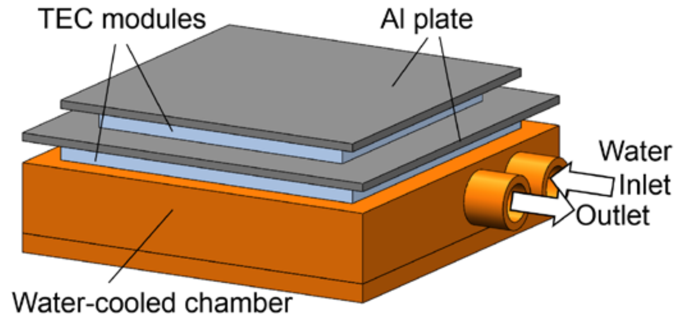

(c)

Figure 2-3 (a) 3D view of chamber, (b) side view of the circled area in (a), and (c) thermal head

The detailed side view of the area marked by a red circle in Figure 2-3a is shown in Figure 2-3b. A specimen is placed on the thermal head using a thermal grease. A metal case is mounted over the specimen, and an insulation layer is wrapped around the metal case. The metal case reaches virtually the same temperature as the top surface of the thermal head, and it acts as a heat radiation source during experiments. Without the metal case, heat loss of the specimen though radiation would occur, which would result in the non-uniform temperature distribution of the specimen.

The laser beams illuminate the specimen grating through an optical window, which is schematically shown in Figure 2-3b. The window is coated with anti-reflection (AR) coating to avoid reflections which can cause undesired interference patterns from the window surfaces, also known as ghost patterns. When deformations are measured at cryogenic temperatures, e.g., -40 °C, moisture is condensed on the surface of the specimen grating, which is difficult to remove during testing. To cope with the problem, the chamber is filled with dried desiccants (shown in Figure 2-3b) that absorb the moisture inside the chamber prior to testing.

Figure 2-3c shows the details of the thermal head, which consists of two layers of thermoelectric cooler (TEC) modules mounted directly on a water-cooled chamber. The TEC module consists of many pairs of P-type and N-type semiconductor pellets. Most commercial TEC temperature controllers use the pulse-width modulation (PWM) technique to power the pellets [43]. With the PWM technique, a power supply provides a constant voltage to a microcontroller, which adjusts the duty cycle to provide a required power input to the TEC. The heating/cooling modes are controlled by a full H-bridge included in the controller, which biases the voltage direction. This is a cost-effective solution since only a constant voltage source is required.

Moiré fringes are documented when a target temperature is reached. In order to maintain the target temperature, a pulse voltage input is continuously supplied to the TEC. The pulse voltage deforms the P-pellet and N-pellet alternatingly, which causes relative displacements between the interferometer and the specimen grating. Moiré interferometry measures tiny displacements and these inadvertent displacements can cause the moiré fringes to dance at the pulse frequency. A single fringe pattern can be captured, but it is not possible to capture a series of fringes patterns with a fixed phase shifted amount. The series of fringes patterns are needed for the post-image processing scheme known as the optical/digital fringe multiplication (O/DFM) method employed in the microscopic analysis of this study [24, 44]. More details about the O/DFM will be discussed later.

The continuous voltage loading is used to cope with the above problem. The temperature control setup for the continuous voltage loading is shown in Figure 2-14. A programmable DC power supply (Keysight: N5744A) provides an input voltage

ranging from 0 to 13.5 V. The full H-bridge used for the PWM technique is customized to control the heating/cooling modes for the continuous voltage loading.

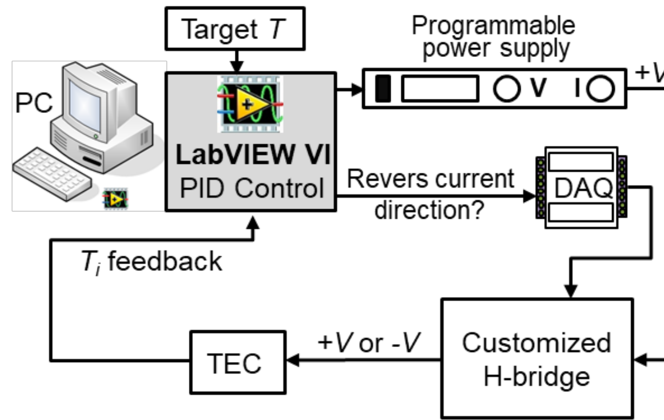

Figure 2-4 Temperature control setup using a continuous voltage

A full H-bridge consisted of four N-MOSFETs is utilized [45]. The gates of two low side N-MOSFETs can be simply driven by a signal of 0 V/5 V provided by a NI DAQ, which controls the OFF/ON status of the MOSFETs. However, the gates of the two high side N-MOSFETs should be driven by a voltage signal at least 5 V higher than the DC voltage loading on the TEC. The DC voltage loading varies from 0 to 13.5 V, and the driving voltage for the high side N-MOSFET is 18.5 V. A circuit shown in Figure 2-5 is designed to provide the output voltage signal 0 V or 18.5 V. It consists of an N-MOSFET, a P-MOSFET, AC adaptor (18.5 V output) and the same NI DAQ that is used to control the low side N-MOSFETs. When DAQ output is 5 V, the circuit will produce 18.5 V output signal. In this way, the H-bridge is controlled effectively for the current thermal head application.

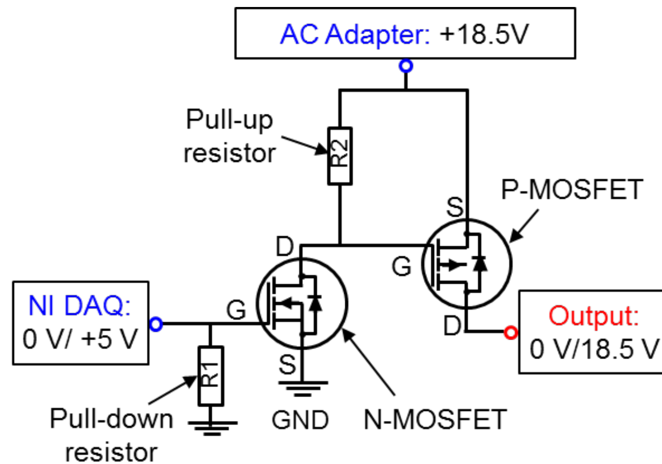

Figure 2-5 A circuit designed to control the N-MOSFET at the high side of the H-bridge

To produce a target temperature profile, the voltage input magnitude and direction are controlled by a LabVIEW Virtual Instrument (VI) with a proportional-integral-derivative (PID) control logic. The temperature of the top thin Al layer (Figure 2-3c) on the thermal head responses to the voltage input change of the TEC very quickly due to its high thermal conductivity and low thermal mass.

Figure 2-6 shows an example of temperature control, where a thermal cycle profile with a ramp rate of 12 °C per minute is shown in (a) and the temperature stability at the maximum temperature (125 °C) is shown in (b). Accurate control of the ramp rate and the target temperature is evident.

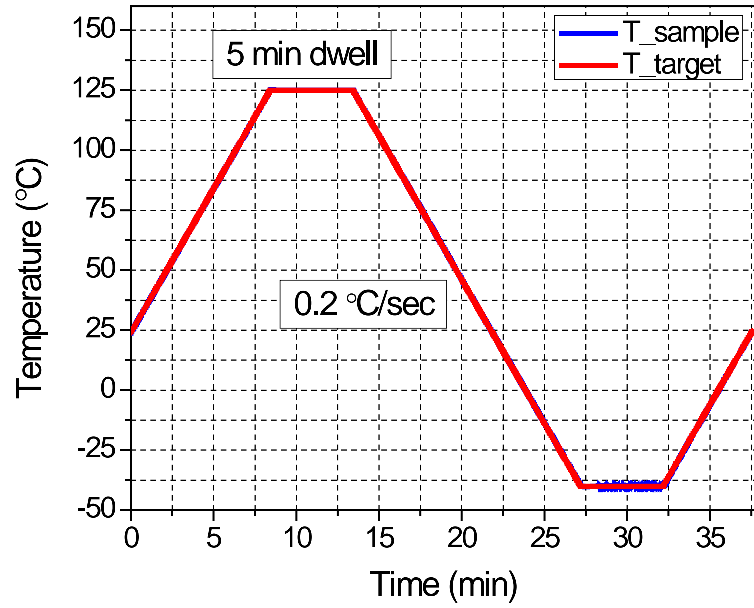

(a)

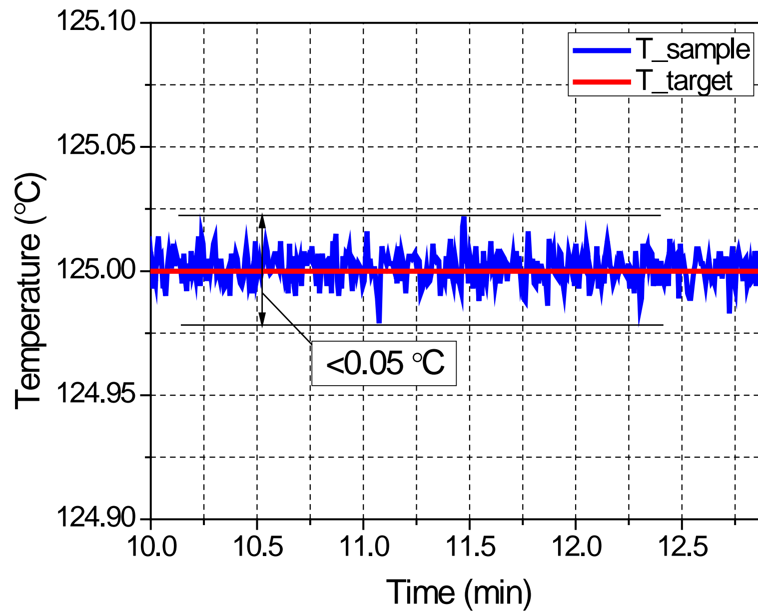

(b)

Figure 2-6 Temperature loadings provided by the conduction chamber: (a) temperature profile with a ramp rate of 0.2 °C/sec, and (b) temperature variation at the steady state

2.3.2. Imaging System Using Microscope Objectives

The comprehensive experimental study of FO-WLP requires a large range of fields of view (FOV) that allows simultaneous measurements of global as well as local (microscopic) deformations. The commercial zoom lenses employed in the real-time moiré setup are ideal for the global deformations, but do not provide the required range of microscopic viewing.

Another important aspect related to the imaging system is the numerical aperture (*NA*), which defines the maximum cone of light that can enter the lens (Figure 2-7) as:

$$NA = n \cdot sin\left(\theta\right) = n \cdot \frac{\left(\phi / 2\right)}{\sqrt{WD^2 + \left(\phi / 2\right)^2}} \tag{2-5}$$

where n is the refractive index of the medium in which the lens is working, ϕ is the diameter of lens and *WD* is the working distance. The current arrangement of the imaging system has a large working distance, and thus, the *NA* is limited (see Figure 2-2).

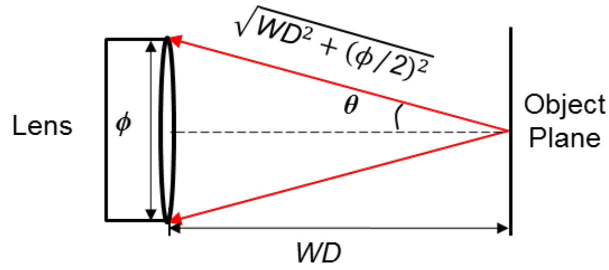

Figure 2-7 Definition of numerical aperture

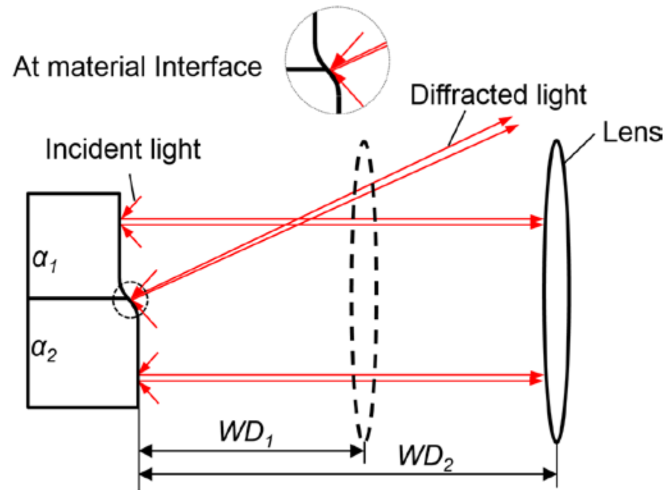

Figure 2-8 Illustration of the effect of out-of-plane displacements at the material interface

Numerous material interfaces exist on the surface of the FO-WLP specimen. As illustrated in Figure 2-8, thermal loading induces a localized but large out-of-plane displacement at the interface due to a large CTE difference of adjacent materials. If the slope caused by the out-of-plane displacement is so large that the diffracted beam pairs miss the lens, the interface area will not be observed by the imaging system; the interface may appear black in the image, called black holes [41].

Long-working distance microscope objectives were incorporated into the system to cope with the challenge. The long-working distance was necessary not to

block the laser beams that formed the virtual reference grating. Figure 2-9 shows a turret-like fixture designed to accommodate two objective lenses (Olympus UPLFLN 4X and Leitz PLAN 10X) mounted directly to the front of the portable moiré system. The two objectives offer FOV ranging from 2.5 mm × 1.8 mm to 0.67 mm × 0.5 mm with a 2/3’’ format CCD camera.

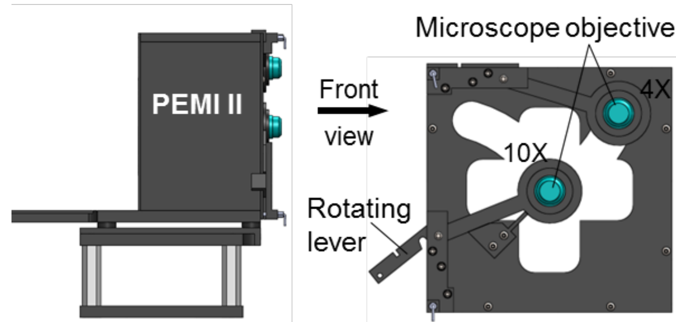

Figure 2-9 Fixture to accommodate microscope objectives; the objectives can be switched by rotating the lever.

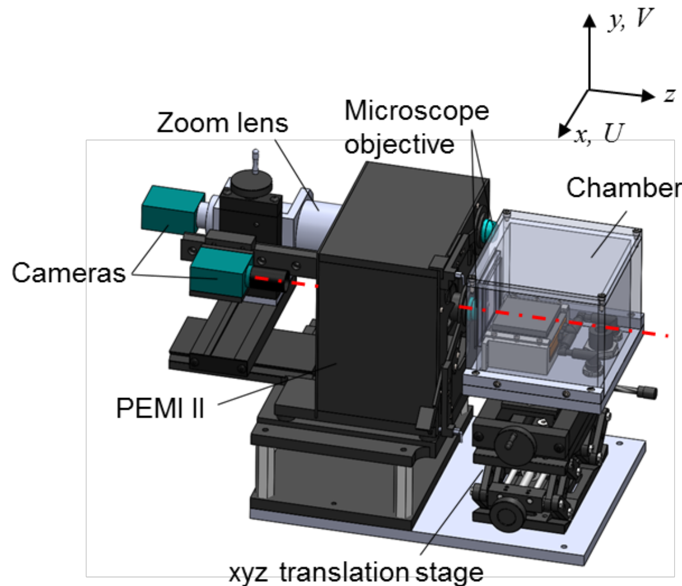

Figure 2-10 Schematic illustration of the complete system with two cameras; use of the objective is illustrated in the figure.

The complete system with two cameras is illustrated in Figure 2-10. The zoom lens is directly mounted to the first camera. The second camera (without a lens) works with the objectives. The figure illustrates the camera position when an objective lens is engaged. Two cameras are mounted on an x-traverse for easy positioning. The whole camera fixture can also move along the z direction to position the cameras.

The thermal chamber is mounted on a xyz translation stage. The xy directional movement enables the system to observe the fringe pattern at any part of the specimen. When a microscope objective and the second camera are used (Figure 2-10), the camera is moved along the z direction to a fixed imaging plane for a desired FOV first, and then the z direction high precision stage under the chamber is used to focus the specimen on the second camera through the objective. The range of the FOV provided by the imaging system is 0.5 mm × 0.5 mm to 40 mm × 40 mm.

2.4. Thermo-mechanical Behavior of Fan-out Wafer Level Package

A package-on-package (PoP) mounted on a PCB substrate is tested. The PoP consists of a FO-WLP (bottom) and a wire-bond BGA (WB-BGA) package (top). Two specimens are studied to investigate thermo-mechanical stresses: one filled with a reworkable underfill and the other without it.

2.4.1. Specimen Preparation

The PoP specimens were ground flat to expose the cross sections of interest. The detailed description of the specimen cross sections is shown in Figure 2-11a and b for without and with underfill, respectively, where the main dimensions are labeled.

The wire bond BGA package contains three chips. It is connected to the bottom component through five columns of solder balls. The bottom FO-WLP component

contains one chip, and it is mounted on a printed circuit board (PCB) through 500 solder balls. The specimen gratings (f_s = 1200 lines/mm) were replicated on the cross sections at room temperature (22 °C). The details about the grating and replication procedures used in this study can be found in Ref. [22, 41].

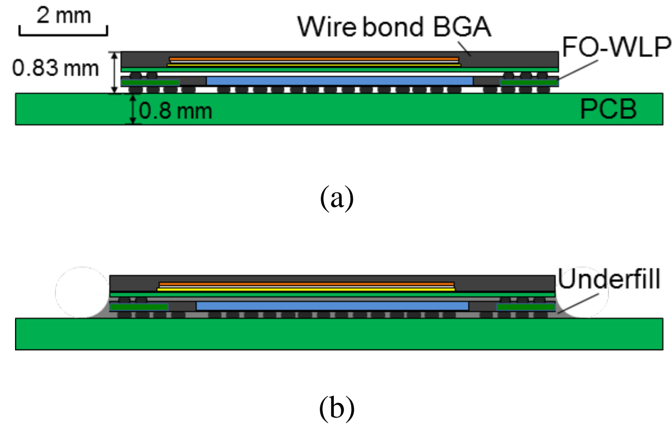

(a)

(b)

Figure 2-11 Cross sections of the PoP specimens: (a) without underfill and (b) with underfill

2.4.2. Moiré Experiment and Results

The advanced real-time moiré setup was employed to document the deformations under the passive thermal condition of -20 °C to 125 °C. During the experiment, the camera with a zoom lens was used to capture the global deformations of the specimens and the camera with a microscope objective was used to capture the solder ball deformations. In the portable moiré system, the collimated beams to form the *U* and *V* field fringe patterns are switched manually by the mechanical shutters, which is shown in Figure 2-12 (left). Two stepper motors were added to rotate the shutters automatically (Figure 2-12 right) during the experiments. An Arduino board, an Adafruit motor control shield and a power supply were used to control the stepper

motors through a LabVIEW VI, which is integrated into the image capture LabVIEW VI. With the automatic shutter, it took only less than a few second to capture the phase-shifted images of the *U* and *V* field fringe patterns at the peak temperatures.

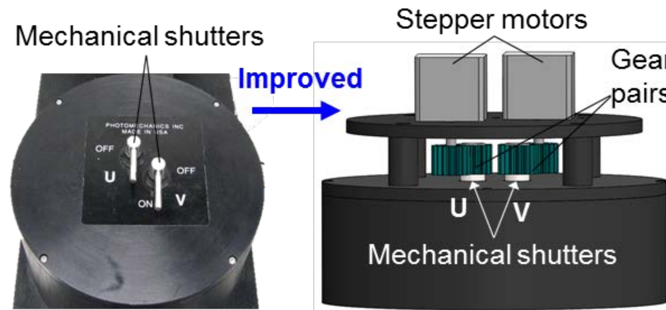

Figure 2-12 Automatic shutter control for capturing the *U* and *V* field fringe patterns

2.4.2.1. Global deformation

The representative fringe patterns obtained at two peak temperatures are shown in Figure 2-13. The effective CTE of the PoP package is much smaller than the PCB. As a result, the specimens show opposite bending deformations with respect to the reference temperature: downwards (∩) at -20 °C and upwards (∪) 125 °C.

Moiré fringes in Figure 2-13 were analyzed further to show the global deformations. The phase shifting technique was implemented to obtain fractional fringe orders along the boundaries of the specimens, and they were used to plot deformed configurations. The deformed configurations are shown in Figure 14, where the deformations are much exaggerated. Figure 14 also shows the outlines of the specimens at the reference temperature (black dash lines). The opposite bending deformations with respect to the reference temperature are evident.

Without Underfill

At -20 °C

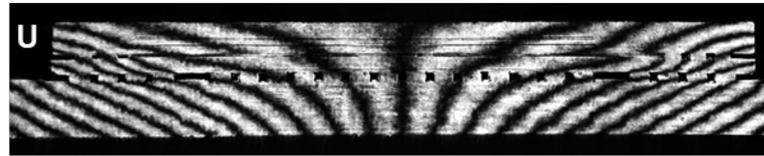

At 125 °C

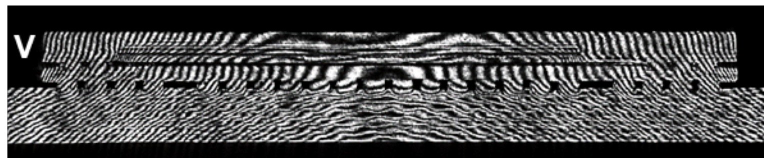

With Underfill

At -20 °C

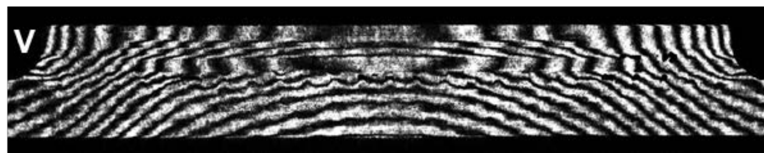

At 125 °C

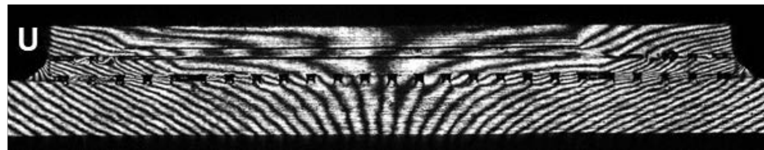

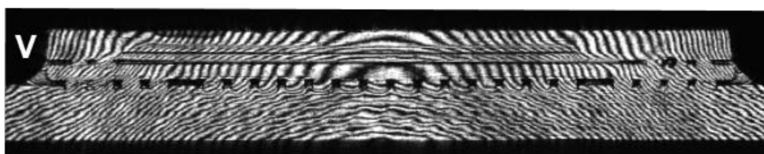

Figure 2-13 Global deformation of PoP packages with and without underfill

In order to show the effect of the underfill more quantitatively, the *V* displacements (bending) obtained at -20°C were subtracted from those obtained at 125°C; the net results represent the bending displacements caused by heating the specimens from -20 °C to 125 °C (ΔT = 145 °C). The results with and without underfill are compared in Figure 2-15, where the displacements are extracted along (a) the PCB centerline, (b) the FO-WLP centerline, and (c) the centerline of the WB-BGA.

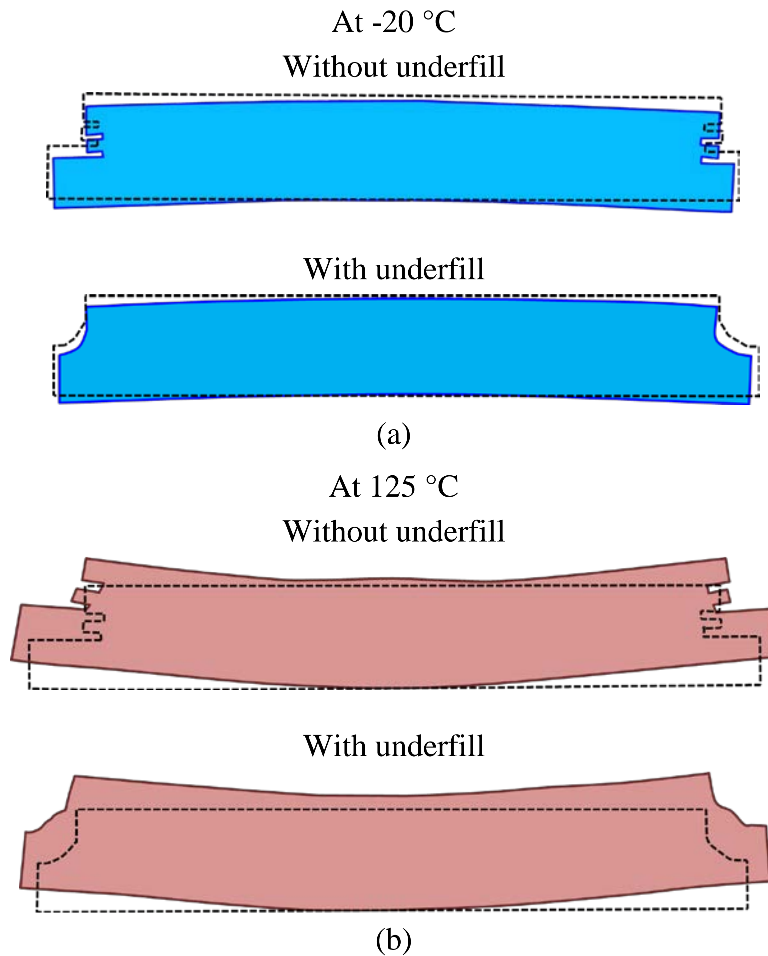

Figure 2-14 Deformed configurations: (a) at -20 °C and (b) at 125 °C. Dashed lines represent the undeformed configurations.

The displacements along the centerlines of the FO-WLP and the PCB are virtually the same for both cases (Figure 2-15a and b). The large number of solder balls

between them is attributed to the coupling that causes the similar bending. However, the bending displacements of the WB-BGA are quite different (Figure 2-15c). Only few solder balls are present between the WB-BGA and the FO-WLP. With the underfill, the coupling between the WB-BGA and the FO-WLP increased and the WB-BGA tends to have the same bending shape as the FO-WLP. The results clearly indicate that the underfill provided strong coupling between the bottom FO-WLP and the top WB-BGA package in spite of its relatively small modulus.

2.4.2.2. Local solder ball deformation

The deformations of the solder balls between the PCB and FO-WLP were analyzed. Although the microscope objectives provided the desired FOV, the basic sensitivity of the system did not produce a sufficient number of fringes for a quantitative analysis over the solder balls. The optical/digital fringe multiplication (O/DFM) method was implemented to enhance the displacement resolutions. The O/DFM method utilizes a β number of equally phase-shifted fringe patterns, and subsequently produces a displacement contour map with β times as many fringe contours as the original moiré fringe patterns [44]. Figure 2-16 shows four phase-shifted fringe patterns of solder #2 in the specimen without underfill, captured at 125 °C. The fringe pattern processed by the O/DFM method (a fringe multiplication factor β = 4) is also shown in the figure, where the contour interval is reduced to 104 nm/fringe.

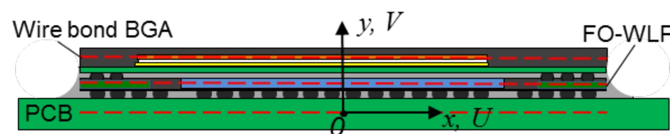

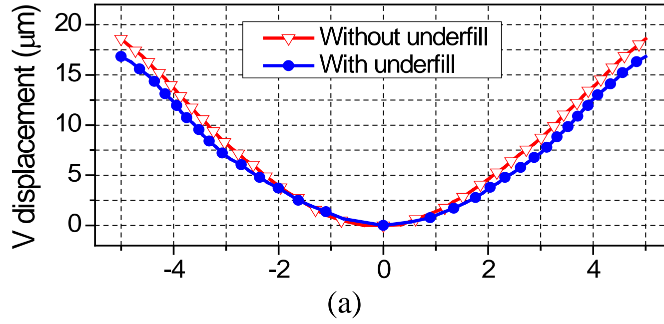

(a)

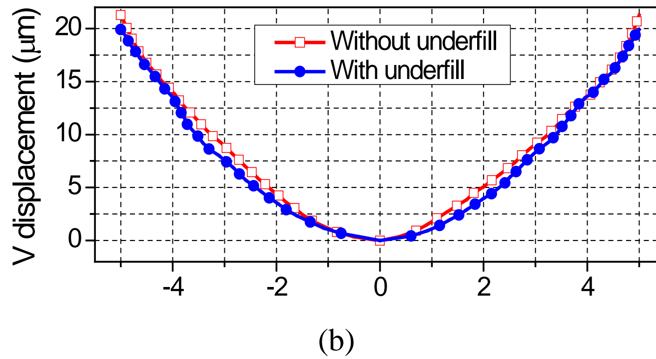

(b)

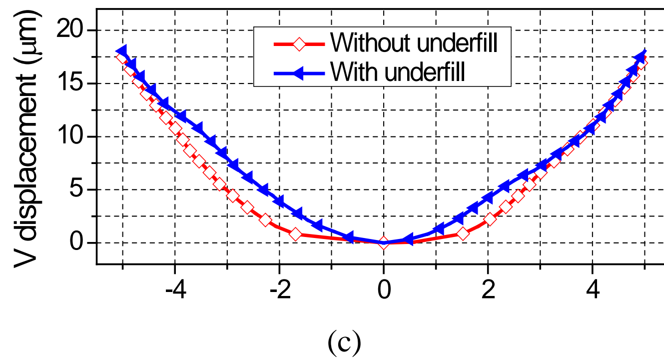

(c)

Figure 2-15 Bending displacements with and without underfill, caused by heating the specimen from - 20°C to 125°C (ΔT = 145 °C), are compared: along (a) the PCB centerline, (b) the FO-WLP centerline, and (c) the centerline of WB-BGA

The representative fringe patterns of the important solder balls with $\beta = 4$ are shown in Figure 2-17, where the solder balls are outlined by yellow dash lines. The larger deformations of the solder balls with underfill are evident by a larger number of

fringe patterns. The average shear strain of solder balls can be determined from the fringe patterns using Eq. (2-4).

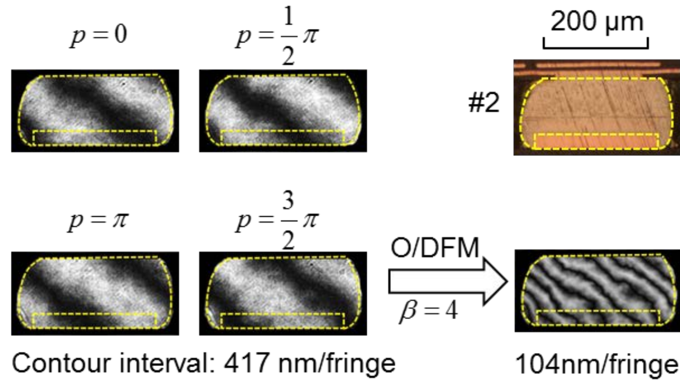

Figure 2-16 Illustration of O/DFM with $\beta = 4$

The average shear strain of solder balls caused by heating the specimens from -20 °C to 125 °C (ΔT = 145 °C) were obtained by subtracting the strains obtained at -20 °C from those at 125 °C. The results are plotted in Figure 2-18. It is to be noted that the shear strain distribution is not symmetric due to the asymmetric design of the WB- BGA component. Overall, the underfill increased the shear strains of solder ball. However, its effect on solder #1 to #8 is different from solder #22 to #14. The large shear strains occurred at the solder ball adjacent to the die shadow. For the specimen without underfill, the maximum shear strain occurred at solder balls #4 and #20, while the maximum shear strain occurred at solder balls #4 and #19 for the specimen with underfill.

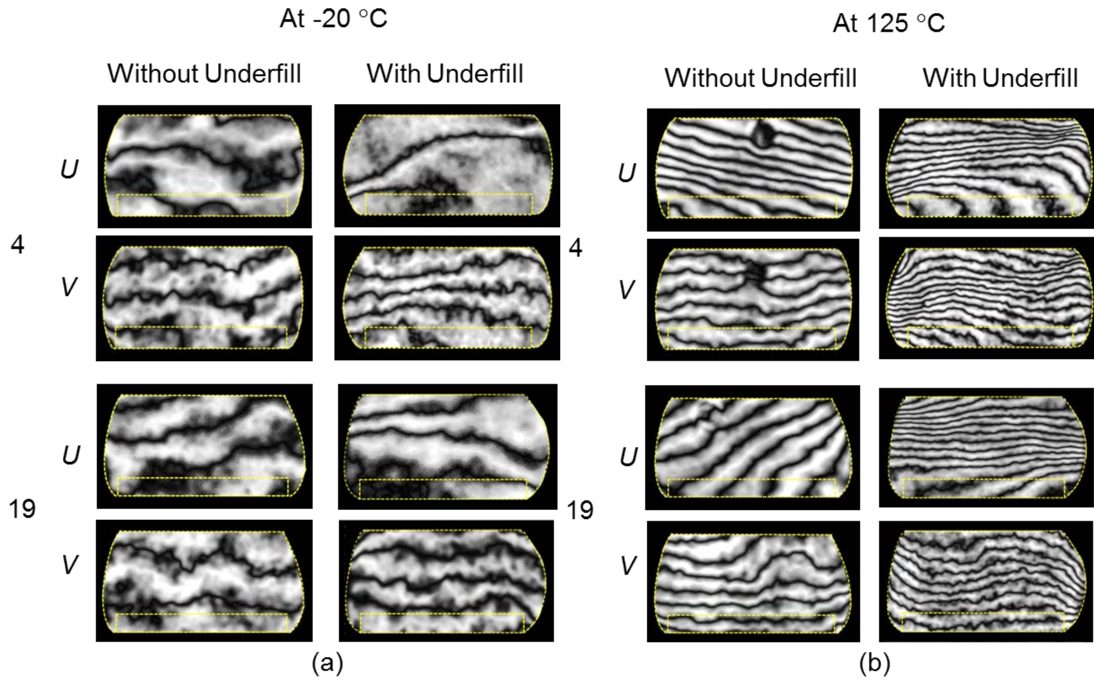

Figure 2-17 Fringe patterns of solder balls (#4 and #19) at: (a) -20 °C and (b) 125 °C. The contour interval is 104 nm per fringe

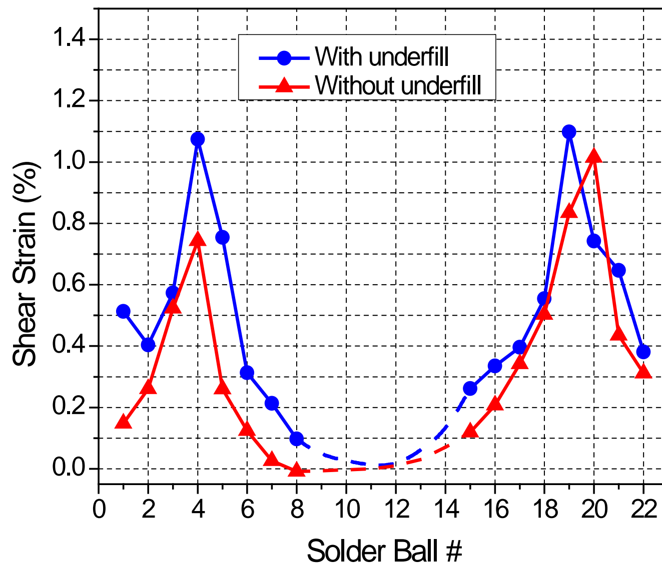

Figure 2-18 Average shear strains of solder balls

2.5. Discussion: Effect of the Reworkable Underfill

Capillary-flow underfill (CUF) was the first technology brought to market for early chip on board and flip chip applications. The original CUF was a liquid encapsulate, usually epoxy resins heavily filled with SiO2, which was applied between the chip and the substrate after flip-chip interconnection was made. It was developed and implemented to reduce the shear strain of flip chip bumps under thermal cycling, caused by the CTE mismatch between the silicon chip and the substrate (or chip carrier) [46-48]. Dramatic reduction of the strain was achieved by converting a discreet solder bump structure into a continuous layer. Therefore, the high modulus and the low CTE of CUF were desired.

More recently, the usage of CUF was extended for portable electronics to enhance the drop reliability of ball grid array (BGA) components. Unlike the original thermoset-based CUF, the CUF of the PoP tested in the study was based on thermoplastic to meet the critical "reworkability" requirement. The thermoplastic-based reworkable CUF resulted in the relatively lower modulus and the higher CTE compared to the thermoset-based CUF, which could adversely affect the board level reliability (BLR) under thermal cycling.

Direct measurements of solder ball deformations of PoP packages with and without the reworkable CUF revealed that the underfill increased the shear strain of solder balls, but the maximum solder ball strain did not change significantly with the underfill. It is thus reasonable to conclude that the BLR of the PoP package with the current underfill under thermal cycling is expected to be comparable with that of the package without the underfill.

2.6. Conclusion

The mechanical/optical configuration of moiré interferometry was advanced to quantify the thermo-mechanical deformations of FO-WLP in a PoP. On the mechanical front, a conduction-based thermal chamber was developed to provide a wide range of ramp rates with accurate temperature control. On the optical front, the microscope objectives were incorporated in the imaging system to observe microscopic fields of view. The advanced configuration was implemented to analyze a FO-WLP in a PoP. Two PoP specimens (with and without reworkable underfill) were prepared, and they were subjected to an identical thermal cycle. The strain analysis of solder balls revealed that that the BLR of the package with the current underfill under thermal cycling is expected to be comparable with that of the package without the underfill.

The global and local thermal deformation analysis capabilities that the advanced real-time moiré interferometry provides can be used effectively to evaluate the thermal cycling BLR of reworkable underfills developed for drop reliability enhancement while avoiding the time-consuming thermal cycling tests.

Chapter 3 Measurement of Anisotropic Coefficients of Thermal Expansion of Single SAC305 Solder Grain

3.1. Introduction

Since Pb was banned for the majority of manufactured electronics, hypoeutectic Pb-free solder, such as Sn3.0Ag0.5Cu (SAC305) and Sn1.0Ag0.5Cu (SAC105) solder alloys, have been widely accepted because they are cost-effective and offer performance like ternary near-eutectic SAC387 solder alloy [1]. Its mechanical behavior is quite different from the traditional eutectic Sn63Pb37 solder. The Sn63Pb37 solder contains soft islands of Pb embedded in Sn matrix [1], and it has been treated as a homogenous material with isotropic properties for stress analyses since its grain size is relatively small [2, 3]. However, hypo-eutectic SAC305 solder alloy contains 96.5% tin (Sn) material and intermetallic compounds (IMCs) of Ag_3Sn and Cu_6Sn_5 disperse around β-Sn grain matrix.

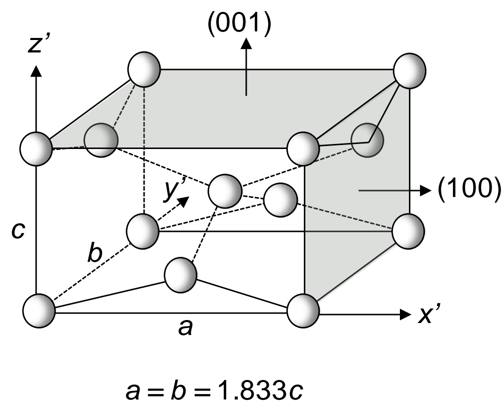

Figure 3-1 Illustration of β-Sn crystal structure

β-Sn grains in SAC solders are large, and some solder joints of surface-mount components contain only one or a few grains [1, 4-10]. Sn crystal has a body-central

tetragonal (BCT) structure (Figure 3-1) with the lattice constants of $a = b = 1.833c$. Anisotropic elastic modulus and the coefficient of thermal expansion (CTE) of Sn unit cell can vary by a factor of 3 and 2, respectively [7, 11].

The CTE values of β-Sn crystal were measured by the X-ray technique [49, 50]. It has been reported that β-Sn has transverse isotropic CTE values. The CTE value on the plane perpendicular to the *c*-axis (Figure 3-1) of the Sn grain is isotropic (i.e., CTE along the *a*-axis). The CTE value along *c*-axis, α_c, is almost twice as large as the value along a-axis, α_a. SAC305 solder joints are expected to have strong anisotropic thermal expansion responses since they contain more than 97% of Sn [6, 7, 9-11, 51]. To the best knowledge of the authors, however, the anisotropic CTE values of SAC305 solder grains have not been measured experimentally.

In this work, the CTE values of SAC305 grains are measured using a full-field in-plane displacement measurement technique called moiré interferometry. A cube shape solder specimen that contains a single grain of SAC305 is fabricated, and the thermally-induced displacements fields with a sub-micron resolution are measured on two perpendicular surfaces as a function temperature. The CTE values and the *c*-axis direction are determined from the theoretical relationship between the CTE values and the engineering surface strains.

The theoretical relationships are described after briefly reviewing moiré interferometry. The test results are followed with the detailed description of specimen preparation. The validity of the measurement is corroborated using the grain orientation measured by the electron backscatter diffraction (EBSD) method.

3.2. Theoretical Derivation

The relationship between the CTE values of SAC solder and the engineering strains is described first. Then, a procedure to determine the CTE values from the engineering strains measured on two perpendicular surfaces is presented.

3.2.1. Relationship between CTE Values and Surface Strains

Figure 3-2 shows the specimen coordinate (*o-xyz*) and the coordinate of an arbitrary grain orientation (*o-x'y'z'*). The blue and red blocks represent the specimen and the solder grain orientation, respectively.

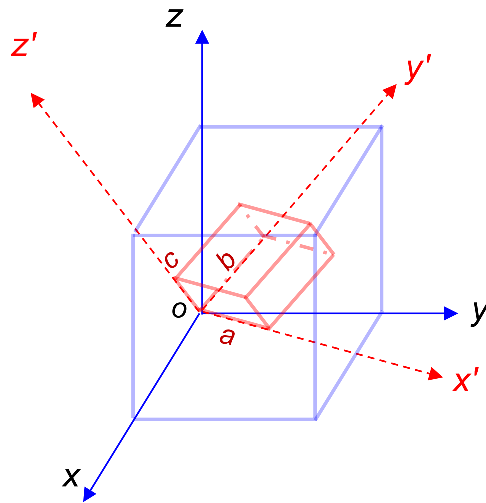

Figure 3-2 Solder specimen coordinate (*o-xyz*) and grain coordinate (*o-x'y'z'*)

In the solder grain coordinate, *c*-axis is aligned with *z'* axis, and *a*-axis and *b*-axis are aligned with *x'*, *y'* axis respectively. The specimen coordinate can be transformed to the solder grain coordinate through three sequential steps of coordinate rotation, schematically illustrated in Figure 3-3: step 1: *xyz* coordinate rotates angle A_1 around *z*-axis and transforms to $x_1y_1z_1$, step 2: $x_1y_1z_1$ coordinate rotates angle A_2

around x_1-axis and transforms to $x_2y_2z_2$, step 3: $x_2y_2z_2$ coordinate rotates angle A_3 around z_2-axis and transforms to grain coordinate $x'y'z'$, where A_1, A_2 and A_3 are Euler angles.

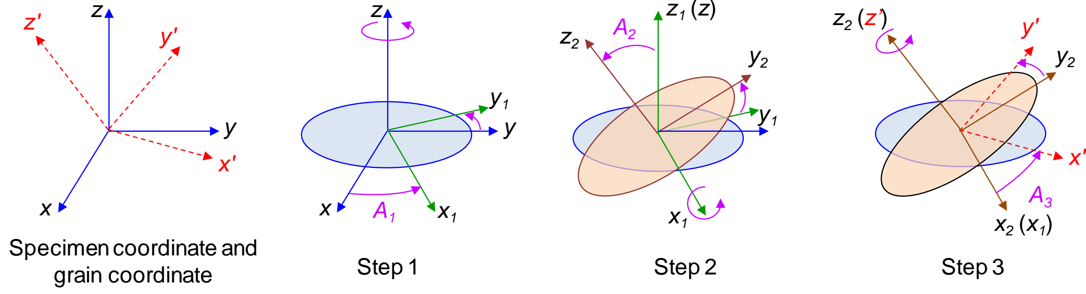

Figure 3-3 Coordinate transformation

The transformation matrix can be determined as:

$$\widetilde{T} = R_{A3}R_{A2}R_{A1}$$
$$= \begin{bmatrix} \cos A_3 \cos A_1 - \sin A_3 \cos A_2 \sin A_1 & \cos A_3 \sin A_1 + \sin A_3 \cos A_2 \cos A_1 & \sin A_3 \sin A_2 \\ -\sin A_3 \cos A_1 - \cos A_3 \cos A_2 \sin A_1 & -\sin A_3 \sin A_1 + \cos A_3 \cos A_2 \cos A_1 & \cos A_3 \sin A_2 \\ \sin A_2 \sin A_1 & -\sin A_2 \cos A_1 & \cos A_2 \end{bmatrix}$$

(3-1)

where $R_{A1} = \begin{bmatrix} \cos A_1 & \sin A_1 & 0 \\ -\sin A_1 & \cos A_1 & 0 \\ 0 & 0 & 1 \end{bmatrix}$, $R_{A2} = \begin{bmatrix} 1 & 0 & 0 \\ 0 & \cos A_2 & \sin A_2 \\ 0 & -\sin A_2 & \cos A_2 \end{bmatrix}$,

$$R_{A3} = \begin{bmatrix} \cos A_3 & \sin A_3 & 0 \\ -\sin A_3 & \cos A_3 & 0 \\ 0 & 0 & 1 \end{bmatrix}.$$

The thermal strain tensor at the grain coordinate can be expressed as:

$$\widetilde{\varepsilon}' = \begin{bmatrix} \varepsilon_{x'x'} & \varepsilon_{x'y'} & \varepsilon_{x'z'} \\ \varepsilon_{y'x'} & \varepsilon_{y'y'} & \varepsilon_{y'z'} \\ \varepsilon_{z'x'} & \varepsilon_{z'y'} & \varepsilon_{z'z'} \end{bmatrix} = \begin{bmatrix} \alpha_a \cdot \Delta T & 0 & 0 \\ 0 & \alpha_a \cdot \Delta T & 0 \\ 0 & 0 & \alpha_c \cdot \Delta T \end{bmatrix} \quad (3\text{-}2)$$

where ΔT is the temperature change; and α_c and α_a are the CTE along the *c*-axis and *a*-axis (or on the *x'y'* plane), respectively.

The strain tensor at the specimen coordinate can be determined by:

$$\tilde{\varepsilon} = \begin{bmatrix} \varepsilon_{xx} & \varepsilon_{xy} & \varepsilon_{xz} \\ \varepsilon_{yx} & \varepsilon_{yy} & \varepsilon_{yz} \\ \varepsilon_{zx} & \varepsilon_{zy} & \varepsilon_{zz} \end{bmatrix} = \tilde{T}^T \tilde{\varepsilon}' \tilde{T} \tag{3-3}$$

From equation (5) – (7), the engineering strains of the specimen surfaces can be expressed in terms of $\varepsilon_{x'}, \varepsilon_{z'}, A_1$ and A_2:

$$\begin{cases} \varepsilon_x = \varepsilon_{xx} = \left(\cos^2 A_2 \cdot \sin^2 A_1 + \cos^2 A_1\right)\varepsilon_{x'x'} + \sin^2 A_1 \cdot \sin^2 A_2 \varepsilon_{z'z'} \\ \varepsilon_y = \varepsilon_{yy} = \left(\cos^2 A_2 \cdot \cos^2 A_1 + \sin^2 A_1\right)\varepsilon_{x'x'} + \cos^2 A_1 \cdot \sin^2 A_2 \varepsilon_{z'z'} \\ \varepsilon_z = \varepsilon_{zz} = \left(\sin^2 A_2\right)\varepsilon_{x'x'} + \cos^2 A_2 \varepsilon_{z'z'} \\ \gamma_{xy} = 2\varepsilon_{xy} = 2\sin^2 A_2 \cdot \sin A_1 \cdot \cos A_1 \left(\varepsilon_{x'x'} - \varepsilon_{z'z'}\right) \\ \gamma_{xz} = 2\varepsilon_{xz} = 2\sin A_2 \cdot \cos A_2 \cdot \sin A_1 \left(\varepsilon_{z'z'} - \varepsilon_{x'x'}\right) \\ \gamma_{yz} = 2\varepsilon_{yz} = 2\sin A_2 \cdot \cos A_2 \cdot \cos A_1 \left(\varepsilon_{x'x'} - \varepsilon_{z'z'}\right) \end{cases} \tag{3-4}$$

3.2.2. Determination of Anisotropic CTE Values from Surface Strains

The principal strains and principal angle of the principal angle on the *xy* plane can be expressed as:

$$\begin{aligned} \varepsilon_{p_1}^{xy} &= \frac{\varepsilon_x + \varepsilon_y}{2} + \sqrt{\left(\frac{\varepsilon_x - \varepsilon_y}{2}\right)^2 + \left(\frac{\gamma_{xy}}{2}\right)^2} \\ \varepsilon_{p_2}^{xy} &= \frac{\varepsilon_x + \varepsilon_y}{2} - \sqrt{\left(\frac{\varepsilon_x - \varepsilon_y}{2}\right)^2 + \left(\frac{\gamma_{xy}}{2}\right)^2} \end{aligned} \tag{3-5}$$

$$\theta_{p_2}^{xy} = \begin{cases} \frac{1}{2}\tan^{-1}\left(\frac{\gamma_{xy}}{\varepsilon_x - \varepsilon_y}\right), \text{ if } \varepsilon_x \le \varepsilon_y \\ \frac{1}{2}\tan^{-1}\left(\frac{\gamma_{xy}}{\varepsilon_x - \varepsilon_y}\right) + \frac{\pi}{2}, \text{ if } \varepsilon_x > \varepsilon_y \end{cases} \tag{3-6}$$

where $\varepsilon_{p_1}^{xy}$ and $\varepsilon_{p_2}^{xy}$ are the first and second principal strains on the *xy* plane, respectively, and $\theta_{p_2}^{xy}$ is the corresponding principal angle for $\varepsilon_{p_2}^{xy}$ measured from the positive *x* axis. Substituting equation (3-4) into (3-5) yields:

$$\begin{aligned} \varepsilon_{p_1}^{xy} &= \cos^2 A_2 \cdot \varepsilon_{x'x'} + \sin^2 A_2 \cdot \varepsilon_{z'z'} = \left(\cos^2 A_2 \cdot \alpha_a + \sin^2 A_2 \cdot \alpha_c\right)\Delta T \\ \varepsilon_{p_2}^{xy} &= \varepsilon_{x'x'} = \alpha_a \cdot \Delta T \\ \theta_{p_2}^{xy} &= A_1 \end{aligned} \tag{3-7}$$

Similarly, the principal strains and principal angle on the on the adjacent *yz* plane (perpendicular to the *xy* plane) can be expressed as:

$$\begin{aligned} \varepsilon_{p_1}^{yz} &= \frac{\varepsilon_y + \varepsilon_z}{2} + \sqrt{\left(\frac{\varepsilon_y - \varepsilon_z}{2}\right)^2 + \left(\frac{\gamma_{yz}}{2}\right)^2} \\ \varepsilon_{p_2}^{yz} &= \frac{\varepsilon_y + \varepsilon_z}{2} - \sqrt{\left(\frac{\varepsilon_y - \varepsilon_z}{2}\right)^2 + \left(\frac{\gamma_{yz}}{2}\right)^2} \end{aligned} \tag{3-8}$$

$$\theta_{p_2}^{yz} = \begin{cases} \dfrac{1}{2}\tan^{-1}\left(\dfrac{\gamma_{yz}}{\varepsilon_y - \varepsilon_z}\right), \text{ if } \varepsilon_y \le \varepsilon_z \\ \dfrac{1}{2}\tan^{-1}\left(\dfrac{\gamma_{yz}}{\varepsilon_y - \varepsilon_z}\right) + \dfrac{\pi}{2}, \text{ if } \varepsilon_y > \varepsilon_z \end{cases} \tag{3-9}$$

where $\varepsilon_{p_1}^{yz}$ and $\varepsilon_{p_2}^{yz}$ are the first and second principal strains on the *yz* plane respectively, and $\theta_{p_2}^{yz}$ is the corresponding principal angle for $\varepsilon_{p_2}^{yz}$ measured from the positive *y* axis. Substituting equation (3-4) into (3-5) yields:

$$\begin{aligned} \varepsilon_{p_1}^{yz} &= \sin^2 A_2 \cdot \sin^2 A_1 \cdot \varepsilon_{x'x'} + \left(\cos^2 A_2 + \sin^2 A_2 \cos^2 A_1\right) \cdot \varepsilon_{z'z'} \\ &= \left[\sin^2 A_2 \cdot \sin^2 A_1 \cdot \alpha_a + \left(\cos^2 A_2 + \sin^2 A_2 \cos^2 A_1\right) \cdot \alpha_c\right]\Delta T \\ \varepsilon_{p_2}^{yz} &= \varepsilon_{x'x'} = \alpha_a \cdot \Delta T \\ \theta_{p_2}^{yz} &= \tan^{-1}\left(\frac{\sin A_2 \cdot \cos A_1}{\cos A_2}\right) \end{aligned} \tag{3-10}$$

In the same way, the principal strains and angle on the *xz* plane can be derived. It is important note that the magnitude of the smaller principal strain remains constant regardless of the plane. The isotropic CTE on the *x'y'* plane is attributed to this constant principal strain. More details about the constant second principal strain on surfaces will be in the discussion section.

From equations (3-11) and (3-10), α_a and α_c can be expressed as:

$$\alpha_a = \frac{\varepsilon_{p_2}^{xy}}{\Delta T}$$
$$\alpha_c = \frac{\varepsilon_{p_1}^{xy}}{\sin^2 A_2 \Delta T} - \cot^2 A_2 \cdot \alpha_a \tag{3-12}$$

where $A_2 = \tan^{-1}\left(\frac{\tan\theta_{p_2}^{yz}}{\cos\theta_{p_2}^{xy}}\right)$.

Similar derivations can be made using $\varepsilon_{p_1}^{yz}$ and $\varepsilon_{p_2}^{yz}$.

$$\alpha_a = \frac{\varepsilon_{p_2}^{yz}}{\Delta T}$$
$$\alpha_c = \frac{\frac{\varepsilon_{p_1}^{yz}}{\Delta T} - \sin^2 A_2 \cdot \sin^2 A_1 \cdot \alpha_a}{\cos^2 A_2 + \sin^2 A_2 \cos^2 A_1} = \frac{\frac{\varepsilon_{p_1}^{yz}}{\Delta T} - \sin^2 A_2 \cdot \sin^2 \theta_{p_2}^{xy} \cdot \alpha_a}{\cos^2 A_2 + \sin^2 A_2 \cos^2 \theta_{p_2}^{xy}} \tag{3-13}$$

The CTE values can be determined by either (3-14) or (3-15) if the engineering strain values on two perpendicular surfaces are available. It is worth noting that the value of α_a can be calculated using the strains of a single surface.

3.3. CTE Measurements

A full-field optical technique called moiré interferometry is used to measure the required engineering strains. The method is described briefly first and results obtained from two specimens are presented.

3.3.1. Experimental Method: Moiré Interferometry

Moiré interferometry is a full-field optical technique to measure the in-plane deformations with high sensitivity, high signal-to-noise ratio, and excellent clarity. Moiré interferometry has the ability to map the deformations of advanced engineering structures with extremely high resolution. The data are output as contour maps of in-plane displacements.

In this method, a cross-line high frequency diffraction grating, f_s, of 1200 lines per mm is replicated on a specimen surface, and it deforms together with the underlying specimen. As illustrated in Figure 3-4, a virtual reference grating, f, is formed by two coherent beams of light. The deformed specimen grating and the uniform reference grating interact to produce moiré patterns of in-plane displacements. It has been widely used for electronic packaging design and reliability assessment [18-32, 52, 53]. A detailed description of moiré interferometry can be found in Ref. [52].

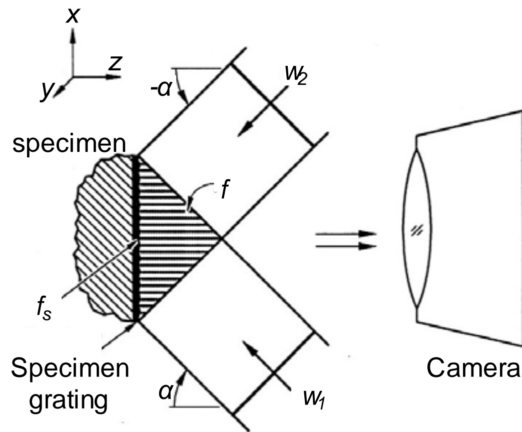

(a)

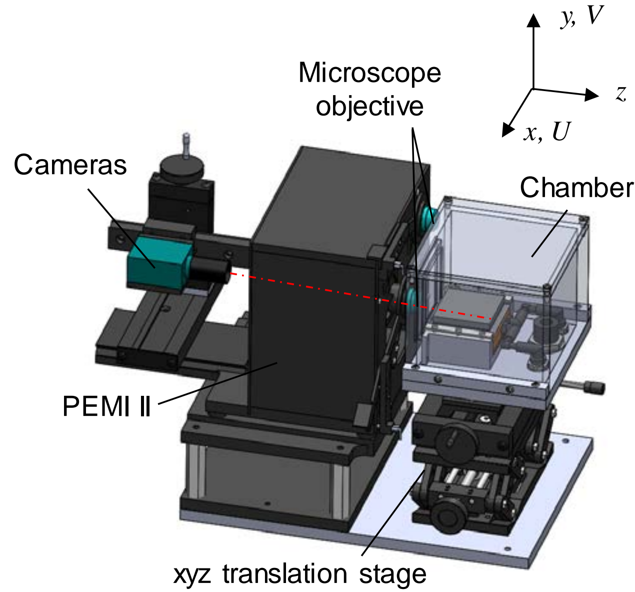

(b)

Figure 3-4 Schematic illustration of (a) the principles of moiré interferometry and (b) the optical/mechanical configuration of an advanced portable moiré system

The resultant fringe patterns represent contours of two in-plane x and y displacements, u_x and u_y, which are related to the fringe orders by [52]:

$$u_x(x,y) = \frac{1}{f} N_x(x,y), \quad u_y(x,y) = \frac{1}{f} N_y(x,y) \tag{3-16}$$

where N is the fringe order and f is the frequency of the virtual reference grating. In routine practice, a virtual reference grating with a frequency of 2400 lines/mm is used, which provides a contour interval of 417 nm per fringe order. The engineering in-plane strains can be determined by:

$$\varepsilon_x(x,y) = \frac{\partial u_x}{\partial x} = \frac{1}{f} \frac{\partial N_x(x,y)}{\partial x} \tag{3-17}$$

$$\varepsilon_y(x,y) = \frac{\partial u_y}{\partial y} = \frac{1}{f} \frac{\partial N_y(x,y)}{\partial y} \tag{3-18}$$

$$\gamma_{xy}(x,y) = \frac{\partial u_x}{\partial y} + \frac{\partial u_y}{\partial x} = \frac{1}{f}\left(\frac{\partial N_x(x,y)}{\partial y} + \frac{\partial N_y(x,y)}{\partial x}\right) \tag{3-19}$$

In this work, an advanced moiré interferometry system developed for temperature-dependent microscopic deformations was used to measure the required deformation fields. The system is illustrated schematically in Figure 3-4b, [53]. It consists of (1) a portable engineering moiré interferometer (PEMI) that provides two sets of virtual reference gratings, (2) a conduction chamber built on a high performance thermo-electric cooler that provides accurate temperature control, and (3) a high-resolution digital camera with a microscope objective lens. The thermal conduction chamber is mounted on an x-y-z translation stage, which allows positioning as well as focusing the specimen. More details of the system can be found in [53].

3.3.2. Specimen Preparation: Solder Specimen with a Single Grain

An aluminum mold with 9 cube shape holes was used to control the shape of solder specimen (≈ 1 mm × 1 mm × 1 mm). A detailed procedure to fabricate the solder specimens is shown schematically in Figure 3-5. The mold was first mounted on an aluminum substrate. They were placed on a plate heater, which was heated to 240 °C. When the mold temperature reached the steady state (about 235 °C), SAC305 solder wire was manually fed into the holes in the mold. After placing a thin hot aluminum plate on the top of the mold, the whole assembly was removed from the heater and was cooled by natural convection. When temperature decreased to 190 °C, the solder was completely solidified, and the assembly was moved to a metal heat sink for faster cooling. There was virtually no wetting between the SAC305 solder and the aluminum mold, and thus the solder specimens were readily removed from the mold.

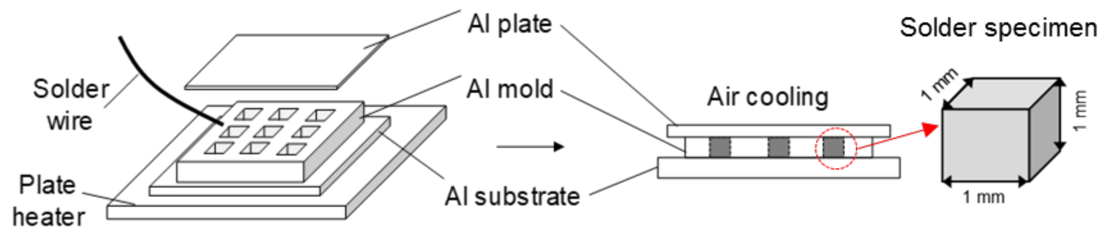

Figure 3-5 Solder specimen fabrication procedures

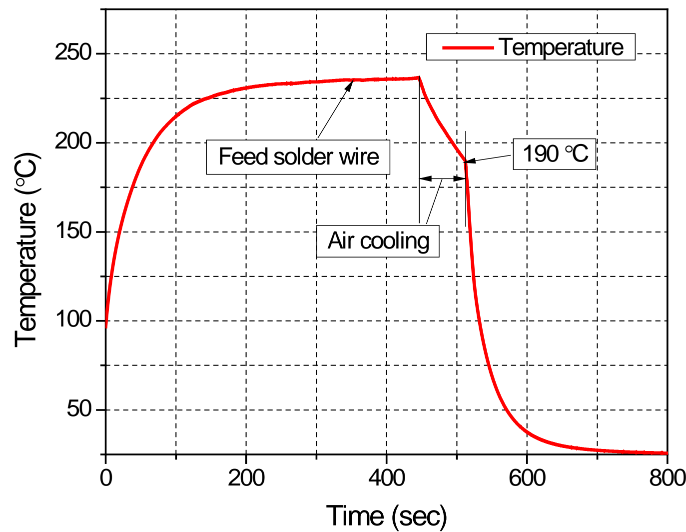

Figure 3-6 Solder reflow profile

The cooling rate during the solidification process is known to be one of the most critical parameters [54] that influence grain growth. By controlling the substrate thickness, different cooling rates were achieved. The solder specimens with a single grain were obtained with a cooling rate of approximately 0.8 °C/sec. The temperature profile of the mold used in this study is shown in Figure 3-6.

All the samples were carefully ground and polished after separation from the mold. Then, the number of the gains on specimen surfaces were examined using a

polarizing microscope. The results obtained from a single-grain specimen are shown in Figure 3-7. The results confirm that the specimen contain a single grain.

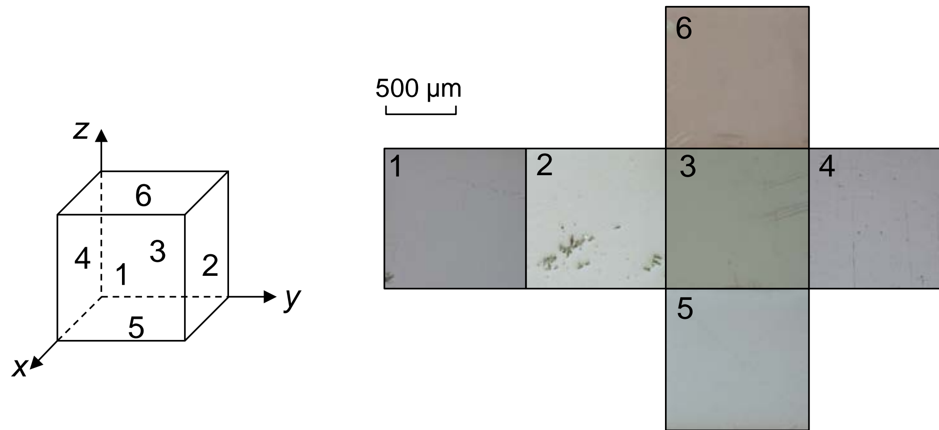

Figure 3-7 Six surfaces of a specimen under the polarizing microscope ensuing a single grain

Two single-grain specimens were prepared for the experiments (will be referred to as Specimen 1 and Specimen 2). The specimen gratings (f_s = 1200 lines/mm) were replicated on two surfaces of each specimen at room temperature. The details about the grating replication procedures can be found in Refs. [22, 52].

3.3.3. Displacement Fields and CTE Values

The in-plane displacements fields (u_x, u_y on the *xy* plane and u_y, u_z on the *yz* plane) were documented at -40, 20, 80, and 140 °C. A total of four moire experiments were conducted (two surfaces of each specimen). The fringe patterns of Specimens 1 and 2, representing the displacement fields, are shown in Figure 3-8 and 9, respectively. In each figure, the displacements of the *xy* plane are shown in (a), and the displacements of the *yz* plane in (b).

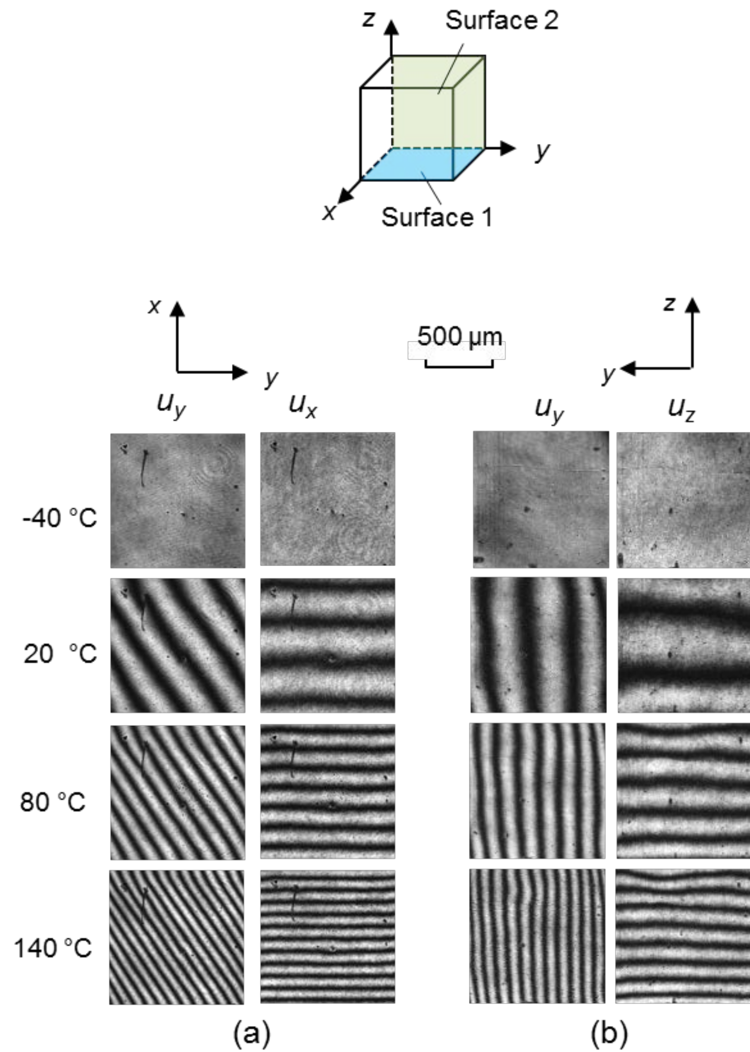

Figure 3-8 Moiré fringe patterns obtained from two surfaces of Specimen 1, where the counter interval is 417 nm/fringe: (a) on the *xy* plane; (b) on the *yz* plane

The moiré interferometer was tuned to produce null fields (i.e., fields devoid of fringes) at -40 °C; the optical configuration was adjusted until the frequency of the virtual reference gratings were exactly twice as high as that of the specimen gratings at -40 °C.

The engineering normal and shear strains $(\varepsilon_x,\ \varepsilon_y,\ \varepsilon_z,\ \gamma_{xy},\ \gamma_{xz})$ were calculated from the fringe patterns using E.q. (3-17), (3-18) and(3-19). The results are

summarized in Table 3-1 and Table 3-2. Two Euler angles (A_1, A_2) were calculated from the engineering strains using equation (11) and (14). The values are shown in Table 3-3. The deviations of the calculated angles from each temperature range is less than 1 degree. The averaged values (Specimen 1: A1 = 132.2º and A2 = -88.4º; Specimen 2: A1 = 57.2º and A2 = - 87.3º) were used to conduct the subsequent CTE calculations.

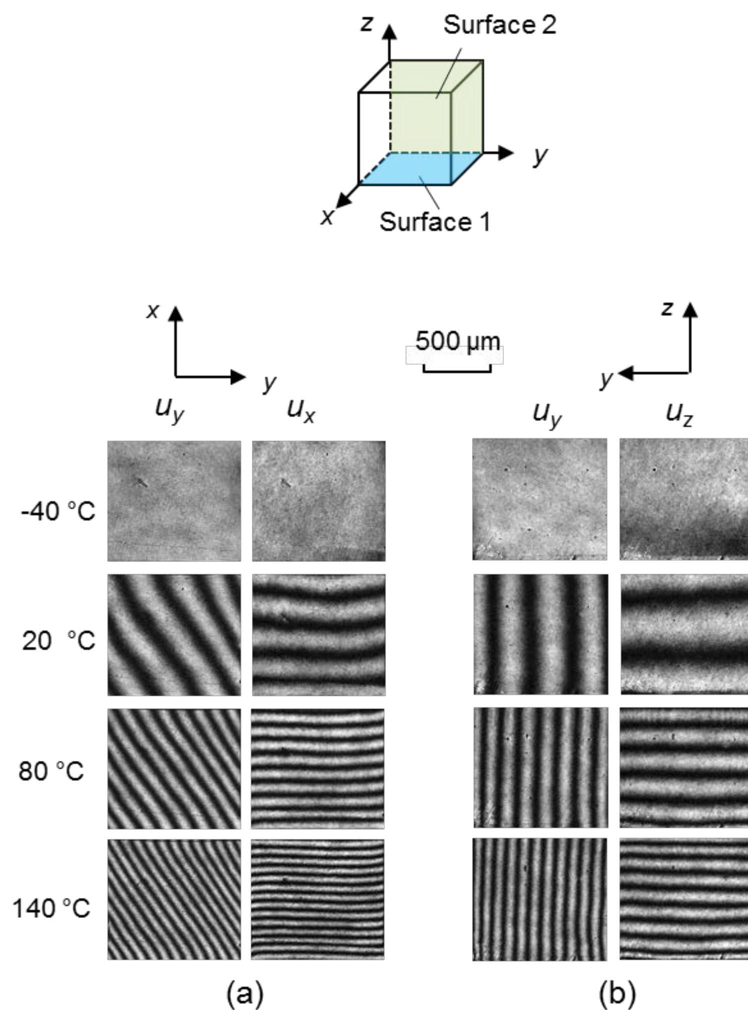

Figure 3-9 Moiré fringe patterns obtained from two surfaces of Specimen 2, where the counter interval is 417 nm/fringe: (a) on the *xy* plane; (b) on the *yz* plane

Table 3-1 Engineering strains obtained from fringe patterns of specimen 1

Temperature range (°C)	Mean temperature (°C)	Surface 1			Surface 2		
		ε_x (10^{-3})	ε_y (10^{-3})	γ_{xy} (10^{-3})	ε_y (10^{-3})	ε_z (10^{-3})	γ_{yz} (10^{-3})
-40 to 20	-10	1.55	1.48	0.96	1.48	1.05	-0.03
20 to 80	50	1.63	1.54	0.99	1.55	1.10	-0.04
80 to 140	110	1.73	1.60	1.04	1.62	1.13	-0.04

Table 3-2 Engineering strains obtained from fringe patterns of specimen 2

Temperature range (°C)	Mean temperature (°C)	Surface 1			Surface 2		
		ε_x (10^{-3})	ε_y (10^{-3})	γ_{xy} (10^{-3})	ε_y (10^{-3})	ε_z (10^{-3})	γ_{yz} (10^{-3})
-40 to 20	-10	1.66	1.26	0.83	1.30	1.03	0.06
20 to 80	50	1.73	1.33	0.86	1.39	1.10	0.04
80 to 140	110	1.83	1.47	0.88	1.44	1.12	0.06

Table 3-3 Euler angles

Temperature range (°C)	Mean temperature (°C)	Euler angle (degree)			
		Specimen 1		Specimen 2	
		A_1	A_2	A_1	A_2
-40 to 20	-10	132.9	-88.6	122.2	86.8
20 to 80	50	132.4	-88.4	122.5	88.1
80 to 140	110	131.2	-88.3	123.9	87.1
Average		132.2	-88.4	122.8	87.3

Table 3-4 CTE values obtained from specimen 1

Temperature range (°C)	Mean temperature (°C)	Specimen 1			
		Based on Eq. (3-12)		Based on Eq. (3-13)	
		α_a (ppm/°C)	α_c (ppm/°C)	α_a (ppm/°C)	α_c (ppm/°C)
-40 to 20	-10	17.2	33.2	17.5	33.6
20 to 80	50	18.1	34.8	18.3	35.4
80 to 140	110	19.0	36.5	18.8	36.8

Table 3-5 CTE values obtained from specimen 2

Temperature range (°C)	Mean temperature (°C)	Specimen 2			
		Based on Eq. (3-12)		Based on Eq. (3-13)	
		α_a (ppm/°C)	α_c (ppm/°C)	α_a (ppm/°C)	α_c (ppm/°C)
-40 to 20	-10	16.6	32.0	17.2	32.7
20 to 80	50	17.6	33.5	18.3	34.8
80 to 140	110	19.6	35.5	18.6	36.9

The CTE values $(\alpha_a,\ \alpha_c)$ over each temperature range were calculated using equations (3-12) and (3-13). The results are summarized in Table 4 and Table 3-5. It is important to recall that the values of α_a can be calculated using the strains of a single surface. The variations of the α_a value from all four surfaces are less than 1 ppm/ºC, which establishes the accuracy of the measurements.

The averaged CTE value of two specimens are plotted as a function of temperature in Figure 3-10. The CTE value along *c*-axis is nearly twice as large as the value along *a*-axis. There is clear linear dependency of the CTE values on the temperature. The temperature dependent CTE values over a temperature range of -40 °C to 140 °C can be expressed as:

$$\begin{cases} \alpha_a\left(\text{ppm/°C}\right) = 17.28 + 0.016T\left(\text{°C}\right) \\ \alpha_c\left(\text{ppm/°C}\right) = 33.18 + 0.029T\left(\text{°C}\right) \end{cases} \tag{3-20}$$

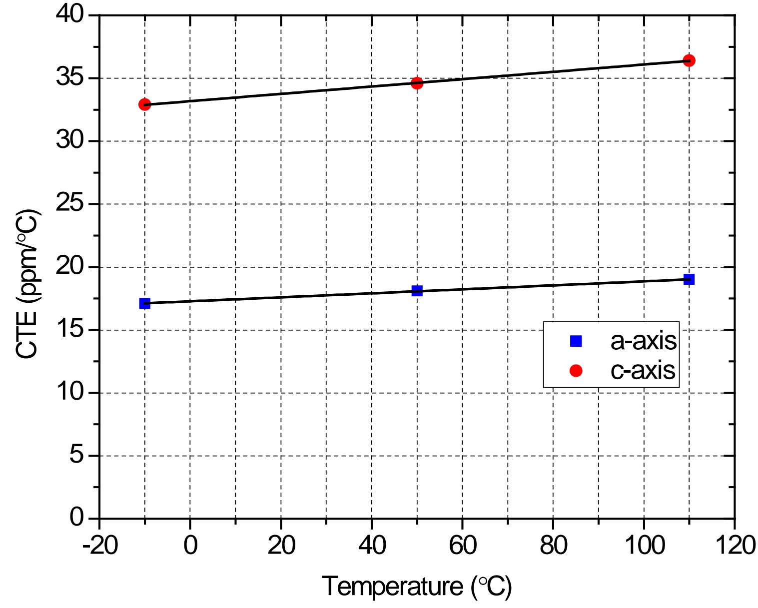

Figure 3-10 Comparison of anisotropic CTE values

3.4. Discussion: Grain Orientation

Determination of the grain orientation is critical to accurate calculation of the CTE values. As illustrated in Figure 3-11, lines *OE* and *OF* represent the principal angles of $\theta_{p_2}^{xy}$ and $\theta_{p_2}^{yz}$, respectively. The two vectors can be expressed as:

$$\begin{cases} \overrightarrow{OE} = \left[\cos\theta_{p_2}^{xy},\ \sin\theta_{p_2}^{xy},\ 0\right] \\ \overrightarrow{OF} = \left[0,\ \cos\theta_{p_2}^{yz},\ \sin\theta_{p_2}^{yz}\right] \end{cases} \tag{3-21}$$

Substitute equation (3-7) and (3-10) into (3-21) yields:

$$\begin{cases} \overrightarrow{OE} = \left[\cos A_1,\ \sin A_1,\ 0\right] \\ \overrightarrow{OF} = \left[0,\ \cos A_2,\ \sin A_2 \cos A_1\right] \end{cases} \tag{3-22}$$

Then, the unit vector $\overrightarrow{n_1}$ perpendicular to the plane defined by $\overline{OE}$ and $\overline{OF}$ can be expressed as:

$$\overrightarrow{n_1} = \frac{\overrightarrow{OE} \times \overrightarrow{OF}}{\left|\overrightarrow{OE}\right| \cdot \left|\overrightarrow{OF}\right|} = \left[\sin A_1 \sin A_2,\ \ -\cos A_1 \sin A_2,\ \ \cos A_2\right] \tag{3-23}$$

The above unit vector, $\overrightarrow{n_1}$, in the specimen coordinate (*o-xyz*) can be expressed in the coordinate of the grain orientation (*o-x'y'z'*) using the coordinate transformation as:

$$\overrightarrow{n_1} = \tilde{T}\left[\sin A_1 \sin A_2,\ \ -\cos A_1 \sin A_2,\ \ \cos A_2\right]^T = \left[0,\ 0,\ 1\right] = \overrightarrow{n_{z'}} \tag{3-24}$$

The above result proves that $\overrightarrow{n_1}$ and $\overrightarrow{n_{z'}}$ are the same vector confirming that the plane defined by $\overrightarrow{OE}$ and $\overrightarrow{OF}$ coincides with the *x'y'* plane in the grain coordinate.

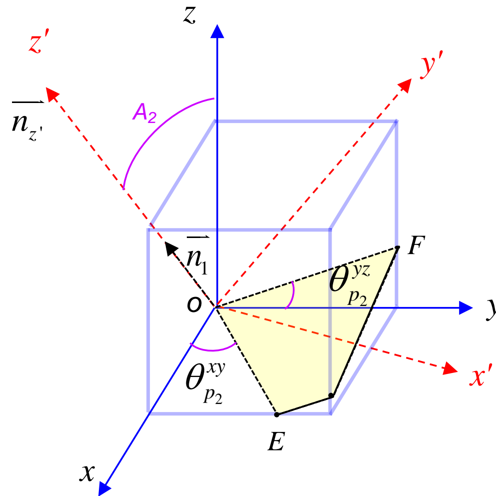

Figure 3-11 Principle angles and grain orientation

This was further confirmed by a supplementary experiment using electron backscatter diffraction (EBSD) technique. The technique has been used widely to characterize microstructural crystallography of any crystalline or polycrystalline materials [55]. Specimen 1 was placed in the SEM chamber, and an EBSD measurement was made on Surface 1.

The result is shown in Figure 3-12. Figure 3-12 (a) shows an EBSD layered image, where the uniform color indicates that the specimen contains only one grain. Based on the Euler angles obtained from the EBSD measurement, the direction vector of *c*-axis in the specimen coordinate (Figure 3-8) was determined. It is [-0.738, -0.675, 0.032], which is very close to the values calculated from the moiré results using equation (22) [-0.727, -0.685, 0.038].

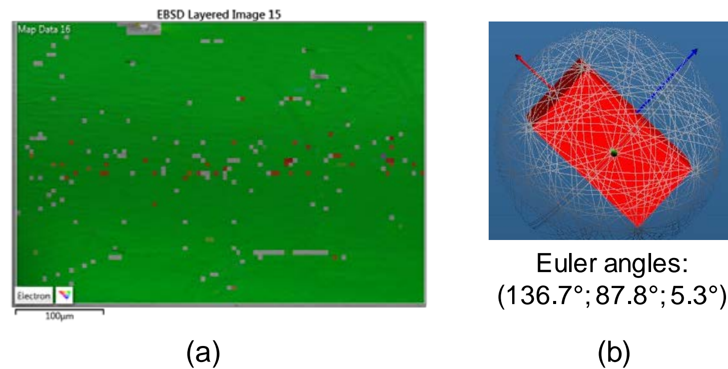

Figure 3-12 EBSD result for specimen 1 on surface 1: (a) EBSD layered image, and (b) grain orientation

3.5. Conclusion

The anisotropic CTE values of SAC305 grains were measured by moiré interferometry. The theoretical relationships between the CTE values and the engineering surface strains were derived first. Two cube shape solder specimens that contained a single grain of SAC305 were fabricated, and the engineering strains were measured on two perpendicular surfaces of each specimen as a function temperature. The CTE values and the c-axis direction were determined from the theoretical relationship. The CTE value along c-axis is nearly twice as large as the value along a-

axis while both values showed clear linear dependency on the temperature. The validity of the measurement was corroborated using the grain orientation measured by the electron backscatter diffraction (EBSD) method.

Chapter 4 Experimental Study of a Single SAC305 Grain Deformation under Thermo-Mechanical Loading

4.1. Introduction

Pb-based solder alloys were once the most commonly used interconnect materials in electronic packages. Due to environmental and health concern over the toxicity of Pb material, Pb solder product has been banned gradually. Pb-free solders become popular and widely adopted in the electronic packaging. Hypoeutectic Sn3.0Ag0.5Cu (SAC305) and Sn1.0Ag0.5Cu (SAC105) solder alloys have been widely accepted because they are cost-effective but offer performance similar to the ternary near-eutectic SAC387 (recommended by iNEMI) in terms of microstructure and mechanical response [15].

The hypo-eutectic SnAgCu (SAC) alloy contains about 97% of Sn and its mechanical behavior is quite different from the traditional eutectic Sn63Pb37 solder[6]. Eutectic Sn63Pb37 solder contains soft islands of Pb embedded in Sn matrix [1]. It has been treated as a homogenous material with isotropic properties since its grain size is relatively small [2, 3]. The grain boundary sliding is the dominant creep mechanism for this solder [1, 14, 56]. However, Sn grains in SAC solders are large, and some solder joints contain only one or a few grains [1, 4-10]. The SAC solder has hard intermetallic compounds (IMCs) of Ag_3Sn and Cu_6Sn_5 disperse around the Sn dendrites which limits the grain boundary sliding, and the dominant creep mechanism is the dislocation climb [1, 4, 57]. Compared to PbSn solder, it shows superior creep resistant and durability under creep-dominant fatigue loads such as thermal cycling [1, 8].

Sn crystal has a body-central tetragonal (BCT) structure, shown in Figure 3-1, and it has anisotropic thermo-mechanical properties. Anisotropic elastic modulus, *E*, and CTE of Sn unit cell vary by a factor of 3 and 2, respectively [7, 11]. It is expected that these SAC solder joints have strong anisotropic mechanical response depending on the Sn grain orientation [6, 7, 9-11, 51].

Reliability of solder joints under thermal cycling condition is one of the main concerns in electronic packages. Under the thermal loading condition, the solder joints experience complex deformations including elastic, plastic deformations and rate-dependent creep deformation [1, 12, 13]. Numerous studies have been conducted to develop the creep models and obtain constitutive properties of SAC solder materials, which can be found in Ref. [14]. However, these material properties were obtained typically by conducting experimental tests in a macroscale, which described the deformations in an average sense. A few researchers [1, 4, 7, 11, 15] have investigated the vsicoplastic behavior of SAC solder considering the anisotropic properties of large Sn grains. It is very critical to have experimental work to investigate the deformations of SAC305 solder grains under the thermal cycling conditions to validate and improve the existing constitutive models. But, there are only limited reports about SAC solder deformation behavior under thermal cycling conditions [9, 16]. To the best knowledge of the authors, in-situ thermo-mechanical deformation behavior for a SAC305 joint with a single gain under thermal cycling conditions have not yet been investigated experimentally.

In this work, the in-situ deformation behavior of SAC305 solder joint with a single grain under thermal cycling condition is studied by an advanced moiré

interferometry system. A novel specimen is designed and fabricated to apply a well-controlled loading on the solder joint under thermal loadings and it is described after brief reviewing the advanced moiré system. The detailed procedures to obtain a solder joint with a single grain are introduced. After that, the deformations of the specimens are documented under the thermal cycling conditions. The deformation analyses are followed with a discussion about the deformation prediction capability of the existing constitutive models and anisotropic properties of Sn grain.

4.2. Moiré Interferometry for Real-Time Deformation Observation

Moiré interferometry is a full-field optical technique to measure the in-plane deformations with high sensitivity, high signal-to-noise ratio, and excellent clarity. The outputs are fringe patterns representing contours of U and V displacement. The displacements are related to fringe orders by Eq. (2-1).and the engineering in-plane strains can be determined by Eq. (2-2) to (2-4). More details can be found in chapter 2 [53].

In this work, an advanced moiré interferometry system developed for temperature-dependent microscopic deformations (introduced in chapter 2) was used to measure the required deformation fields. The system is illustrated schematically in Figure 4-1[53]. It consists of (1) a portable engineering moiré interferometer (PEMI) that provides two sets of virtual reference gratings, (2) a conduction chamber built on a high performance thermo-electric cooler that provides accurate temperature control, and (3) two high-resolution digital cameras with a zoom lens and microscope objectives. The thermal conduction chamber is mounted on an x-y-z translation stage, which allows positioning as well as focusing the specimen. The system is able to provide

accurate temperature loading from -40 °C to 150 °C with ramp rate up to 1 °C/sec. It is very critical for the experimental study of temperature-rate-dependent solder material behavior. The range of the field of view provided by the imaging system is from 0.5 mm × 0.5 mm to 40 mm × 40 mm which enables the deformation observation on the local and global areas of specimen during experiment.

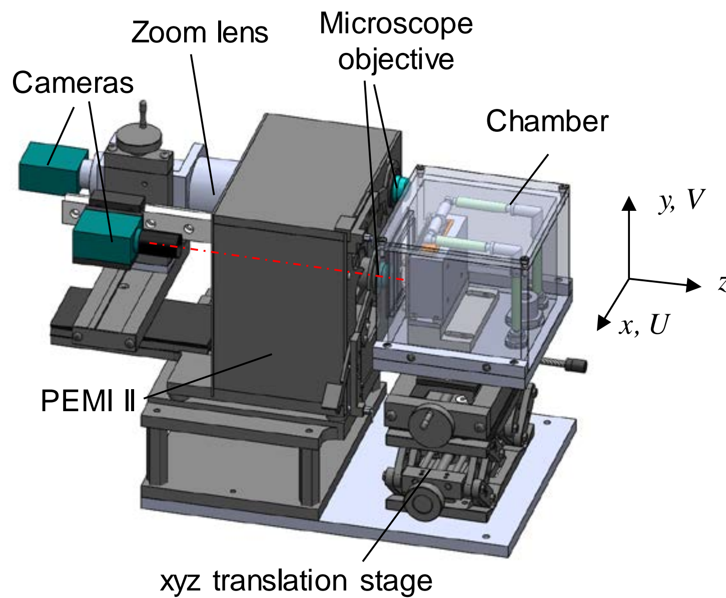

Figure 4-1 Schematic illustration of the optical/mechanical configuration of advanced portable moiré system

4.3. Specimen Design and Fabrication

4.3.1. Specimen Configuration

In electronic packaging, solder joints experience elastic, plastic and creep deformation under the thermal loading condition. It is caused by the coefficients of thermal expansion (CTEs) mismatch among different packaging materials. However, due to the complex structure of actual electronic component and material properties, it

is very difficult to quantify the mechanical response of the actual solder joint from its complex stress and strain state.

In this work, a new specimen configuration was designed to simplify the stress and strain state of solder joint under the thermal cycling condition and to investigate the mechanical response of SAC305 solder material. The specimen configuration was first introduced by Cho [58] to study the thermo-mechanical behavior of PbSn eutectic solder. The specimen was fabricated with copper (Cu) and steel material whose material properties are well-known [59] (Table 4-1). The design was modified to produce a higher strain at solder joint under thermal loading conditions in this study. The specimen configuration is shown in Figure 4-2. The CTE difference (~5 ppm/°C) between copper and steel produces the mechanical deformation of the solder joint when the specimen is subjected to a thermal cycling. The solder joint deformation due to the CTE mismatch between steel and copper is illustrated in Figure 4-3.

To understand the deformations of the solder joint in the specimen configuration under thermal loading condition, a simplified FEA modeling was conducted where the SAC305 solder joint was assumed to have isotropic elasticity and CTE value. The quarter model is shown in Figure 4-4. The isotropic properties of SAC305 are list in Table 4-2 [60]. The reference temperature was set at temperature 125 °C. The shear stress distribution of the solder joint at 20 °C and comparison of stress components along the center line AA’ are shown in Figure 4-5. It shows that the shear stress is dominant and other stress components are very small.

The main advantages of the copper-steel specimen frame design are: (1) the symmetric design minimizes the bending of specimen and provides shear dominant

loading on the solder joint, (2) local CTE mismatch is minimized by using the same copper materials connected with the solder joint, and (3) the solder joint geometry can be controlled.

Table 4-1 Material properties of AISI 1081 steel and OFC 101 Cu

	AISI 1018 Steel	OFC 101 Copper
Elastic modulus E (GPa)	207	114.0-0.0449*T (°C)
Poisson Ratio	0.29	0.34
CTE α (ppm/°C)	11.57+0.01494*T(°C)-1.739E- 5*T2 (°C)	16.28+0.01144*T(°C)-1.064E-5*T^2(°C)

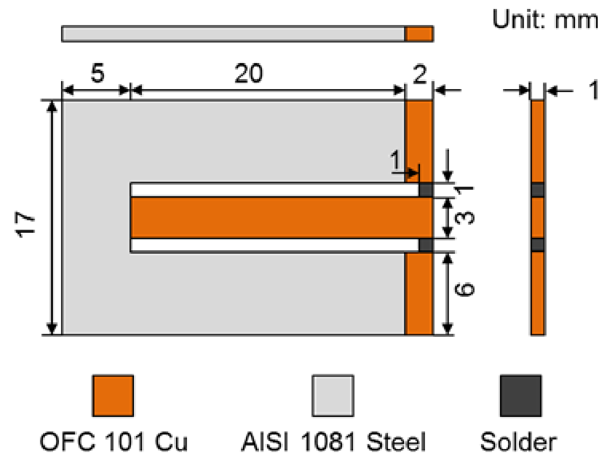

Figure 4-2 Solder specimen configuration

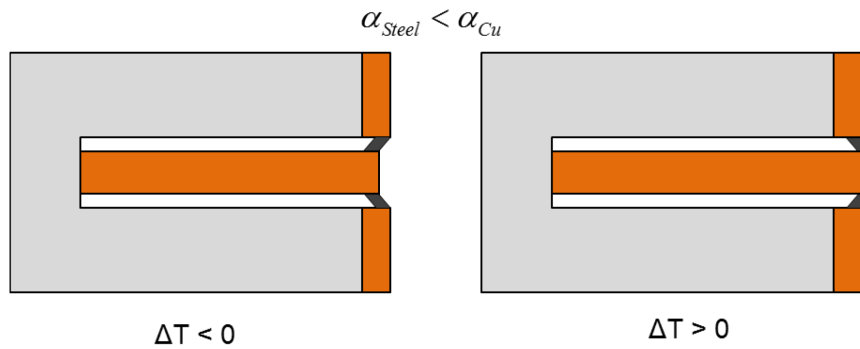

Figure 4-3 Schematic of specimen deformation under thermal loading ΔT

Table 4-2 Isotropic material properties of SAC305

Young's Modulus (GPa)	Poisson's Ratio	CTE (ppm/K)
30+(398-*T*(K))*0.1	0.3	21.6

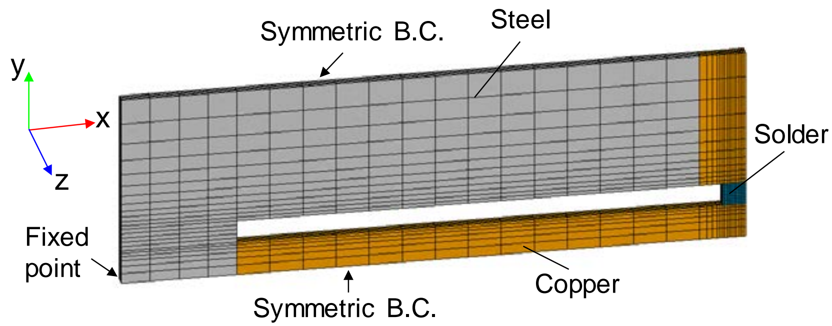

Figure 4-4 A quarter model for copper-steel specimen

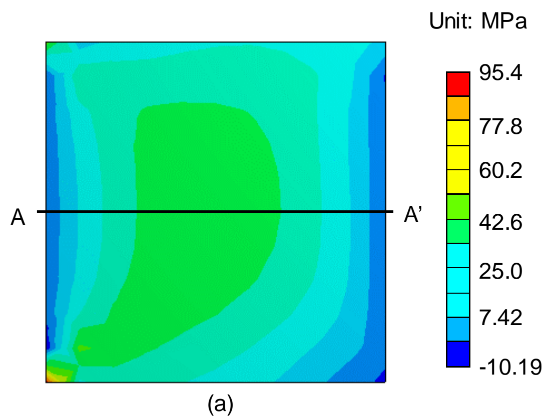

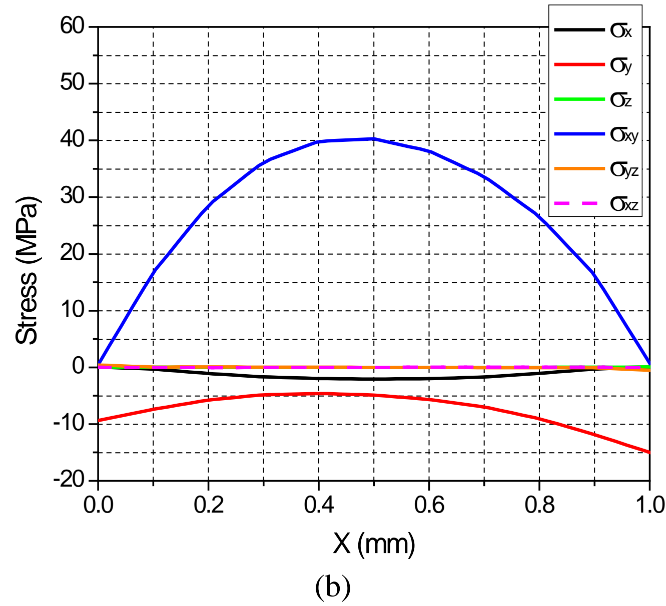

(b)

Figure 4-5 Stress distribution of solder joint in copper-steel frame: (a) shear stress and (b) stress components along line AA'

4.3.2. Specimen Fabrication

The whole specimen fabrication consists of two parts: (1) fabricate Cu-Steel specimen frame, (2) make solder joints.

4.3.2.1. Cu-Steel Specimen Frame

The fabrication process of the specimen is shown in Figure 4-6. In order to ensure the precise geometry control, the wire electro-discharge machining (wire EDM) was used during the fabrication. The Cu and steel were machined and brazed together by a very thin silver braze alloy layer (Harris brazing alloy Safety-Silv®50N: 50Ag28Zn20Cu2Ni) which has the melting temperature of 707 °C. Then, two opening slots were cut by wire EDM followed by slicing to get the copper-steel frames with thickness of 1 mm.

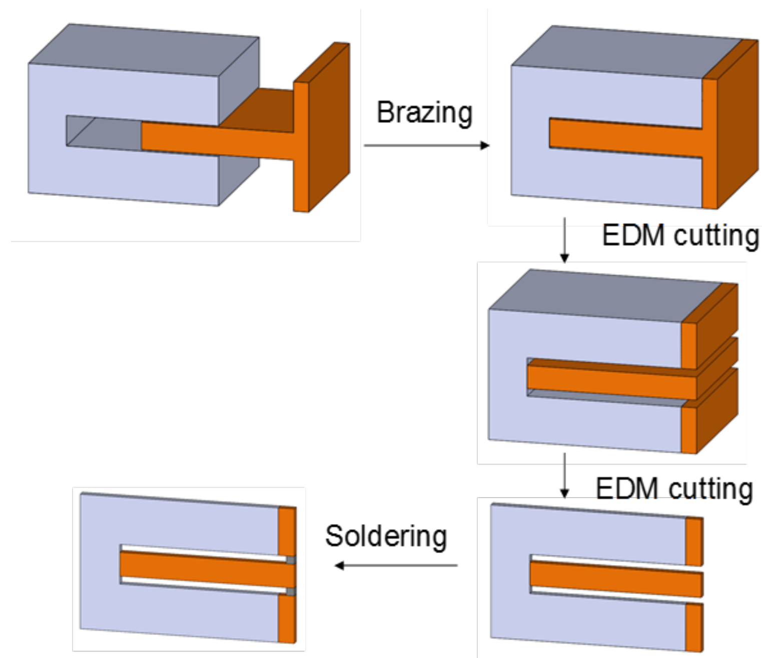

Figure 4-6 Specimen fabrication procedures

4.3.2.2. Solder Joint

Next step is to fabricate SAC305 solder joints with dimension 1 mm (width) × 1 mm (height) × 1mm (thickness) in the Cu-steel specimen frame. The soldering areas on the Cu were ground carefully using 1200 grit sandpaper and cleaned by isopropyl alcohol first. A manual soldering procedure was employed in this work [1, 15] and it is schematically illustrated in Figure 4-7. Two aluminum (Al) blocks were inserted to the slots of Cu-Steel frame and the positions were carefully controlled to ensure the desired width (1 mm) of solder joints. The whole assembly was placed on a Al substrate and moved to pre-heated heating plate whose surface temperature was approximately 30 °C above the melting temperature of SAC305 (217 °C). When the assembly reached ~132 °C, the solder flux was applied to the soldering surfaces. After reaching thermally steady state (~237 °C), a solder wire was manually fed into the gaps.

The soldered specimen was undisturbed on the hot plate for ~1 min. Then, whole assembly was removed from the hot plate to solidify the solder joints. After the sample was cooled down to room temperature, the Al blocks and substrate were readily separated from specimen since there is virtually no wetting between the SAC305 solder and Al material. Then, the excessive solder at the joint areas was removed by grinding using sand paper. The specimen was inspected under optical microscope.

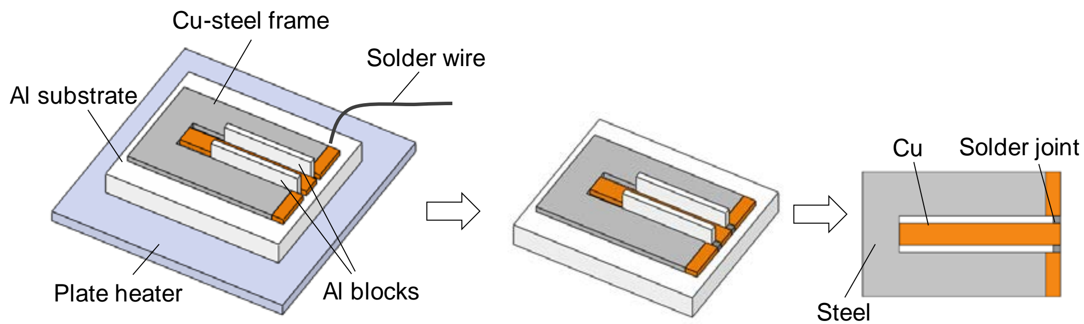

Figure 4-7 Manual soldering procedure

Several SAC305 solder grains can be generated during the solidification process with the large dimensions (1 mm ×1 mm × 1mm). To quantify the deformation behavior of the anisotropic SAC305 solder grain, it is necessary to produce solder joint specimen with only one solder grain. The cooling rate during the solidification process is known to be one of key parameters [54] [1, 5, 61] that influence the grain growth. By controlling the Al substrate thickness and ambient conditions during cooling process, different cooling rates were achieved. Numbers of grains on the surfaces of solder specimens, which were made under different cooling rates, were examined under the polarizing microscope. The results are shown in Figure 4-8 for the different cases where the cooling rate were controlled at: (a) 25 °C/sec, faster cooling using water; (b)

3.5 °C/sec, natural convection cooling; (c) 0.8 °C/sec, natural convection cooling but with a thicker Al substrate; (d) 0.1 °C/min, extremely slow cooling rate. There are several large grains generated under the faster cooling (case a) while many interlaced grains structures were observed under the extremely slow cooling (case d). From this study, it is learned that the solder specimens with a single grain can be obtained when a cooling rate is approximately 0.8 °C/sec. This cooling rate was selected in this study to make specimen solder joints with a single solder grain.

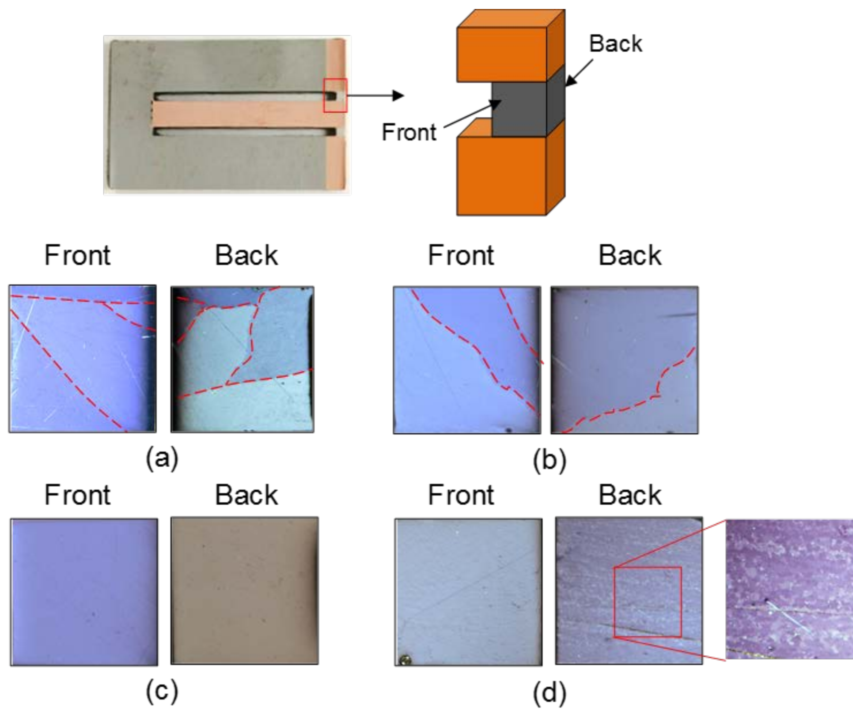

Figure 4-8 Number of grain on SAC305 solder joints under polarizing microscope made at different cooling rates: (a) 25 °C/sec, (b) 3.5 °C/sec, (c) 0.8 °C/sec and (d) 0.1 °C/min

During solder reflow, a thermocouple was attached on the surface of specimen to monitor the temperature. The specimen temperature during the manual soldering process is shown in Figure 4-9. When temperature decreased to 190 °C, the solder was completely solidified, and the assembly was moved to a metal heat sink for faster

cooling. Two specimens were fabricated for the moiré experiments. As shown in Figure 4-10, both the upper solder joint (#1) and lower solder joint (#2) in specimen 1 contain a single grain, and in specimen 2, the upper solder joint (#3) contains two grains through the thickness and the lower joint (#4) contains a single grain. The microstructures on specimens were observed using the scanning electron microscope (SEM). A SEM image of solder joint #1 is shown in Figure 4-11.

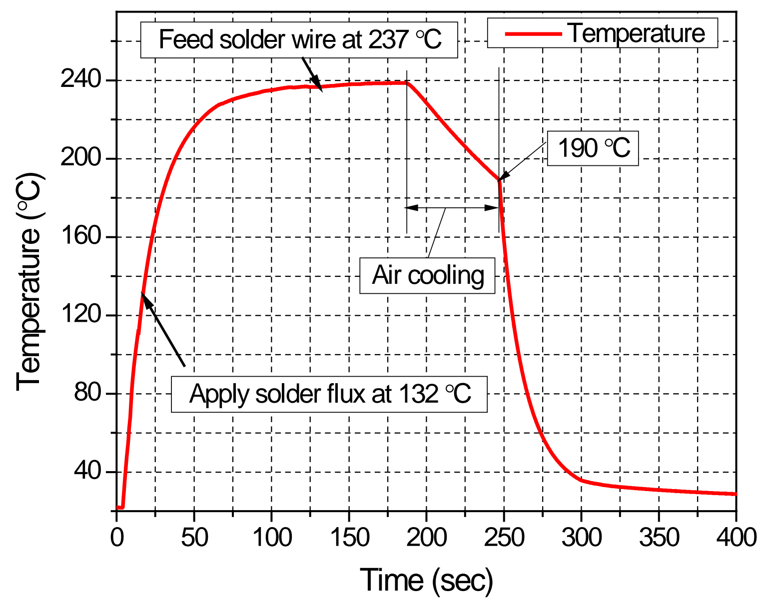

Figure 4-9 Specimen temperature during manual soldering process

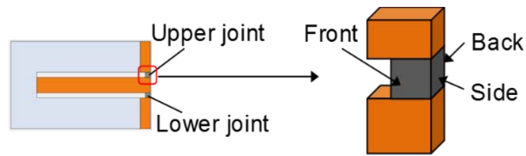

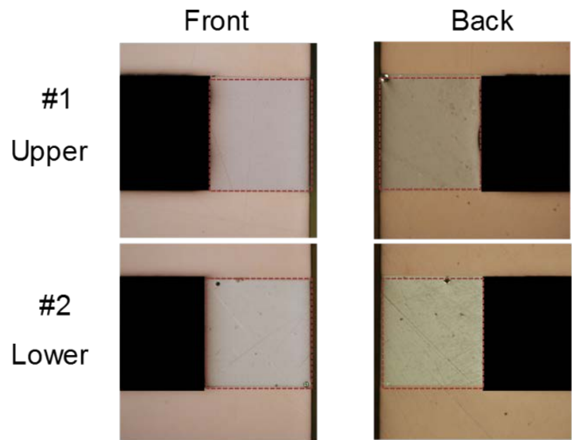

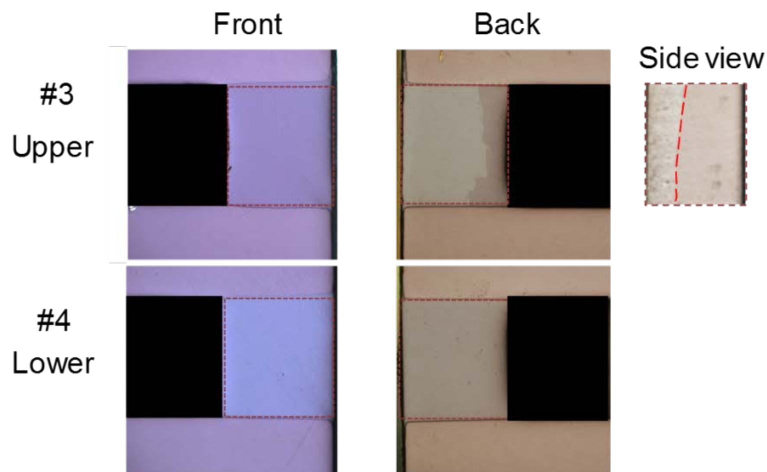

Figure 4-10 Number of grains on the surfaces of solder joints under polarizing microscope: (a) specimen 1 and (b) specimen 2

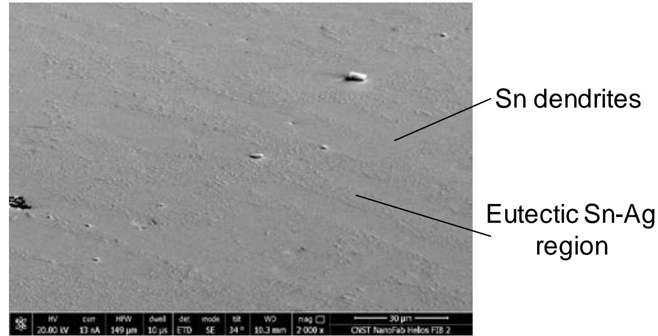

Figure 4-11 Microstructure on the surface of solder joint #1

4.3.2.3. Grain Orientation in Solder Joints

Since the SAC305 solder joint has strong anisotropic mechanical response depending on the Sn grain orientation, it is very important to know the grain orientations of each solder joint in the specimens. Electron backscatter diffraction (EBSD) technique was employed to detect the Sn grain orientation. The technique is a well-established microstructural-crystallographic characterization technique to study any crystalline or polycrystalline material [55].

In this work, the specimens were measured in the FEI Helios NanoLab 600 dual-beam microscope system. The specimen was mounted on a metal stage and placed inside SEM chamber, schematically shown in Figure 4-12, where the specimen coordinate system (*o-xyz*) was labeled. An electron beam scanned the specimen solder surface and the EBSD detector collected the backscattered electrons to form a diffraction pattern from which the grain orientation was determined. The EBSD measurement was made on the front surfaces of each solder joint and the results are shown in Figure 4-13. The EBSD layer images have the uniform color which indicates there is only one Sn grain on the solder surface. The Euler angles (A_1, A_2, A_3) shown

in Figure 4-13 were obtained based on the specimen coordinate *o-xyz*. The specimen coordinate can be transformed to the Sn grain coordinate through three steps of rotations shown in Figure 4-14. The grains orientations for all 4 solder joints are quite different. It is expected the deformation behavior of these solder joints will be very different under the thermal loadings.

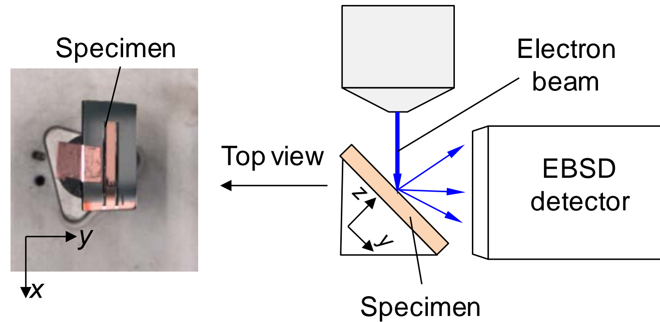

Figure 4-12 Schematic of EBSD measurement for grain orientation

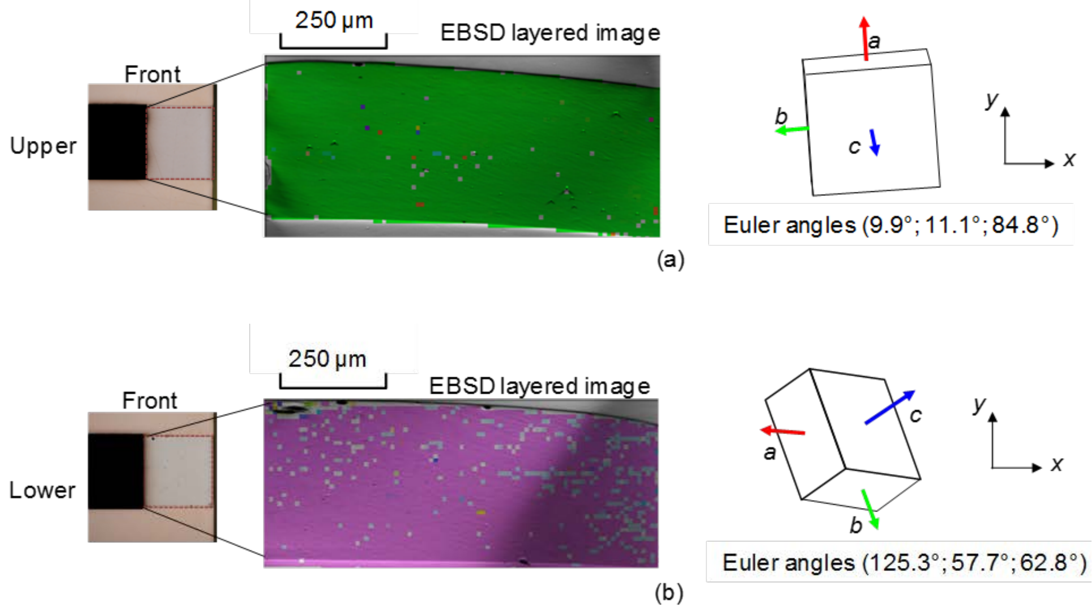

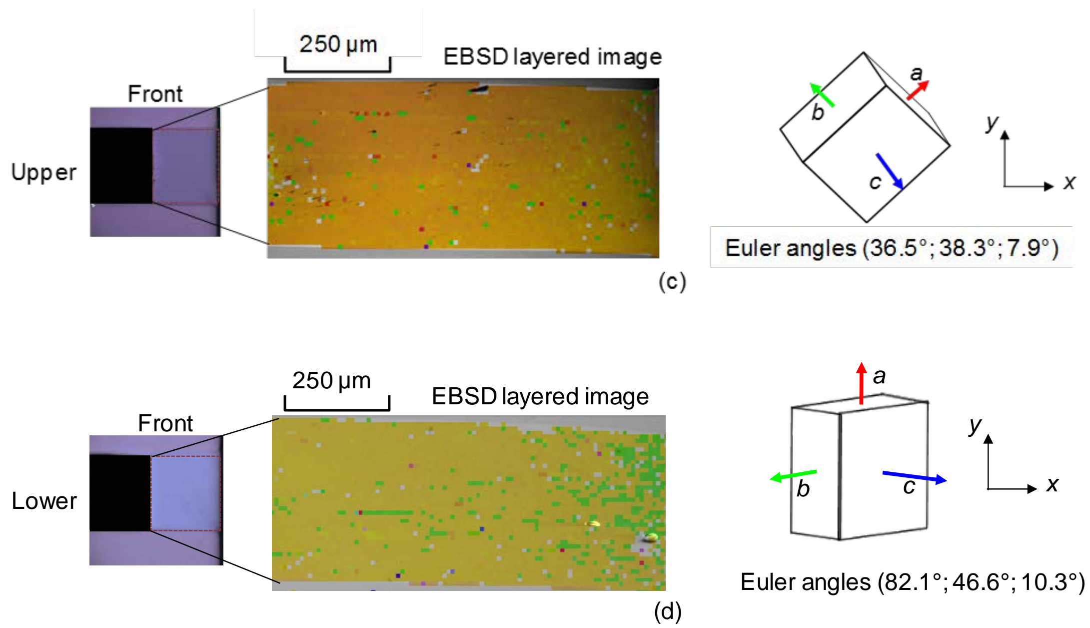

Figure 4-13 EBSD layered images and grain orientations for solder joints: (a) #1, (b) #2, (c) #3 and (d) #4

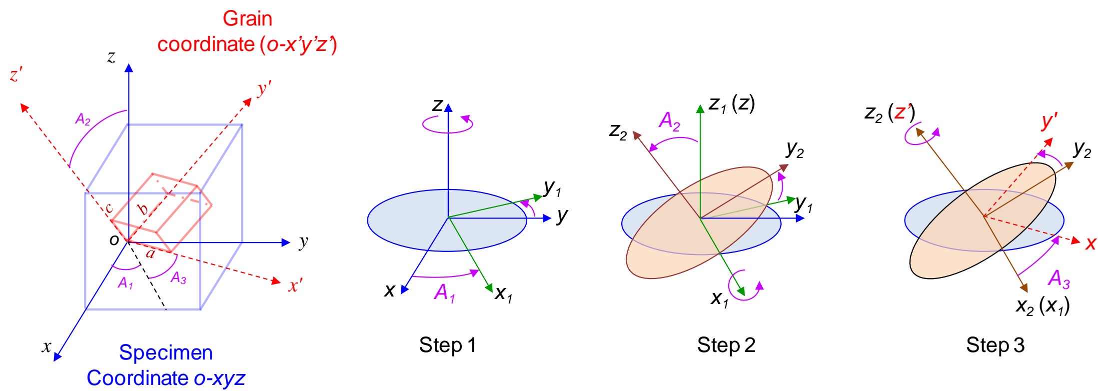

Figure 4-14 Transformation from specimen coordinate to grain coordinate using Euler angles

4.4. Moiré Experiments and Result Analyses

4.4.1. Moiré Experiment

Before the moiré experiments, specimen 1 and 2 were isothermally aged at 0.8 homologous temperature for 100 hours, which is about 125 °C for SAC305 material.

This preconditioning was carried out to stabilize the solder microstructure and relax the residual stresses from the reflow and polishing process. It also can be found in other research groups [1, 15].

After preconditioning, the specimens were cooled down to room temperature and slightly polished to remove the oxidized surface layer. The specimen gratings were replicated on the front surfaces of the two specimens at room temperature (20 °C). The specimen was placed on the top surface of thermal head which consists of high performance thermo-electric cooler modules inside the conduction chamber, shown in Figure 4-15. The null fields were examined carefully at room temperature first to ensure there was virtually no deformation introduced during specimen grating replication. Then, the thermal cycling condition was applied to the specimen. Detailed in-situ deformations of the specimen during the cycling were documented by the advanced moiré interferometry system.

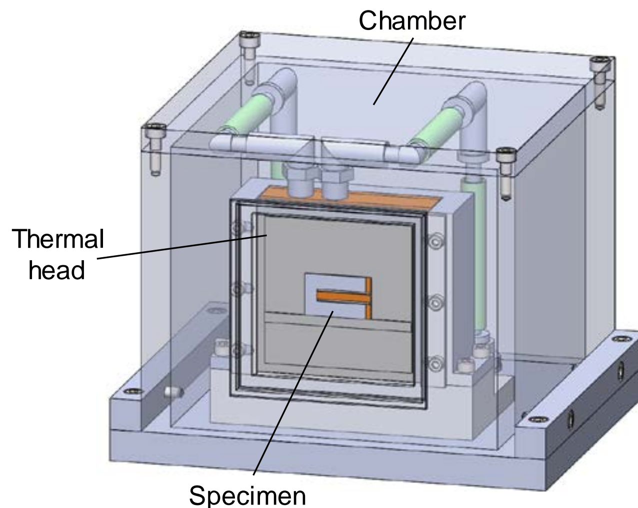

Figure 4-15 Solder specimen inside conduction chamber

Since the specimen is very thin and has high thermal conductivity, the accurate thermal cycling can be well controlled by the system. The specimen was subjected to a thermal excursion of -40 °C to 125 °C with a ramp rate 12 °C /min. The dwell time is 10 min at the peak (-40 °C and 125 °C) temperatures and 5 min at 20 °C. There are total 6 cycles. The actual thermal loading recorded during experiment is shown in Figure 4-16. The deformations of the whole specimen and the local solder joints were captured by the zoom lens and microscope objective, respectively, at the dwell temperature 125, -40 and 20 °C during each cycle. The phase-shifted fringe patterns were captured for the post processing of displacement fields.

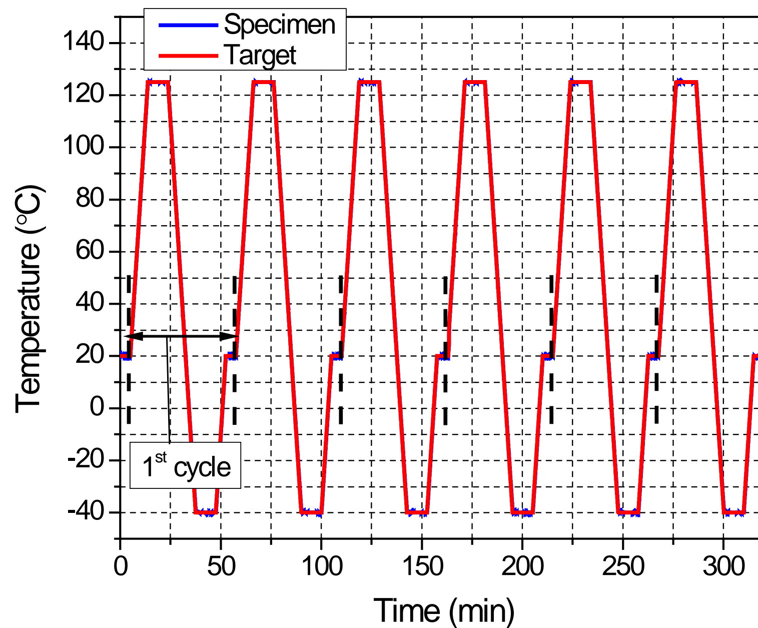

Figure 4-16 Temperature profile of thermal cycling loading applied to the specimen

4.4.2. Experimental Results and Analyses

The fringe patterns of the whole specimen and zoom in area marked by a red box during the 1st cycle are shown in Figure 4-17 and Figure 4-18, where the contour

interval is 417 nm/fringe. The fringe patterns show that the shear deformation is dominant, but each solder joint has quite different fringe patterns because of the different grain orientations.

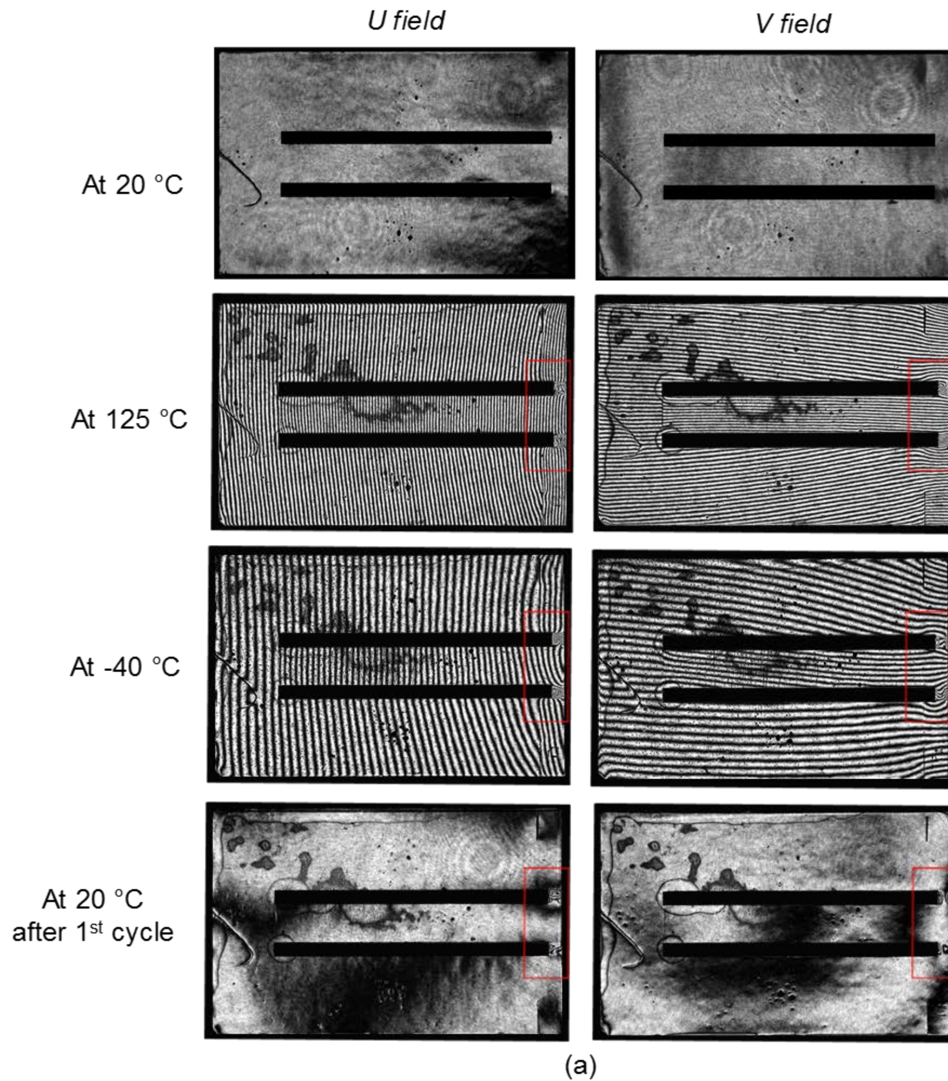

(a)

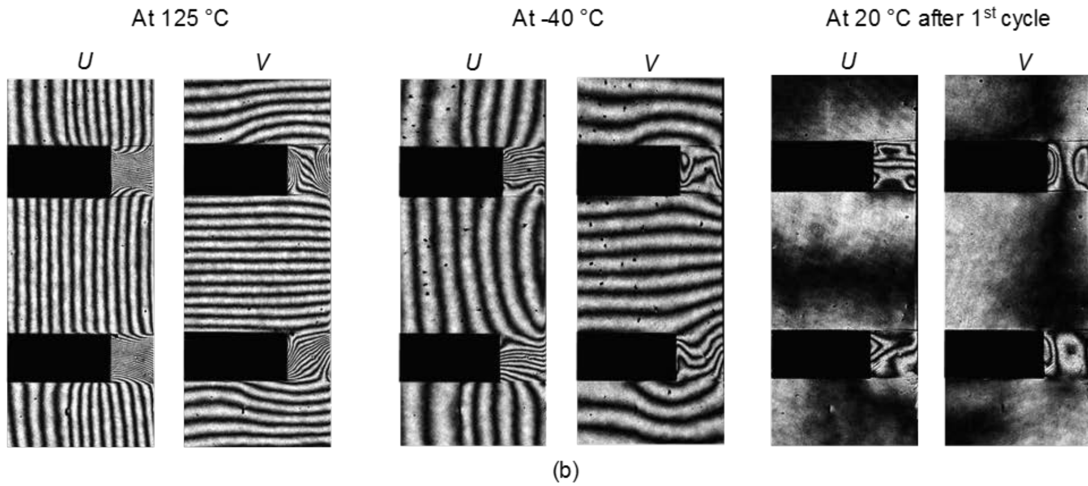

Figure 4-17 Representative fringe patterns of specimen 1 captured during the 1st cycle by zoom lens: (a) whole field, and (b) local solder joint and adjacent area

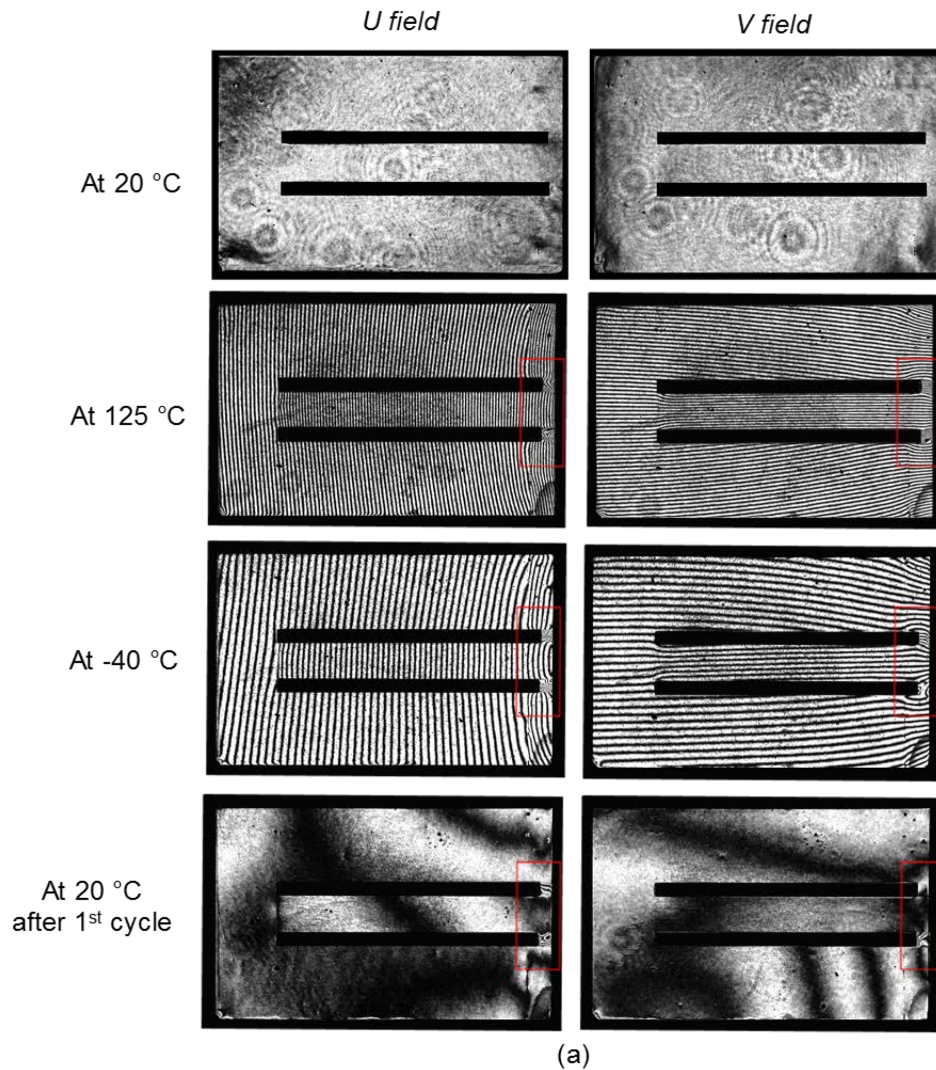

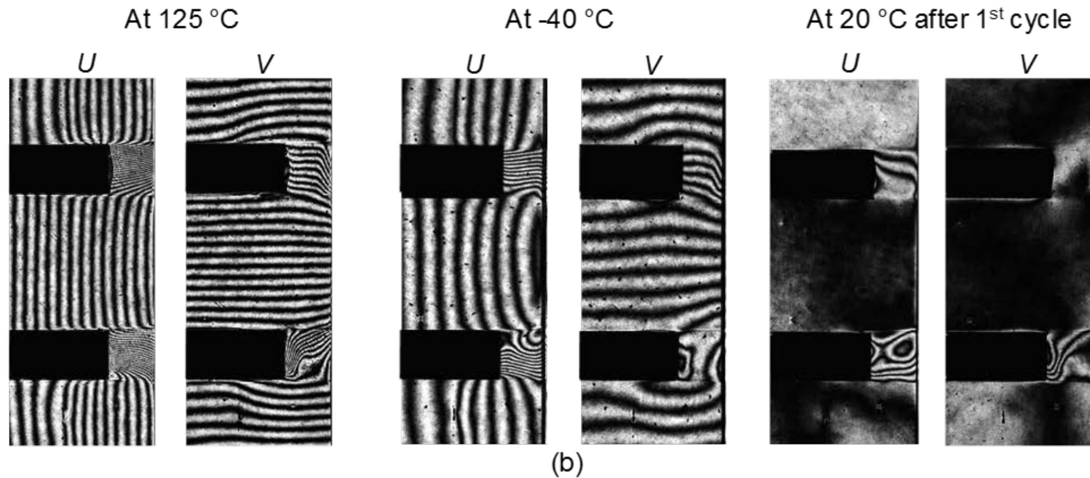

Figure 4-18 Representative fringe patterns of specimen 2 captured during the 1st cycle by zoom lens: (a) whole field, and (b) local solder joint and adjacent area

Fringe pattern evolutions during the thermal cycling for each solder joints are summarized in Figure 4-19, Figure 4-20 and Figure 4-21. The in-situ deformation evolution is clearly observed. At the same temperature, the number of fringes kept increasing when solder joints experienced more thermal cycles that is due to the accumulated deformation. Except the upper solder joint (#3) in the specimen 2, all the solder joints have very complex and non-uniform fringe patterns. The apparent deformation based on the well-defined fringe patterns were analyzed using the moiré software developed by the LOMSS lab of UMD [62]. Four phase-shifted fringe patterns are used to calculate the displacement fields [63]. But, it should be noted that moiré interferometry measures relative deformations. The stress-free temperature of the specimen was assumed to be 125 °C after preconditioning.

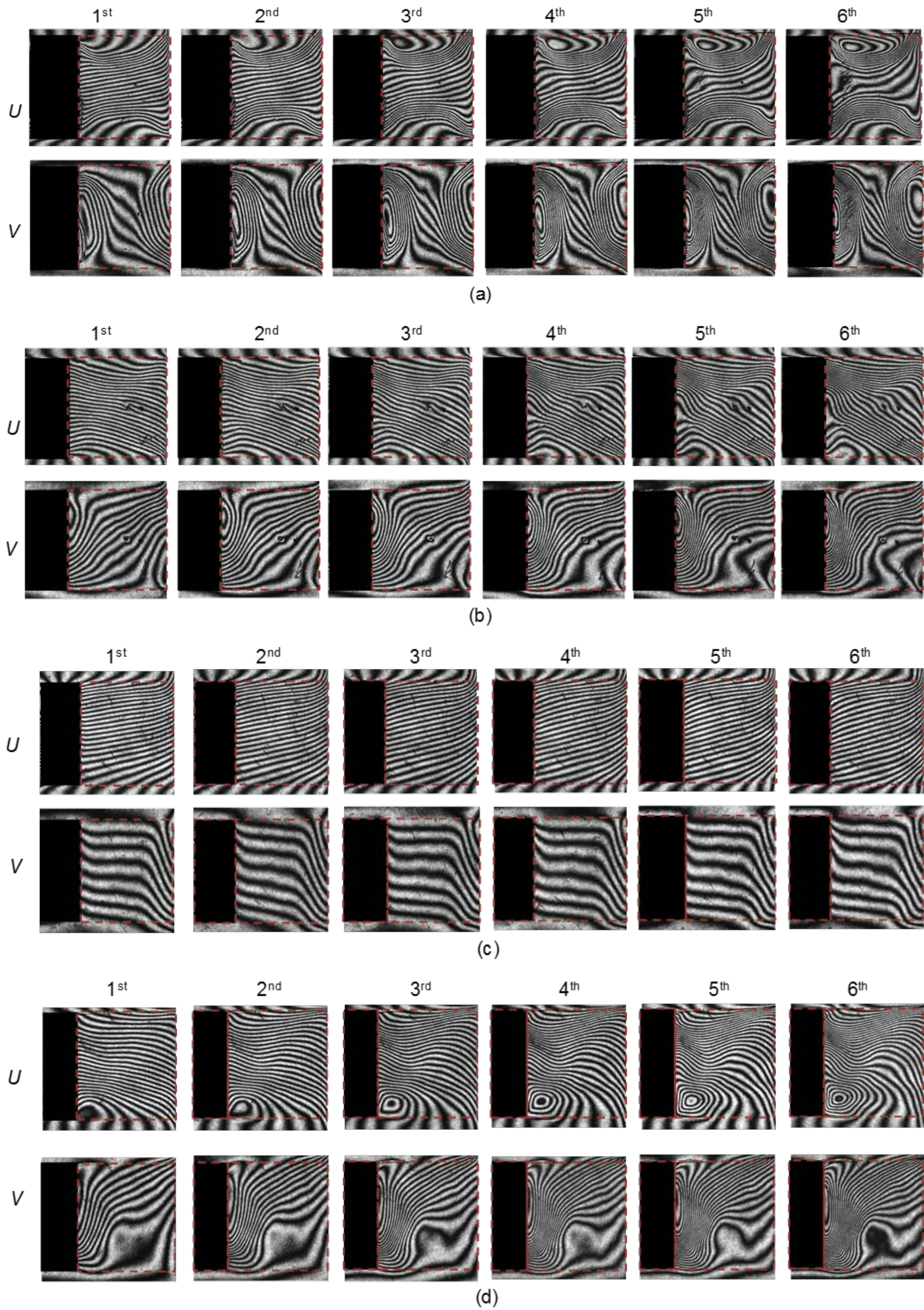

Figure 4-19 Fringe pattern evolution of solder joints during the six thermal cycles at 125 °C: (a) #1, (b) #2, (c) #3 and (d) #4

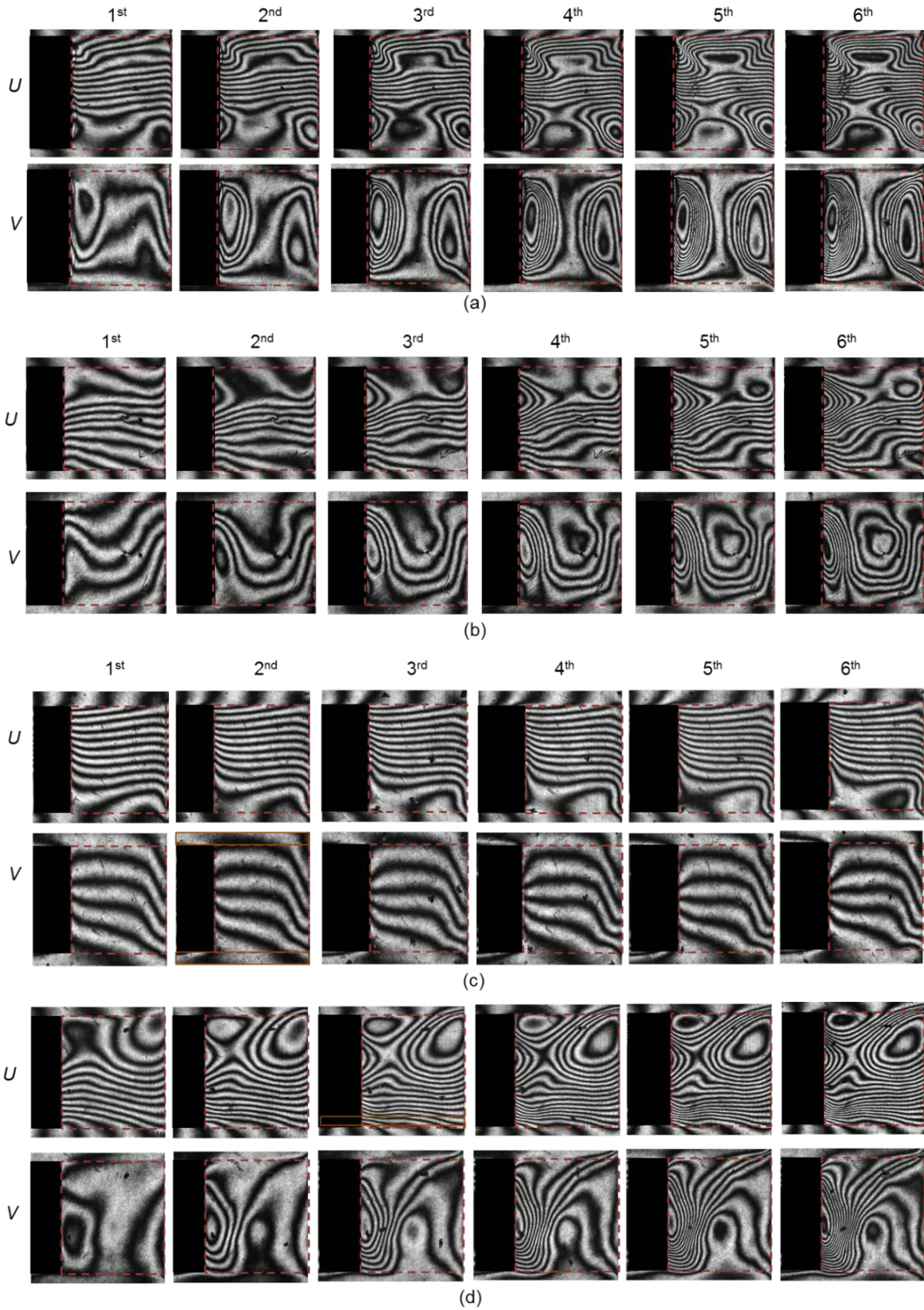

Figure 4-20 Fringe pattern evolution of solder joints during the six thermal cycles at -40 °C: (a) #1, (b) #2, (c) #3 and (d) #4

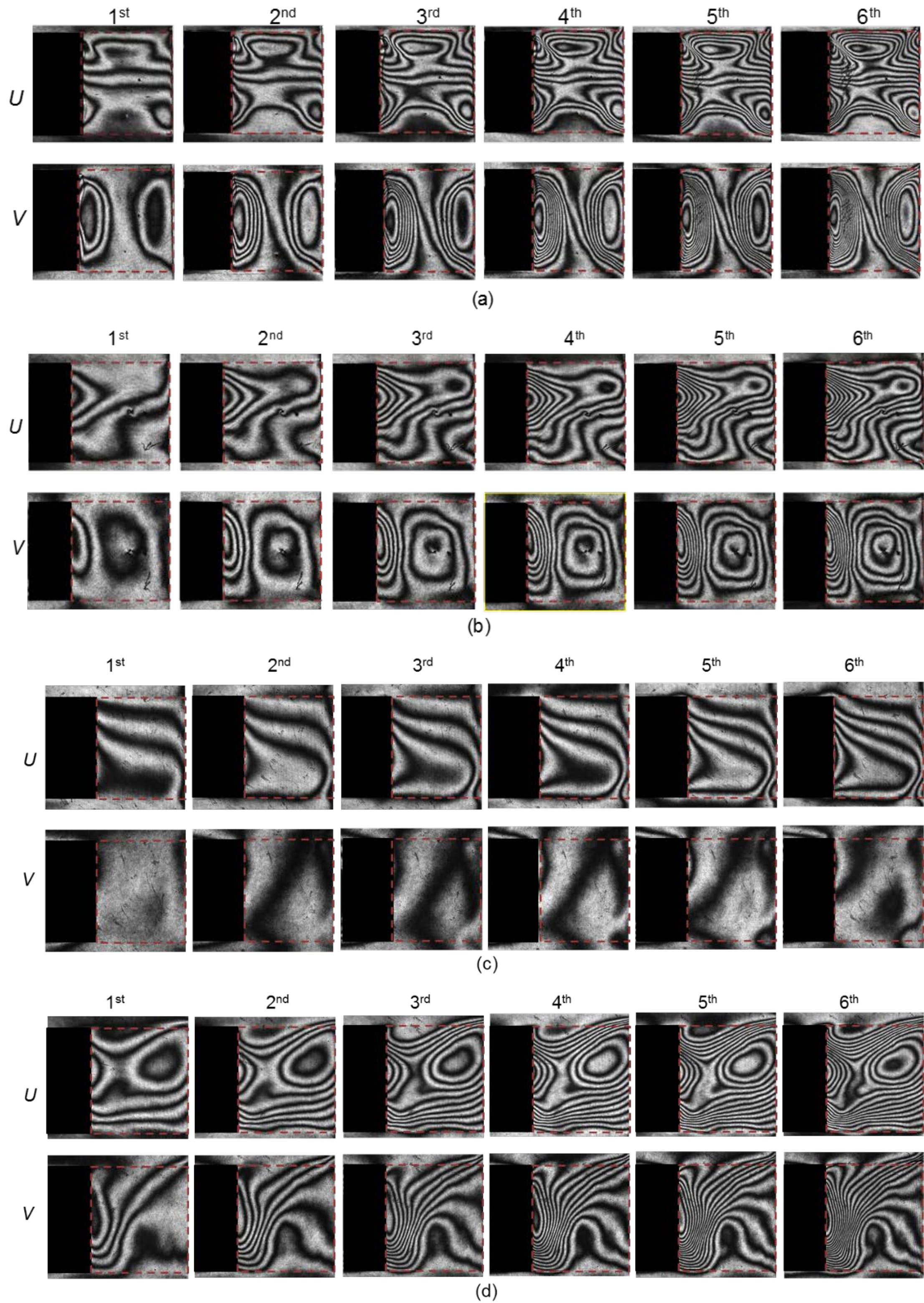

Figure 4-21 Fringe pattern evolution of solder joints after each cycle at 20 °C: (a) #1, (b) #2, (c) #3 and (d) #4

Evolutions of u_x displacements of solder joint #1 at 20 °C and 125 °C during each cycle were obtained based the U field fringe patterns and the results are shown Figure 4-22. Only the displacement at 1st cycle (Figure 4-22 c) directly represents the relative deformation while temperature increased from 20 °C to 125 °C since null fields were tuned at the very beginning (0th, Figure 4-22 a). During other cycles, the relative deformation can be obtained by subtracting the corresponding displacement field at 125 °C from the displacement field at 20 °C. The deformed configurations of the solder joints were constructed based on the u_x and u_y displacement data.

Figure 4-23 shows the apparent deformed configurations of solder joint #1 at 125 °C and -40 °C, where the blue dash line indicates the original shape of solder joint and red line is the deformed solder joint. The deformation was magnified X25 to highlight the important deformation modes. Similarly, the relative deformations for other solder joints were obtained.

The accumulated damage inside the solder joint is one of the most critical parameters for the reliability assessment. The fringe patterns captured at 20 °C (Figure 4-21) after each cycle represent the actual accumulated deformations. To better understand the accumulated damage in each solder joint, the displacement fields and strain fields were calculated using the software. The results of deformations after the 6th cycle are shown in Figure 4-24 and Figure 4-25 for each solder joints. The deformation magnitude and modes are very different. The strain concentrations presented at different locations in each joint. Among the four solder joints, the solder joint #1 (Figure 4-24 (a) and Figure 4-25 (a)) has the largest accumulated deformation,

and the normal strain values are concentrated at the four corners along the diagonal directions.

The deformed configurations (absolute accumulated deformations) at 20 °C were constructed for all the solder joints. Figure 4-26 illustrates the deformed configurations of each solder joint after 1st, 3rd and 6th thermal cycle. It shows that the solder joint #1 and #4 have large accumulated deformation. The deformation modes are different for all the solder joints.

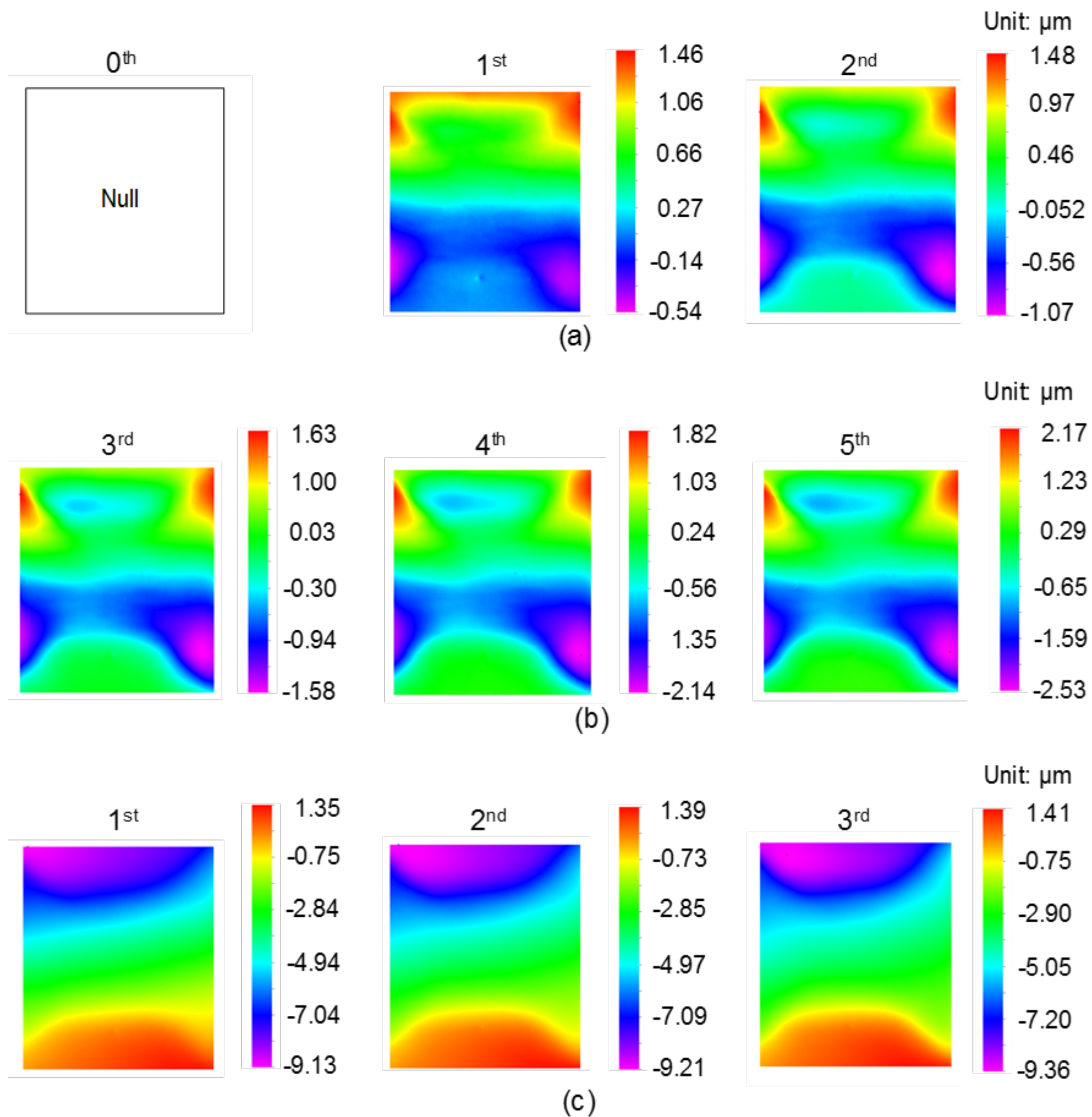

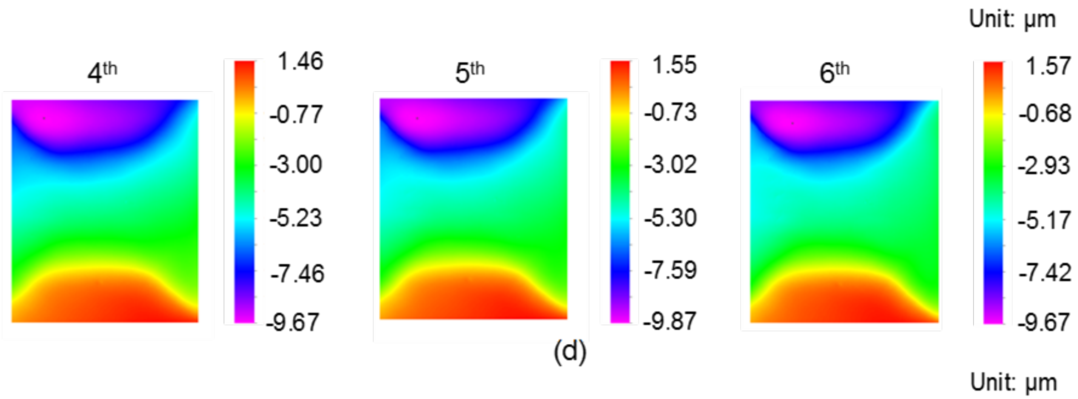

Figure 4-22 u_x displacement evolution of the solder joint #1 during each cycle at: 20 °C (a) (b), and 125 °C (c) (d)

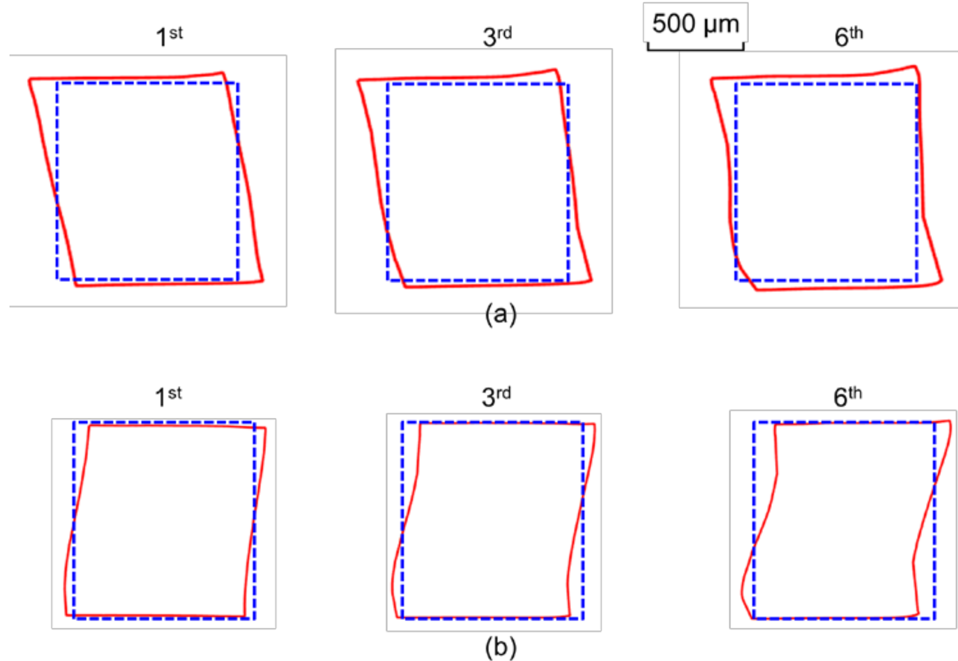

Figure 4-23 Deformed configurations (X25) of solder joint # 1 recorded at different cycles: (a) at 125 °C and (b) at -40 °C

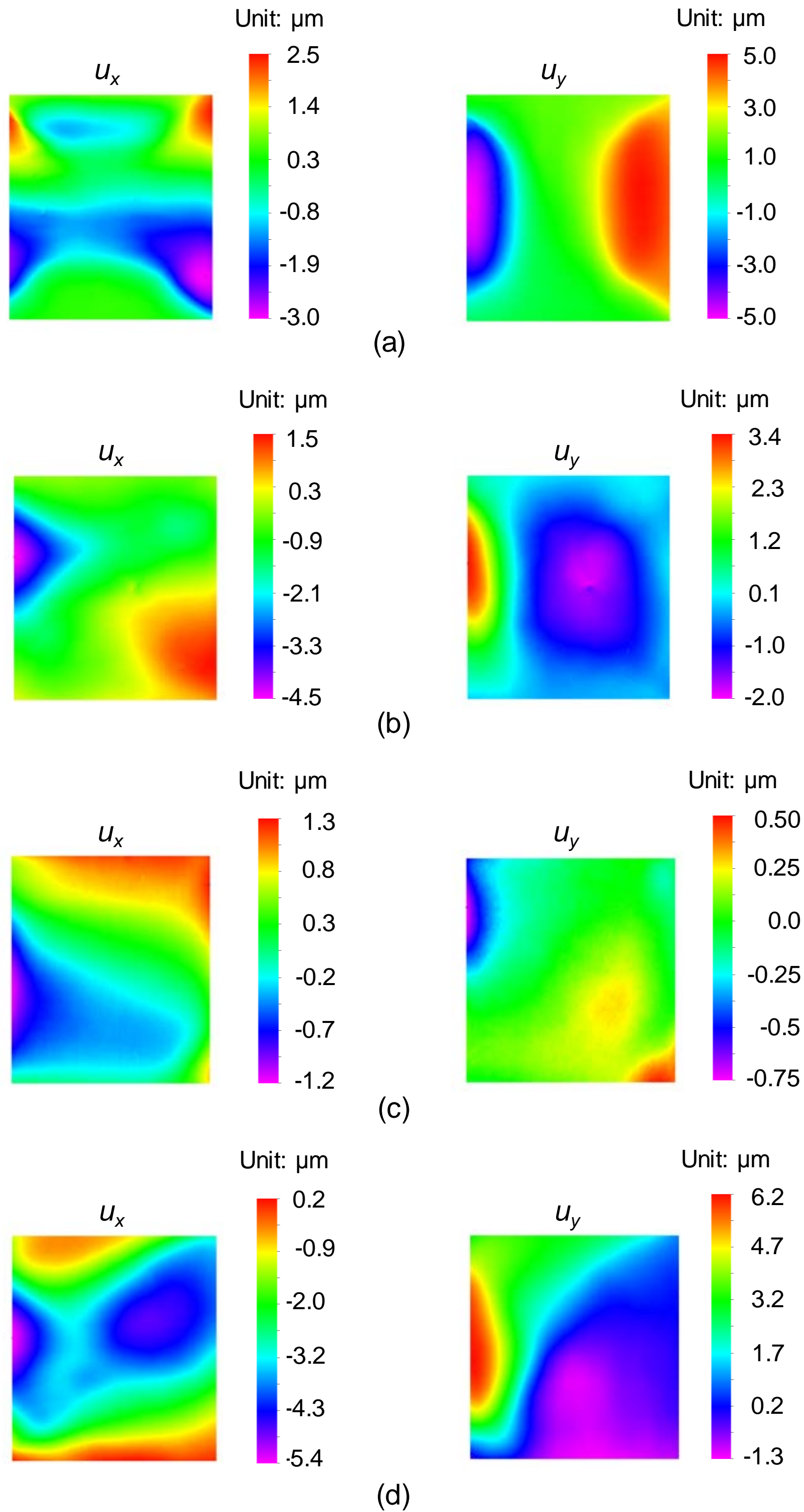

Figure 4-24 Displacements for each solder joint at 20 °C after the 6th thermal cycle: (a) #1, (b) #2, (c) #3 and (d) #4

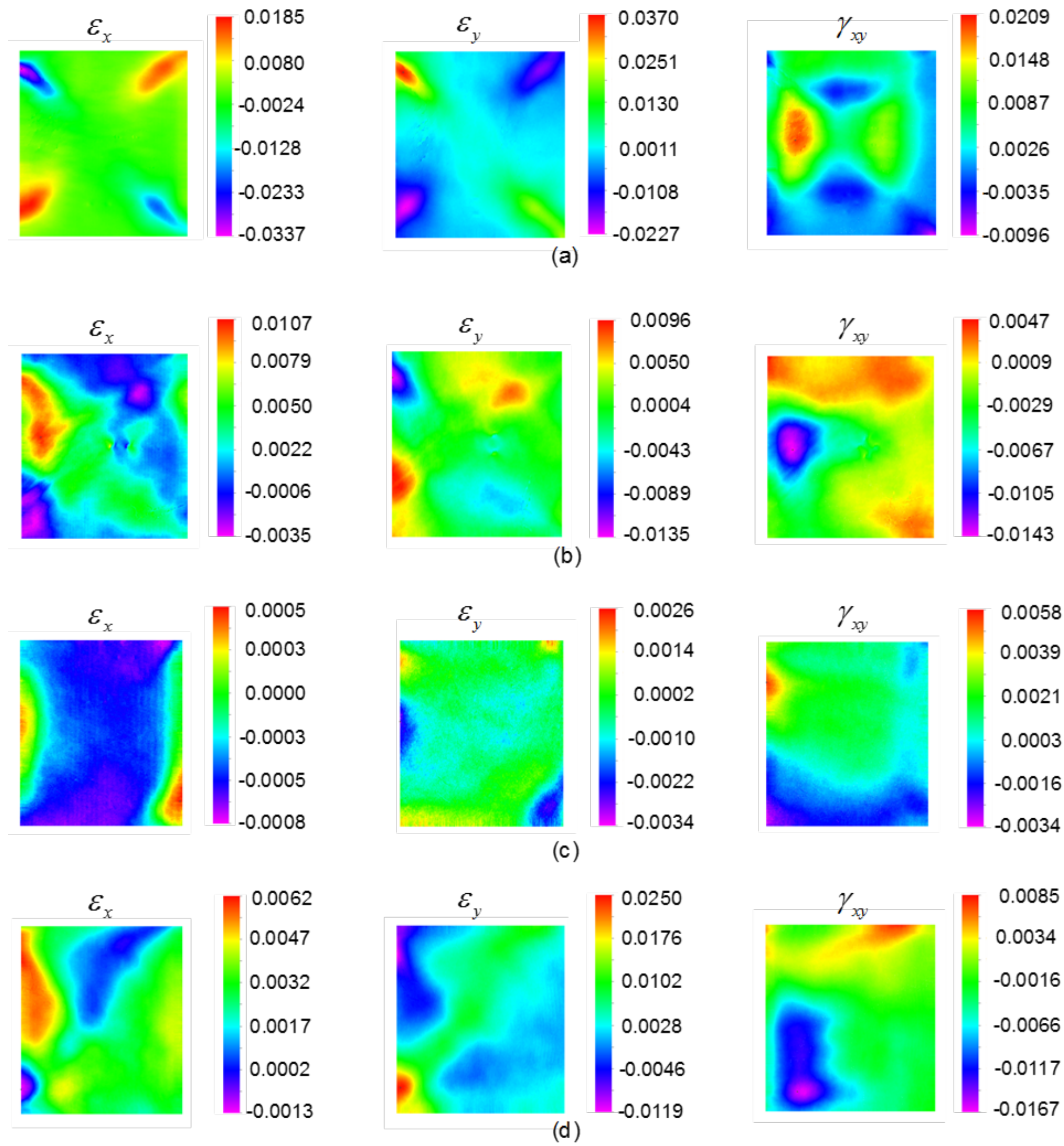

Figure 4-25 Strains for each solder joint at 20 C after the 6th thermal cycle: (a) #1, (b) #2, (c) #2 and (d) #4

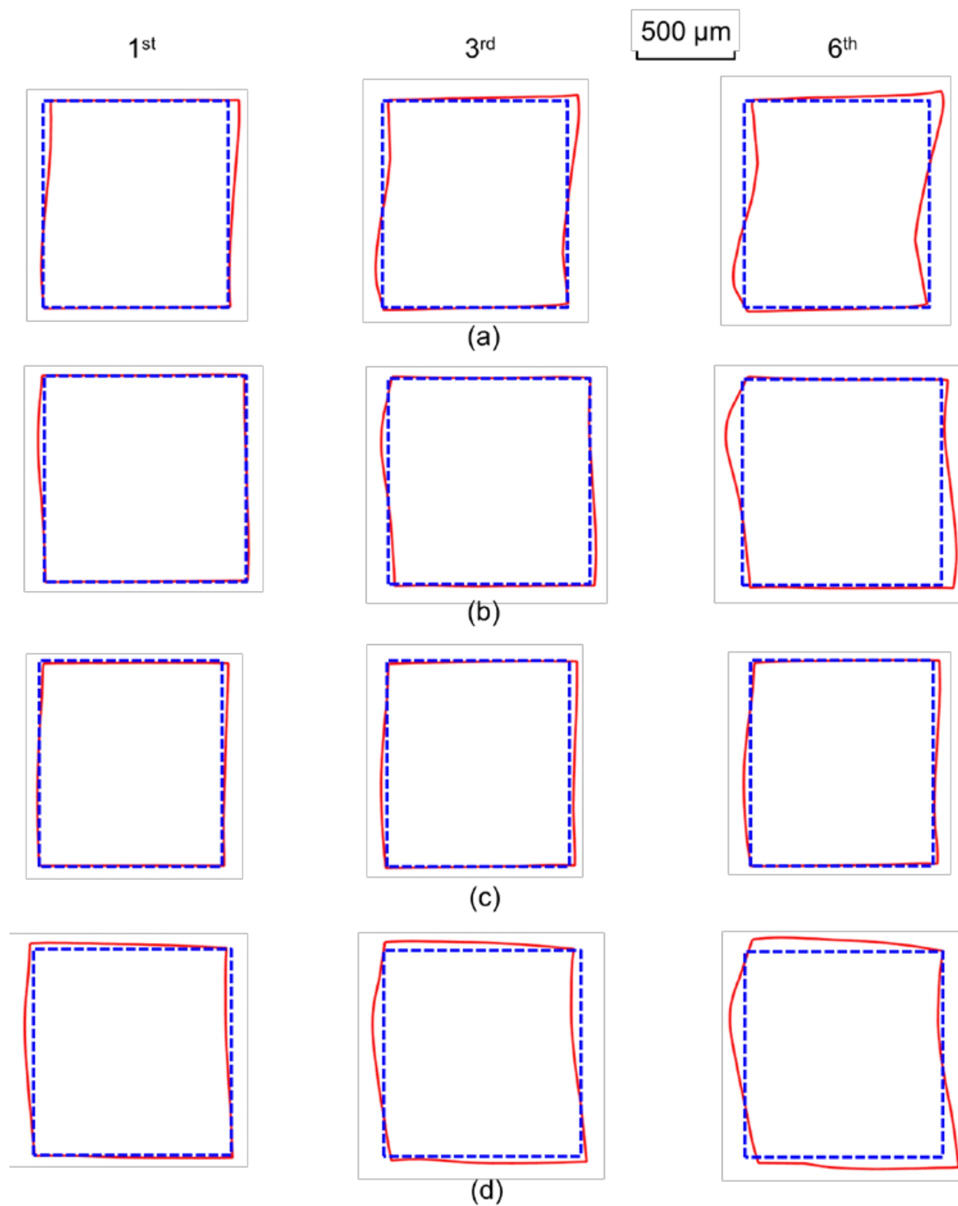

Figure 4-26 Deformed configurations (X25) of solder joints at 20 °C after thermal cycling: (a) #1, (b) #2, (c) #3 and (d) #4

4.5. Discussion

As expected, the SAC305 solder joints showed quite different thermo-mechanical deformation behavior during the thermal cycling due to the different solder grain orientations. There are several empirical solder models to predict the solder

deformation behavior. Two main categories of the empirical models are partitioned model and unified Anand model. The available constitutive properties of SAC305 used in these models are summarized in the Appendix II. They are easy to be implemented in FEA modeling and convenient for analyzing solder deformations in electronic packaging components and assemblies. But, the SAC305 solder is characterized as homogenous and isotropic material in these models. They are not sufficient to predict the accurate deformations of the SAC305 solder joints.

To understand the grain orientation dependent deformation behavior, an elastic modeling was carried out in ANSYS Workbench. β-Sn crystal has BCT structure, shown in Figure 3-1. It has strong orthotropic elastic moduli [64, 65]. Previous experimental study shows that SAC305 grain has transverse isotropic CTE values. In the grain coordinate, the CTE on $x'y'$ plane is a constant, α_a, and CTE along c-axis (z') is another constant, α_c. The elastic constants of pure β-Sn crystal [64] and transverse isotropic CTE values of SAC305 grain were used in the modeling and are summarized in Table 4-3 and Table 4-4. It is noted that these properties are defined in the solder grain coordinate.

A full model was established for specimen 1, shown in Figure 4-27. The grain coordinates were created for each solder joint based on the EBSD result (Figure 4-13). The anisotropic elastic constants and CTE values were assigned to the grain coordinates for each joint. The stress free temperate was set at 20 °C and the deformations of the solder joints at 125 °C are shown in Figure 4-28. The difference of deformations at the two solder joints is evident. Although, the Sn grain is the matrix in SAC305 solder joint, its microstructure is very different from pure β-Sn crystal. It is expected the

anisotropic elasticity, plasticity and creep are different from β-Sn crystal. However, there is still lack of material properties of the SAC305 considering its anisotropic characteristic for accurate deformation prediction.

Table 4-3 Orthotropic elastic constants (components of stiffness tensor) of β-Sn crystal (unit: GPa)

C_{11}	C_{33}	C_{44}	C_{66}	C_{12}	C_{13}
78.7	108.0	18.9	21.0	70.6	60.6

Table 4-4 Transverse isotropic CTE values of SAC305 grain

α_a	α_c
17.28+0.0158*T(°C)	33.18+0.0292*T(°C)

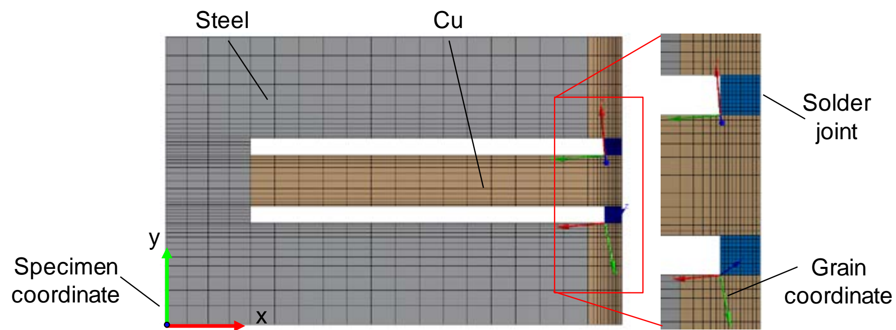

Figure 4-27 FEA model and grain coordinate

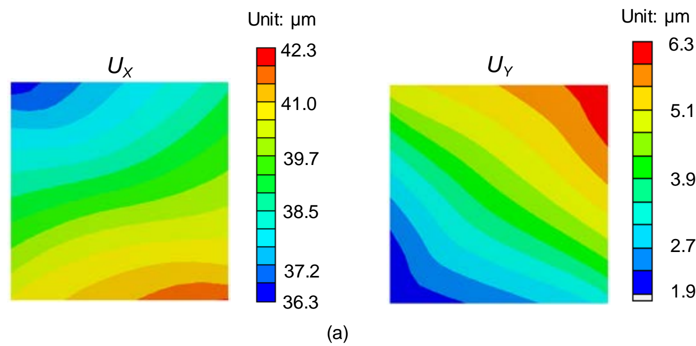

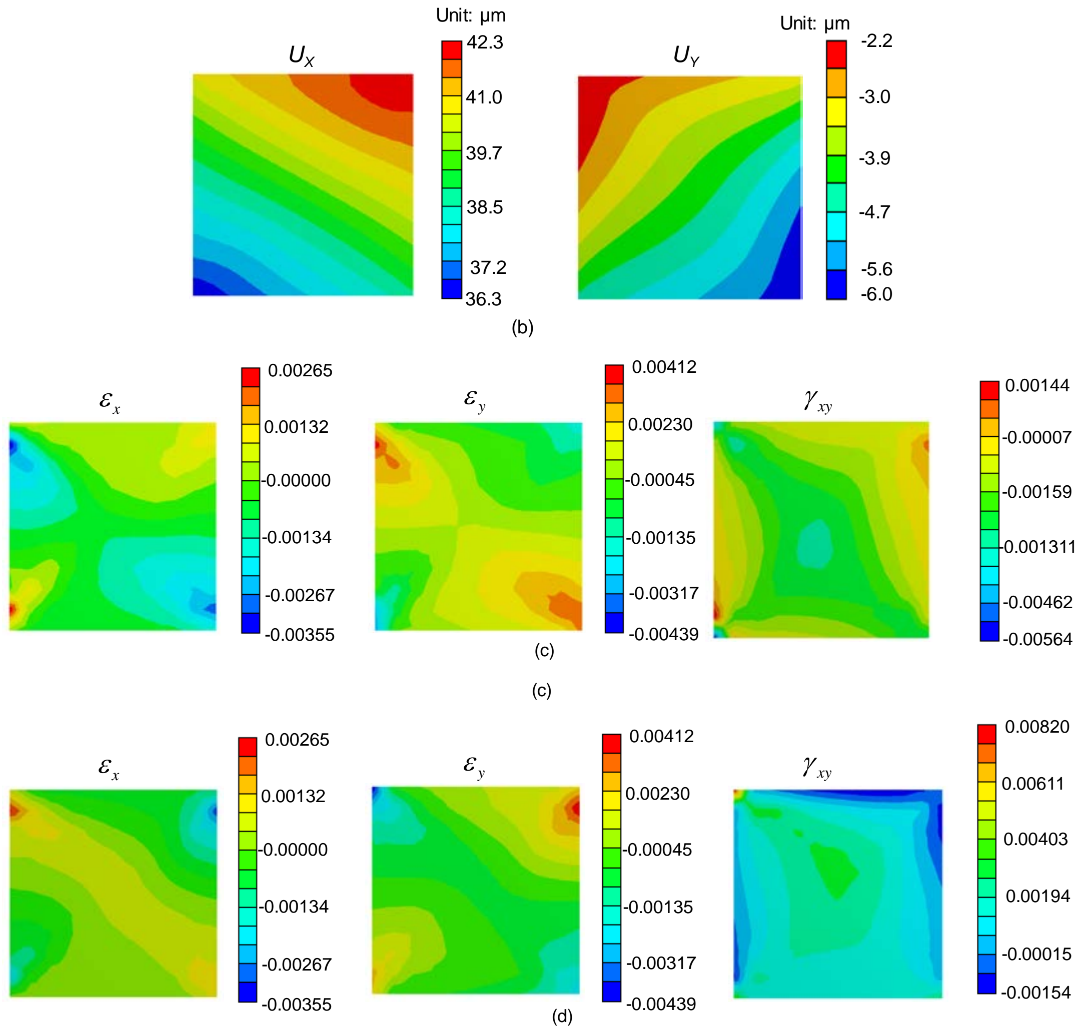

Figure 4-28 FEA results of deformations at 125 C: displacements of upper joint (a) and lower joint (b), strains of upper joint (c) and lower joint (d)

4.6. Conclusion

The in-situ thermo-mechanical behavior of SAC305 solder joint was studied in the grain level. A novel specimen frame was designed to control the loading on a single solder grain specimen under the well-controlled thermal cycling. The detailed evolutions of displacement and accumulated deformation at the solder grain were documented. The deformations of each solder joints were analyzed to reveal the grain orientation dependent thermo-mechanical behavior. The methodology and

experimental data shown in this work can lead more accurate anisotropic constitutive properties of Sn-based Pb-free solder alloys.

Part II: Advancement for Experimental Analyses of Micromechanical Deformations

Chapter 5 Advanced Immersion Microscopic Moiré Interferometer

5.1. Introduction

Special considerations arise for the deformation measurements of tiny specimens or tiny regions of large specimens. The relative displacement within a small field of view will be small, while, the strain can be large. Moiré interferometer with basic sensitivity 417 nm/fringe discussed in previous chapter may not be able to capture enough number of fringes to map the accurate deformation over a tiny area of the microstructures. A displacement measurement tool with higher sensitivity and spatial resolution is required.

The microscopic moiré interferometry (MMI) has been adopted for this kind of applications [22, 24, 52, 66]. It is an extension of moiré interferometry but with greater sensitivity and higher spatial resolution. In this technique, an immersion moiré interferometer is used to double the basic sensitivity [41, 66]. A microscope objective lens is employed to accomplish the spatial resolution. The sensitivity can be further enhanced by using the optical/digital fringe multiplication (O/DFM) technique, which can generates a displacement contour map with β times as many fringe contours as the original moiré fringe patterns [44], while, retaining the high spatial resolution. In the current practice, the contour interval of 17.4 nm has been achieved with β = 12. However, there are some limitations of the current practice of MMI, which keep it from wide applications. The objective of this chapter is to development an enhanced immersion MMI to cope with these limitations for wider application for microstructure deformation analyses.

5.2. Principle of Immersion MMI and Limitations of Current MMI System

The displacement sensitivity of the moiré system is equal to the virtual reference grating f. It is determined by the initial frequency of the specimen grating f_s and the incident angle α of the collimated beams. It can be calculated by:

$$f = 2mf_s = \frac{2m\sin\alpha}{\lambda} \tag{5-1}$$

where $\pm m$ are the diffraction order of two beams, λ is the wavelength of the light source.

According to Eq. (5-1), the sensitivity approaches the theoretical limit when α approaches 90°. However, the increase is not substantial by using larger angle because $\sin\alpha$ already reaches 0.9 when $\alpha = 64°$. Instead, wavelength is manipulated in the immersion moiré interferometer to increase the sensitivity effectively [66].

5.2.1. Principle and Implementation of Immersion MMI

One implementation of immersion interferometer, made of BK7 glass, is illustrated in Figure 5-1 [41, 66]. There is a layer of refractive medium (immersion fluid) between the interferometer and specimen grating. Inside the interferometer, a portion (A) of the collimated beam is reflected by the mirrorized surface and intersects with the portion B. The frequency, f_m, of a virtual reference grating in a refractive medium can be expressed as

$$f_m = \frac{2\sin\alpha}{\lambda_m} = \frac{2n\sin\alpha}{\lambda} \tag{5-2}$$

where, λ is the wavelength in air, n is the refractive index of medium, λ_m is the wavelength in the medium. With $\lambda = 514$ nm (in air), $\alpha = 54.2°$ and $n = 1.52$, the virtual reference grating of 4800 lines/mm is produced. For this reference grating, the

ideal specimen grating frequency would be 2400 lines/mm using in its ±1 diffraction order. The ±2 diffraction order of the grating of 1200 lines/mm was used in the actual implementation of the MMI because of its availability [66].

The interferometer is connect to a phase shifting device using a piezoelectric actuator. A series of shifted moiré patterns are recorded by the CCD camera. As illustrated in Figure 5-2, each fringe pattern is different from its neighbor with a phase difference of $2\pi / \beta$, but they all represent the same displacement field. By using O/DFM technique, these patterns can be converted into a displacement count maps containing β times as many fringe contours as the original moiré fringe patterns.

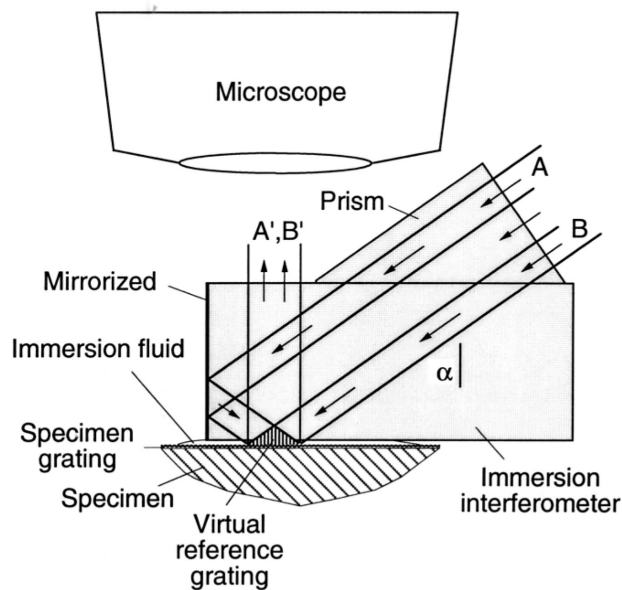

(a)

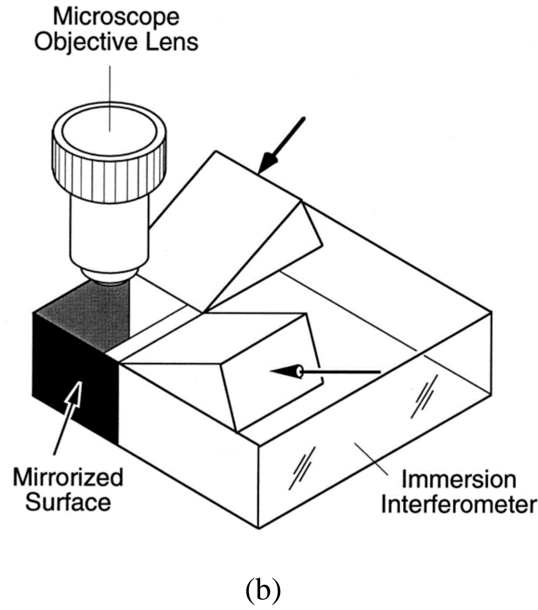

(b)

Figure 5-1 Implementation of immersion interferometer [41, 66]: (a) Optical configuration, (b) four-beam immersion interferometer

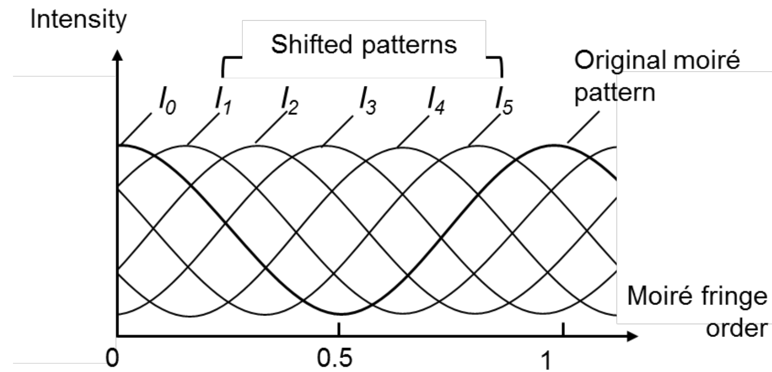

Figure 5-2 Intensity of phase shifted fringe patterns with $\beta = 6$ [41]

5.2.2. Limitations of the current MMI system

The practice of the current MMI system has been limited due to the following limitations:

(1) As shown in Figure 5-1, the optical configuration uses one beam but creates two beams using a mirrorized surface. This compact design have two limitations.

a) The system is polarization-sensitive. The mirror surface causes a left to right reversal of the plane of polarization. When the plan of polarization is perpendicular or parallel to the specimen grating lines, the reversal does not affect the plane of polarization. Therefore, these two beams remain mutually coherent and generate fringe patterns with high contrast. However, for other angles of polarization, the two diffracted beams from the specimen grating will have different planes of polarization, which reduces the coherence, thus reducing visibility of fringe patterns.

b) Shear gradients of *U* and *V* field patterns cannot be adjusted independently. The immersion interferometer is fabricated from a corner cube prism, which has two orthogonal surfaces. The cross line specimen gratings are supposed to be perpendicular to each other, but a typical fabrication process of a cross line grating often produces a tiny angle between two grating lines. A small angle, ψ, (Figure 5-3) produces an error in shear strain by $\gamma_{xy}^{error} = f_m \psi$.

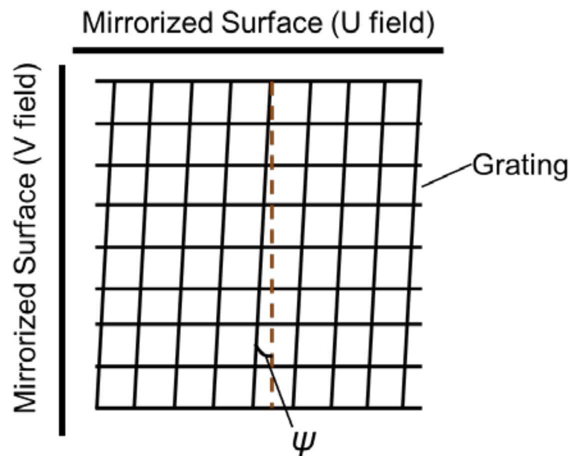

Figure 5-3 Specimen gratings with a small angle error

(2) The fringe shifting mechanism in the original MMI is extremely vibration-sensitive because the immersion interferometer is directly attached to a mechanical

phase-shifting device using a piezoelectric actuator. This limits the fringe multiplication of O/DFM method, which requires very accurate phase shifting amount.

5.3. Development of Advanced Immersion MMI

An advanced immersion MMI is developed to: (1) relax the requirements of light source and specimen grating, (2) provide a robust phase shifting device to cope with environment disturbances during operation, and, (3) offer an imaging system with higher spatial resolution and magnification. The system is the combination of achromatic moiré concept and immersion interferometer.

5.3.1. Optical Configuration

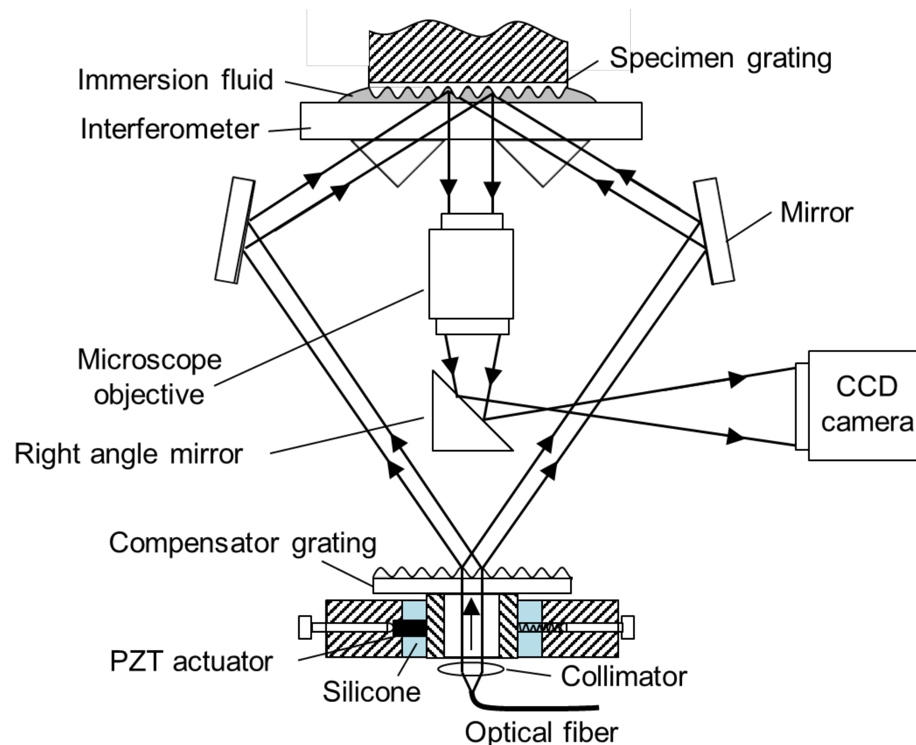

Figure 5-4 Optical configuration of enhanced MMI

The optical configuration of the proposed MMI is illustrated in Figure 5-4. A collimated laser light transmits a cross-line compensator grating. Four diffracted

beams in the ±1 diffraction order are redirected by mirrors into the interferometer assembly made of BK7 glass. Two beams, mirrors and prisms are shown in Figure 5-4. The other set is located at the perpendicular plane.

Four beams, generating *U* and *V* field fringe patterns, respectively, are diffracted from the specimen grating, which are collected by a microscope objective and redirected by a right angle prism mirror to a CCD camera. The enhanced MMI system is insensitive to the polarization of laser light source due to the symmetric design. Four mirrors are designed to tune the beams, independently. Therefore, the null-field can be adjusted readily to eliminate the shear strain error mentioned in the current MMI system.

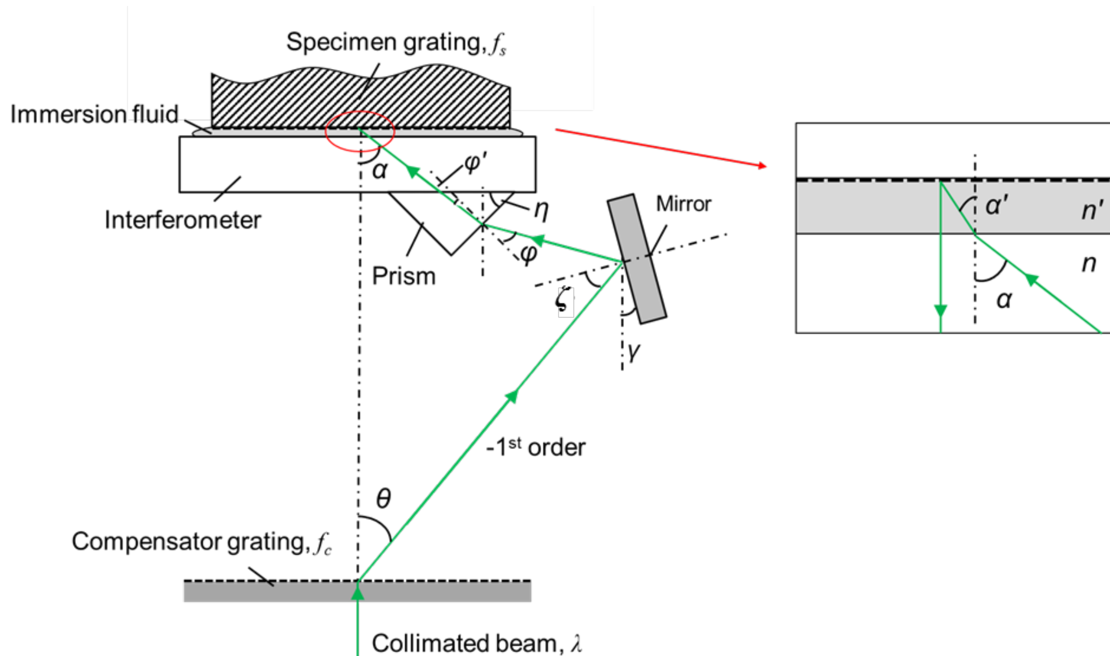

Figure 5-5 Diagram of light path

A more detailed light path is illustrated in Figure 5-5. The angle θ of diffracted beam in its -1st order is:

$$\theta = \sin^{-1}\left(\lambda f_c\right) \tag{5-3}$$

where f_c is the frequency of the compensator grating and λ is the wavelength of the laser in air.

Other angles in the light path shown in the figure have the following relationships:

$$\zeta = \frac{\pi}{2} - \theta - \gamma \tag{5-4}$$

$$\varphi = \frac{\pi}{2} - \left(\eta + \zeta - \gamma\right) \tag{5-5}$$

$$\sin\varphi = n\sin\varphi' \tag{5-6}$$

$$\alpha = \eta + \varphi' \tag{5-7}$$

$$n\sin\alpha = n'\sin\alpha' \tag{5-8}$$

where

γ – Mirror angle

η – Prism angle

n – Refractive index of BK7

n' – Refractive index of immersion fluid

The frequency of the virtual reference grating, f_m, is determined as:

$$f_m = \frac{2n'\sin\alpha'}{\lambda} \tag{5-9}$$

The governing equation for the f_m can be derived by substituting Eqs (5-3) to (5-8) into Eq (5-9):

$$f_m = \frac{2n}{\lambda}\sin\left\{\eta + \sin^{-1}\left\{\frac{1}{n}\sin\left[\sin^{-1}\left(\lambda f_c\right) + 2\gamma - \eta\right]\right\}\right\} \tag{5-10}$$

Governing equation (5-10) provides a guideline for: (a) adjustment of mirror-tilting angle for different combinations of compensator grating and specimen grating, (b) selection of light source.

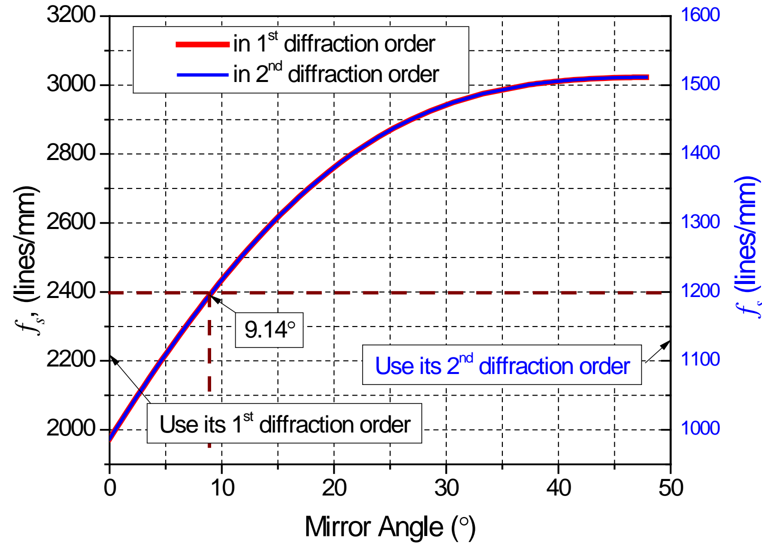

Figure 5-6 Mirror tilting angle vs specimen grating

Since the 1200 lines/mm grating is readily available, it is employed as the compensator grating. A common prism with corner angle of 45° is used in the interferometer. The system can accommodate the specimen grating with different frequencies by adjusting the mirror angle, γ. The relationship between a mirror angle, γ, and a specimen grating frequency, f_s, is shown in Figure 5-6. In the current study, a desired virtual reference grating with f_m = 4800 lines/mm is achieved using a compensator grating with f_c = 1200 lines/mm, λ = 514 nm, $\eta = 45°$, $n = 1.56$ (BK7) and $\gamma = 9.14°$.

5.3.2. Optical and Mechanical Assembly

The optical and mechanical assembly of the enhanced MMI is shown in Figure 5-7. It contains three main parts: an interferometer/laser assembly, a complete translation and rotation stage with respect to three axes, and an imaging system (objective lens, mirror, CCD camera and holders).

The argon ion laser light (514 nm) is directed to a collimator through a fiber mounted at the bottom of the base plate. The compensator grating (f_c = 1200 lines/mm) is attached to the phase shifting device firmly mounted on the base plate. More details about the phase-shifter will be discussed later. A shutter is provided to control collimated beams for U/V fields. The mirror assemblies are mounted on the sidewalls and the titling screws are exposed to the outside. They adjust four beams individually. The interferometer is made of four right angle prisms and a round optical flat. It is fixed at the top plate.

The specimen with a specimen grating is placed on the interferometer, and the gap between the specimen grating and the optical flat is filled with immersion fluid. The xyz translation stage makes the system observe the fringe pattern at any position of the specimen cross section. Two long working distance microscope objective lenses (5X and 10X) are placed inside the MMI. The objective holder has a z-axis adjustment for image focusing. Diffracted beams are redirected to the CCD camera placed outside the MMI by a mirror. All the optical elements are enclosed inside the MMI, which makes the system very stable against environmental disturbances.

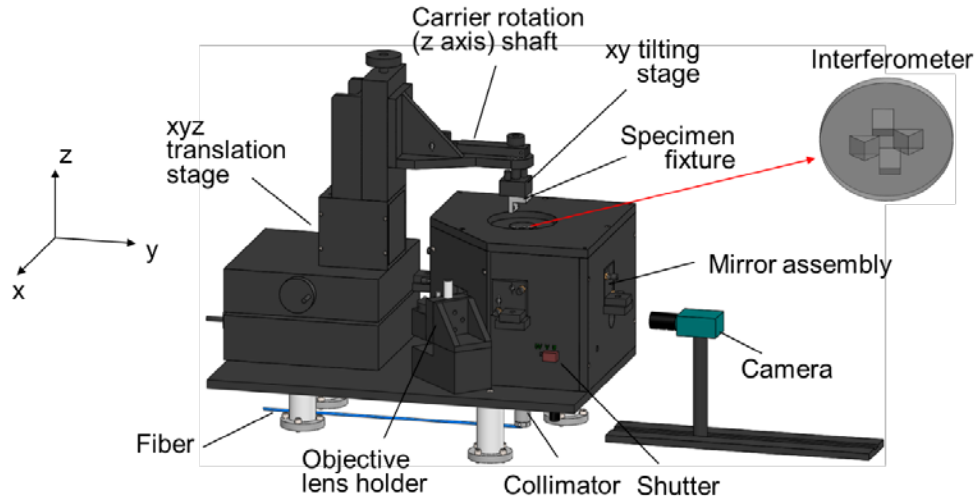

(a)

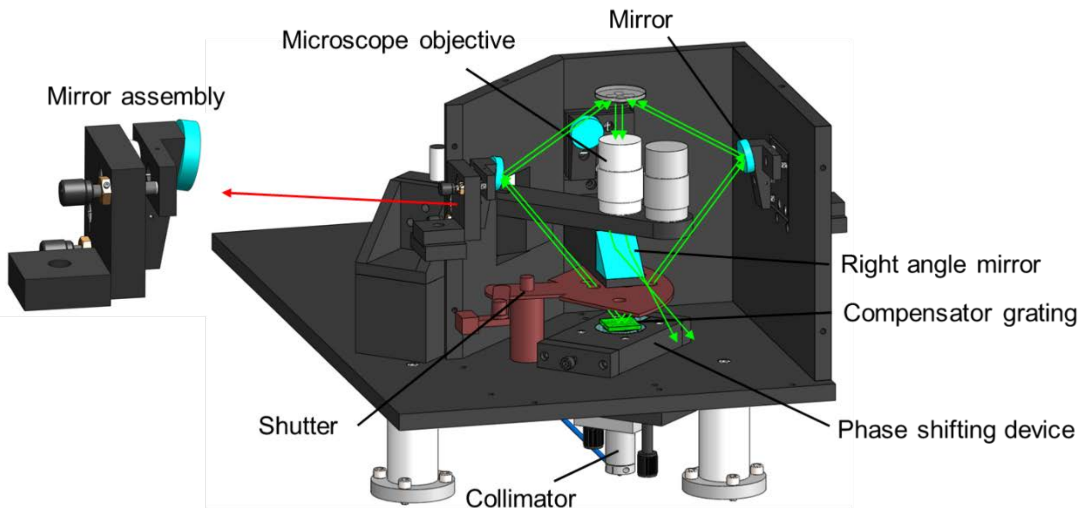

(b)

Figure 5-7 Enhanced MMI assembly: (a) optical and mechanical configurations, (b) components inside MMI and light path

5.3.3. Mechanism of Fringe Phase Shifting Device

A robust phase shifting device is designed for stable, accurate and fast phase shifting. As shown in Figure 5-8, the collimated beam goes through a cylindrical seat and diffracts into +1st, -1st and 0th order from the compensator grating which is directly

mounted on the seat. A PZT actuator is attached to one side of the seat. A high strength spring pushes the seat in an opposite direction to make the transducer preloaded effectively. In such a way, the seat translates immediately corresponding to the voltage applied on the actuator. The seat, PZT actuator and spring are all embedded in the silicone rubber forming a stable elastic foundation. Extremely stable phase shifting is ensured. The compensator grating is oriented at 45° with respect to the translation axis. When the moving distance of the foundation is d, the translation distance of U (or V) field grating lines along x (or y) axis is $d/\sqrt{2}$.

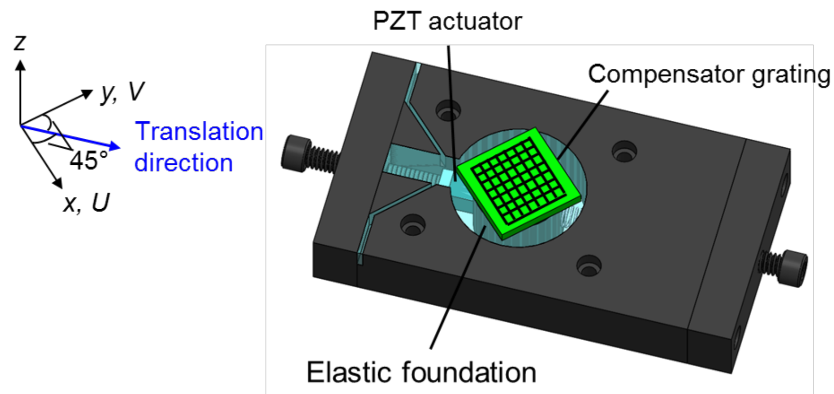

(a)

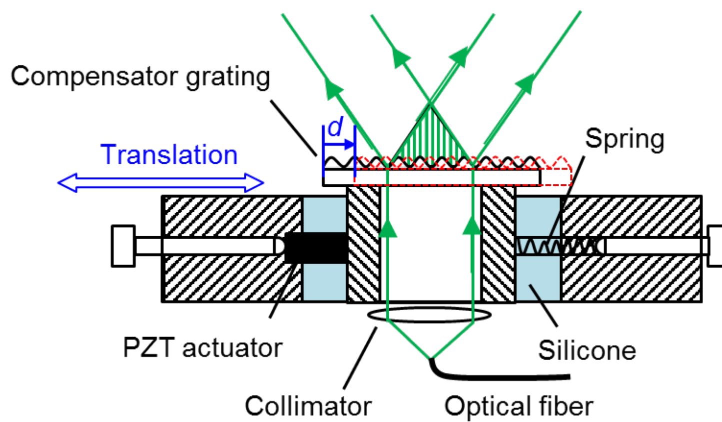

Figure 5-8 Schematics of phase shifting device (a) and its cross section (b)

The phase shifting is accomplished by translating the compensator grating by a fraction of its pitch. A rigorous grating diffraction theory [67] was used to define the phase change of the diffracted beam with respect to the relative position to the compensator grating [68]. This subject is revisited to provide a better physical explanation.

The electronic-magnetic fields after incident light is diffracted by a grating has been rigorously solved by D. Maystre based on Maxwell equation with radiation condition and boundary conditions on the grating profile [67]. It concludes that the only a finite number of the diffracted plane waves remain after diffraction and they propagate in the direction expressed by the well-known grating formula:

$$\sin\beta_m = \sin\alpha + mf_c\lambda \qquad (5\text{-}11)$$

where α is the incident angle, β_m is the diffraction angle in the mth diffraction order.

The complex field of the beams diffracted by a grating is solved [67, 68]:

$$E(x,z) = \sum_m E_m(x,z) = \sum_m B_m\phi_m(x,z) = \sum_m B_m \exp\left[i\frac{2\pi}{\lambda}\left(x\sin\beta_m + z\cos\beta_m\right)\right] \qquad (5\text{-}12)$$

where B_m and ϕ_m represent the amplitude and the phase for each diffracted beam respectively.

The linear relationship between the translation of the compensator grating, Δl, and the phase changes in the $\pm m^{th}$ order diffracted beam, $\Delta\phi$, is obtained [68] (Figure 5-9 (a)):

$$\Delta\phi_{+m} = 2\pi mf_c\Delta l \qquad \text{and} \qquad \Delta\phi_{-m} = -2\pi mf_c\Delta l \qquad (5\text{-}13)$$

Therefore the phase change in the specimen grating with the translation of the compensator grating can be expressed as:

$$\Delta\phi = 4\pi m f_c \Delta l \tag{5-14}$$

A physical explanation of the phase shifting mechanism is given based on the grating formulation and the fact that the wavefront (perpendicular to the collimated light propagation direction) has the same phase ϕ for each beam in the mth order. In Figure 5-9 (b), the solid line shows the new position of the compensator grating after translation by distance Δl (Figure 5-9 (a)).

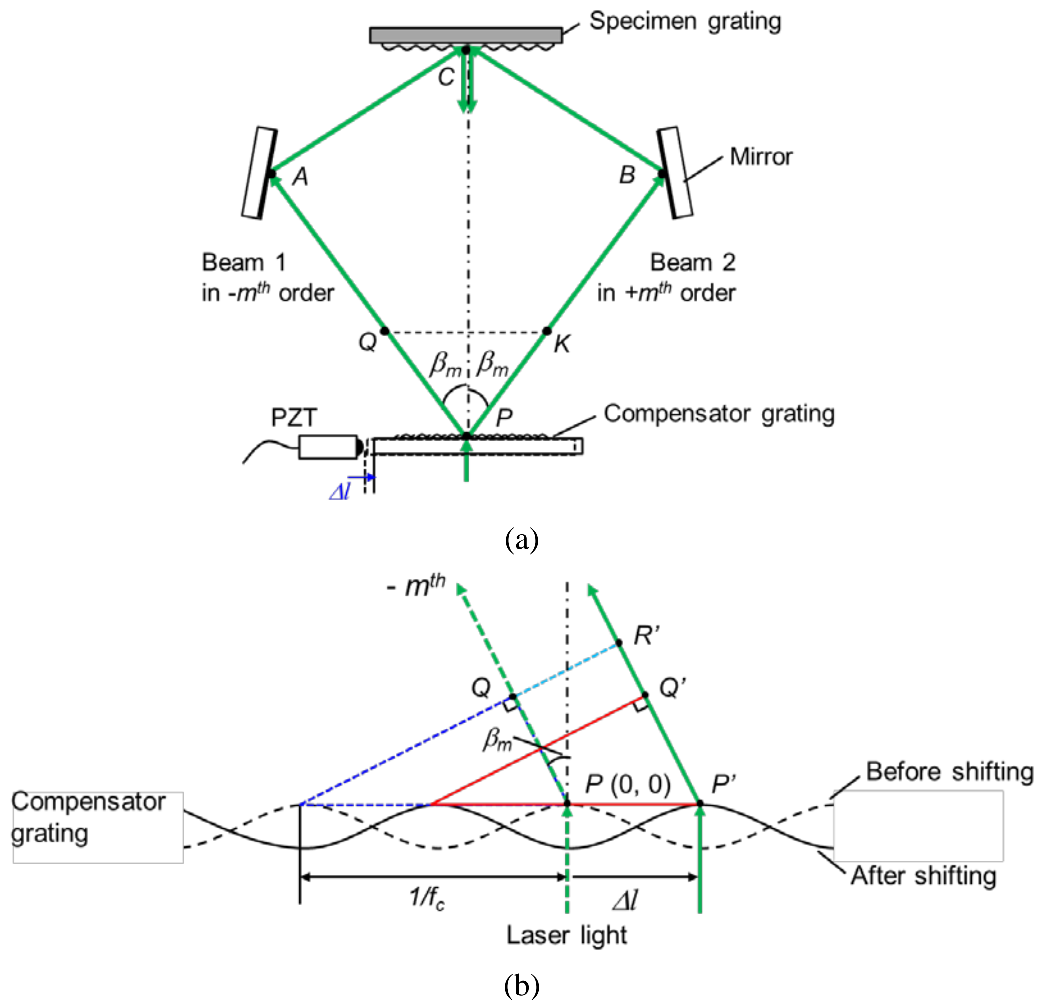

Figure 5-9 Explanation for phase shifting mechanism: (a) Optical path length, (b) phase change for diffracted beam in $-m^{th}$ order

For $\alpha = 0$, the Eq. (5-11) become:

$$\sin\beta_m = mf_c\lambda \tag{5-15}$$

Before shifting, assume the point P (0, 0) at the original position has phase $\phi_P = 0$, then, the phase at point Q is:

$$\phi_Q = \phi_P + 2\pi\frac{PQ}{\lambda} = 0 + 2\pi\frac{(1/f_c)\sin\beta_m}{\lambda} = 2m\pi \tag{5-16}$$

After shifting, P (0, 0) moves to P'(*Δl, 0*). Then, the phase at point P' and Q' remain the same: $\phi_{P'} = \phi_P = 0$, and $\phi_{Q'} = \phi_Q = 2m\pi$. The spatial point R' and Q are at the same wave front, therefore, they have the same phase:

$$\phi_Q = \phi_{R'} = \phi_{Q'} + 2\pi\frac{Q'R'}{\lambda} = 2m\pi + 2\pi\frac{\Delta l\sin\beta_m}{\lambda} = 2m\pi\left(1 + \frac{\Delta l}{1/f_c}\right) \tag{5-17}$$

Thus, the phase change at point Q in the $-m^{th}$ diffraction order after shifting is:

$$\Delta\phi_Q = 2m\pi\frac{\Delta l}{1/f_c} \tag{5-18}$$

In the same way, the phase change at point K in the $+m^{th}$ diffraction order after shifting can be derived and it is:

$$\Delta\phi_K = -2m\pi\frac{\Delta l}{1/f_c} \tag{5-19}$$

Therefore, the relative phase change $\Delta\phi$ between two diffracted beams (in $\pm m^{th}$ orders) corresponding the grating movement distance Δl becomes identical to Eq. (5-15). It means the relative phase change will be 2π when the compensator grating is moved by $1/(2mf_c)$ which is 1/(2m) of the grating pitch. For the enhanced MMI

implementation (f_c = 1200 lines/mm, in ± 1st diffraction order), shifting the compensator grating by one-half pitch (417nm) will cause 2π phase change.

5.4. Bi-thermal Loading Experimental Procedure

Since the immersion fluid is used in the MMI, real-time measurements of thermal mechanical deformations are not practical. An experimental procedure known as "bi-thermal loading" is implemented; namely, the deformation state is locked at room temperature for measurements without a thermal chamber.

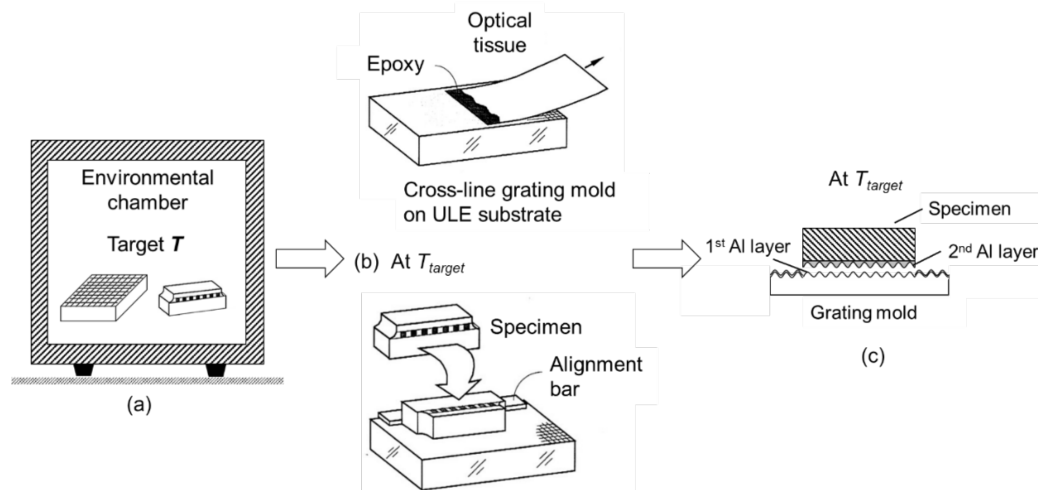

Figure 5-10 Specimen replication for bi-thermal loading experiment

A typical bi-thermal loading procedure is shown in Figure 5-10: (a) the grating mold and specimen are heated to a target temperature; (b) a high temperature curing epoxy is used to replicate the grating on the specimen cross section; and (c) after curing, the specimen grating is pried off from the glass mold. The grating mold on a ULE glass substrate is used to ensure the same specimen grating frequency at elevated temperature. The specimen grating is not deformed at target temperature and has the same frequency as the ULE grating. Then, the specimen is cooled down to room temperature and the specimen grating deforms with the specimen. The ULE grating is used to tune the

moiré system first. Then, the displacement field of deformed specimen grating is recorded at room temperature.

For the displacement measurement over a small field of view, the displacement can be very small. It is very critical to ensure that a good null field is obtained at the specimen grating after separation as the initial reference. In addition, the thickness of the epoxy layer between specimen cross section and specimen grating should be sufficiently small compared to the microstructures of interest, in order to reduce the "shear lag" effect in the regions of large strain gradients such as at geometric and material discontinuities [41]. It is difficult to achieve the two conditions when a specimen grating is replicated inside an environmental chamber. A new procedure is developed to cope with the problem. The procedure is shown in Figure 5-11:

(1) Step 1: Replication of a specimen grating at room temperature. A tiny amount of epoxy is applied around the region of interest on specimen cross section with a sharp-pointed tool. Then, specimen is pressed against a regular grating mold with double coated Al layers to spread the epoxy into a thin film over the region. After epoxy is cured at room temperature, the specimen with grating is pried off from the mold. The null field is checked with the PEMI system. After the good null field is obtained, a small amount of photo-flo solution is applied on the specimen grating surface as a separation medium. After the solution dries, a thin Al layer is deposited.

(2) Step 2: Replication of the deformed specimen grating at an elevated temperature. Place a ULE substrate and the specimen prepared in previous step inside an environment chamber to reach a target temperature. The specimen grating

deforms at the elevated temperature. Then, put a small amount of a high temperature curing epoxy on the deformed specimen grating and place it on the ULE substation. After epoxy is cured, the newly deposited Al grating is separated from specimen.

(3) Step 3: Measurement of the deformed grating on ULE substrate. The grating mold used in Step 1 is used to tune the system. Then, the grating mold is replaced with the ULE substrate and deformations are measured by the MMI system.

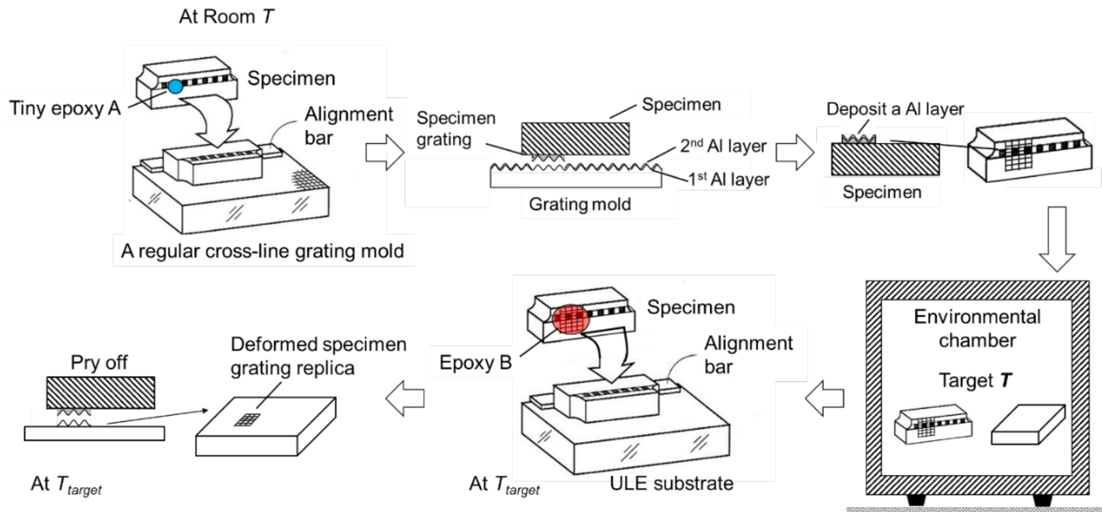

Figure 5-11 New specimen grating replication procedure

5.5. Discussion

The achromatic moiré concept is used in the advanced MMI system. Although the system is not a true achromatic system [41], it still offers the more flexibility for light source selection compared to the MMI system shown in Figure 5-1. For a light source with broad spectrum, the frequencies of different virtual gratings generated on the same specimen grating surface by the specific wavelengths can be calculated using the governing Eq. (5-10). The intensity distribution as function of fringe order is illustrated in Figure 5-12, where light sources with center wavelength λ_0 = 514 nm are

considered and the f_m is 4800 lines/mm. Even for the laser diode with relative large spectrum width, the number of fringes up to around 21 still can be well visualized.

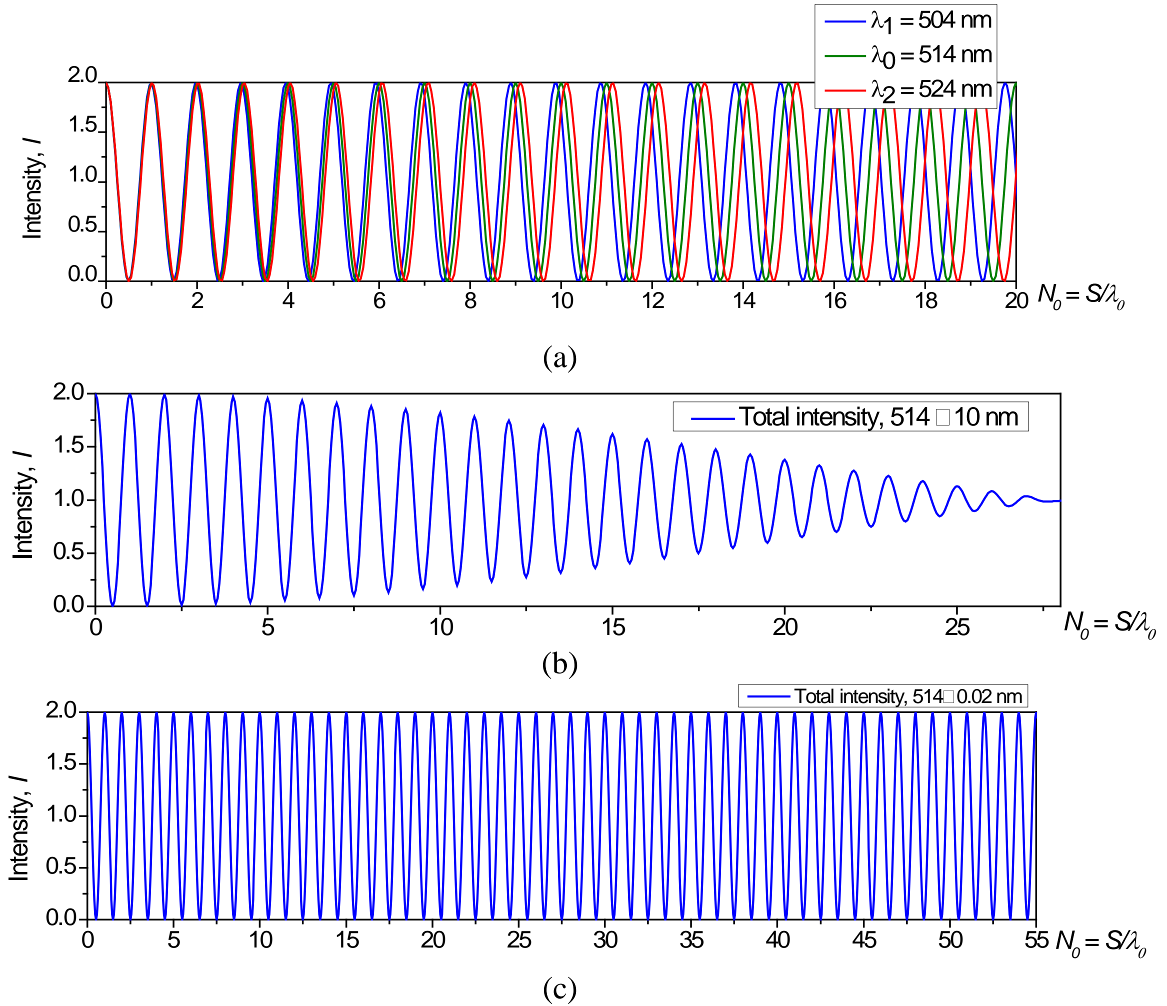

Figure 5-12 Intensity distribution for interference with different light sources: (a) light source with a single wavelength: λ_0 = 514 nm, λ_1 = 504 nm, λ_2 = 524 nm; (b) laser diode: λ = 514 ± 10 nm; (c) ion laser: λ = 514 ± 0.02 nm

5.6. Application: Experimental Analysis of Redistribution Layer (RDL) Deformation in FO-WLP

In Chapter 2, the global deformations and local solder ball deformations of a FO-WLP PoP package were investigated. In this section, the study focused on the thermo-mechanical deformation of the RDL layer using the enhanced MMI system.

5.6.1. Experiment and Results

The PoP package with underfill was analyzed. The previous study shows that the largest shear strain of solder balls under FO-WLP package is located at the die edge area Figure 2-18. The RDL deformation at the die edge area was analyzed. The specimen was cut and ground to expose the desired microstructure as illustrated in Figure 5-13, where the detailed microstructures of interest at the RDL layer are depicted in (b). The interface between RDL layer and Chip, EMC, underfill are also marked by red dash line in (b).

The procedure described in Figure 5-11 was used to replicate the grating. A room temperature curing epoxy (Henkel: F114) was used to replicate the specimen grating on a small area marked in Figure 5-13 (a) at room temperature (22 °C). A high temperature curing epoxy (Henkel: F230) was used to replicate the deformed specimen grating at 100 °C. The fringes were recorded at room temperature (22 °C), representing the thermal deformation of ΔT= +78 °C.

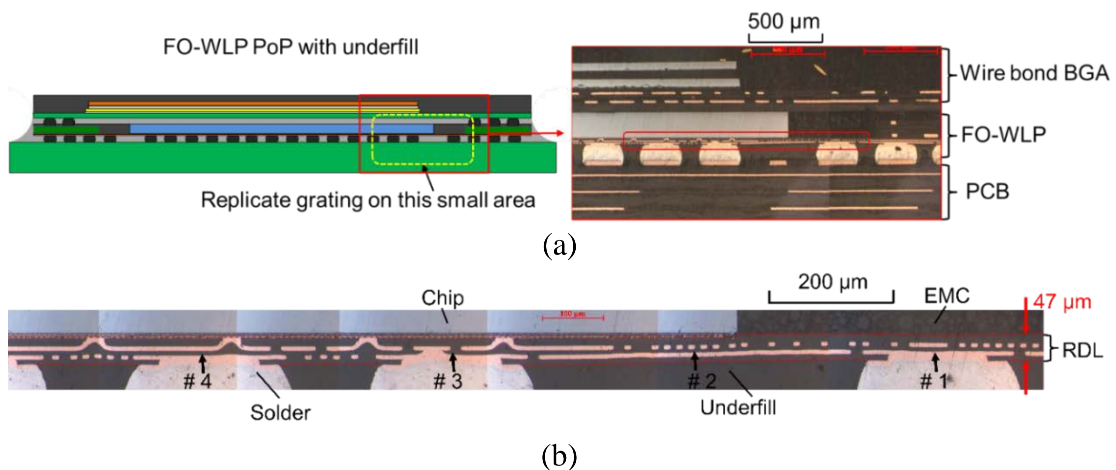

Figure 5-13 RDL structure in FO-WLP PoP specimen: (a) PoP Specimen cross section and area of interest, and (b) RDL microstructure

The resultant fringe patterns for the four sections (#1, #2, #3 and #4) of RDL marked in Figure 5-13 (b) are shown in Figure 5-14. The corresponding cross section are overlapped on the fringe patterns to identify the exact location of RDL. A fringe multiplication (O/DFM) factor of $\beta = 8$ was used to produce a displacement contour interval of 26 nm/fringe.

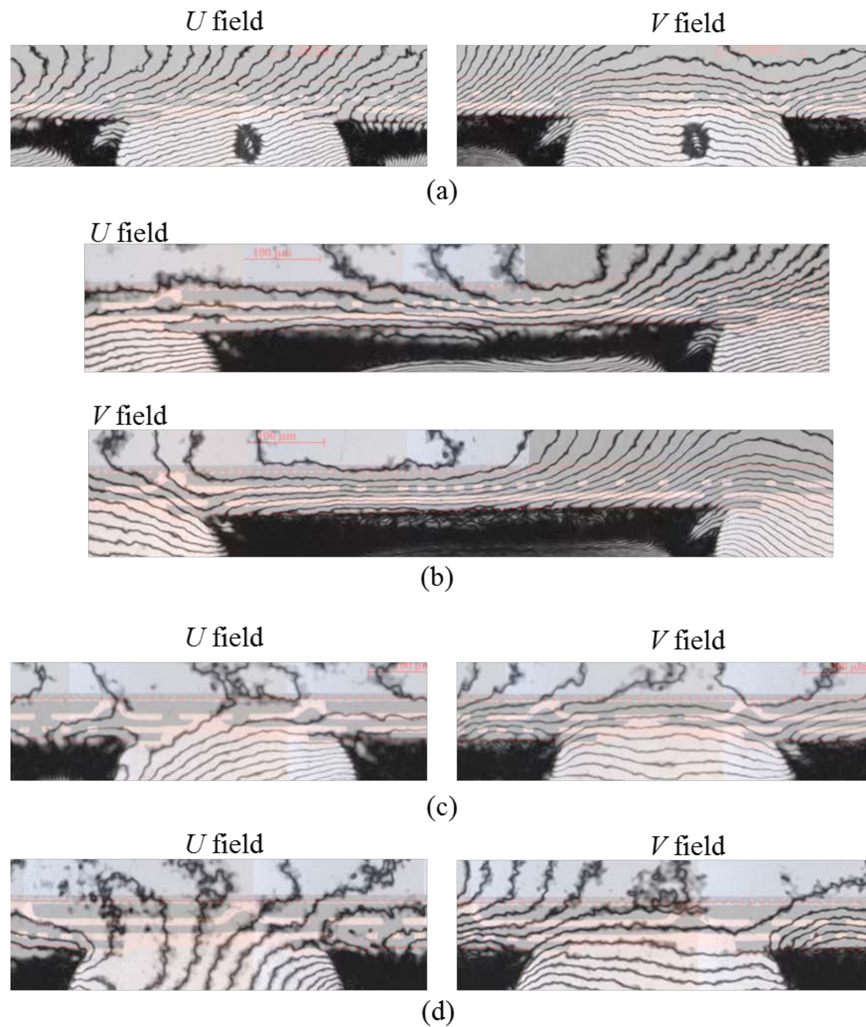

Figure 5-14 Fringe patterns for RDL layer with contour interval 26 nm/fringe: (a) #1, (b) #2, (c) #3, and (d) #4

The deformed configuration of RDL can be determined from the U and V displacement fields and it is plotted in Figure 5-15. It was greatly exaggerated to

highlight the important deformation modes where the deformation was magnified X100. At the die edge area, there are two deflection locations due to the material discontinuity. One locates at the interface between chip and EMC material, and the other one locates at the left-up side of solder ball under EMC. Under die area, the RDL bends upward due to the strong constrain from the die.

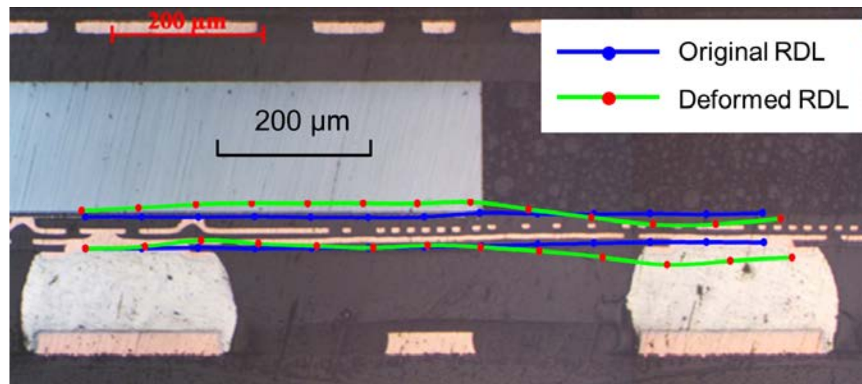

(a)

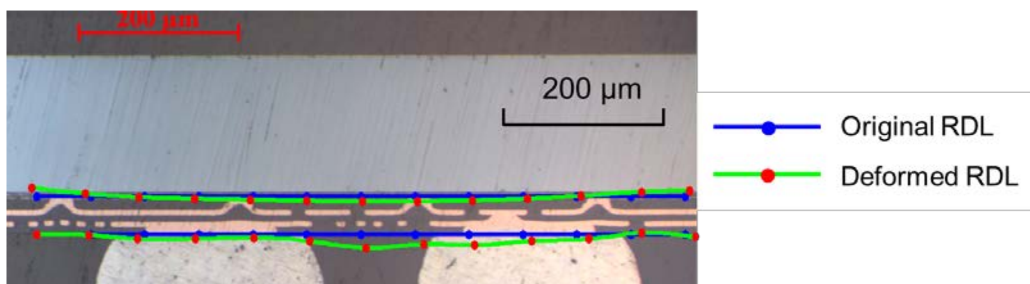

(b)

Figure 5-15 Deformed configuration of RDL layer (RDL deformation magnified X100): (a) at die and EMC material interface area, and (b) at site #3 and #4

The RDL at site #1 shows the largest deformation among the four sites. The maximum shear strain locates at the left-up side of solder ball at site #1 and it is about 0.48%. It is to be noted that the solder ball at this location has the largest average shear

strain as shown in chapter 2. It is expected that it would be one of the most critical failure sites in this package.

5.7. Conclusion

An advanced immersion based microscopic moiré interferometer (MMI) was developed to overcome the limitations of the current MMI system. Detailed optical configuration and mechanical assemblies were described. A robust phase shifting device was created in the system to provide stable phase shifting. A new bi-thermal loading experimental procedure was developed. The advanced MMI system was successfully employed to investigate the micromechanical deformations in the redistribution layer (RDL) of a fan-out wafer level package. The system can be further utilized to analyze the deformation behavior of other microstructures in the advanced electronic packaging components and subassemblies.

Chapter 6 Fabrication of High Quality Grating and Improvement of O/DFM Algorithms for High Displacement Resolution

6.1. Introduction

The advanced immersion based MMI system provides higher displacement resolution (basic sensitivity is 4.8 fringes per micrometer displacement, i.e., contour interval 208 nm/fringe). However, it is still not high enough for the micromechanical deformation analyses. Post-processing of fringe pattern images is required to further enhance the displacement resolution. Moiré interferometry is a phase-based technique. An ideal fringe pattern and its sinusoidal intensity distribution are shown in Figure 6-1 (a). In the actual experiment, the fringe pattern contains inherent optical noise caused by the diffraction grating and the input beams, as illustrated in Figure 6-1 (b). The noise poses challenges for the post-processing techniques such as the O/DFM method and the phase shifting technique [63, 69-74]. In order to obtain more accurate displacement results, a specimen grating with much high quality was developed and the O/DFM algorithms were improved to achieve the desired displacement resolution.

6.2. Fabrication of High Quality Specimen Grating

The fringe patterns of excellent clarity are achieved when specimen gratings are replicated from high quality molds [41]. Currently, a disposable grating mold is fabricated from a sub-master silicone rubber grating. The sub-master grating is a replica of a photoresists master grating fabricated from a typical lithography process using two-beam interference. Although, in principle the sub-master grating fabrication is not supposed to degrade the master grating, the master grating is degraded while the

sub-master grating is fabricated. A more robust master grating is needed to avoid the noise from the grating.

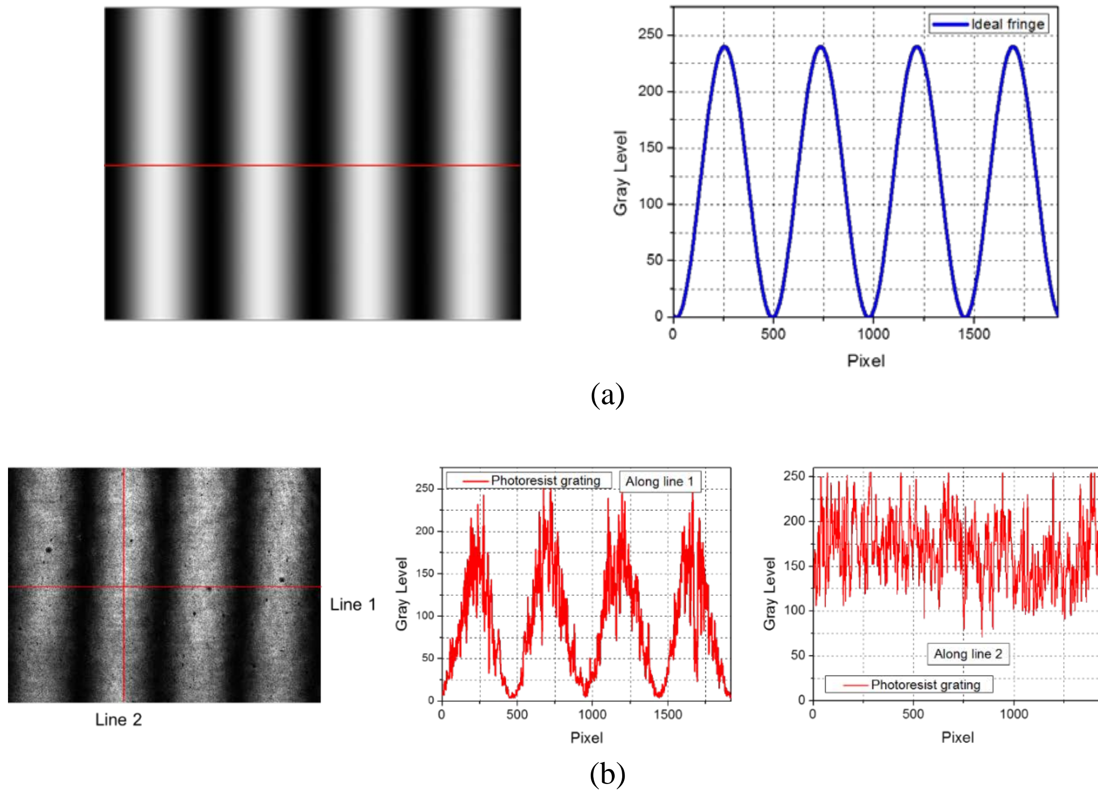

Figure 6-1 Comparison of fringe patterns: (a) an ideal fringe pattern and gray level distribution, (b) fringe pattern from photoresist grating and gray level distribution

Rigid grating molds were fabricated on a silicon substrate to provide the required robustness. A grating with 2500 lines per mm (a pitch of 400 nm) fabricated by a semiconductor fabrication process is shown in Figure 6-2. It was tested using the enhance MMI system. The results are shown in Figure 6-3. The quality of the fringe pattern is much better compared to the photoresist grating (1200 lines/mm) shown in Figure 6-1 (b).

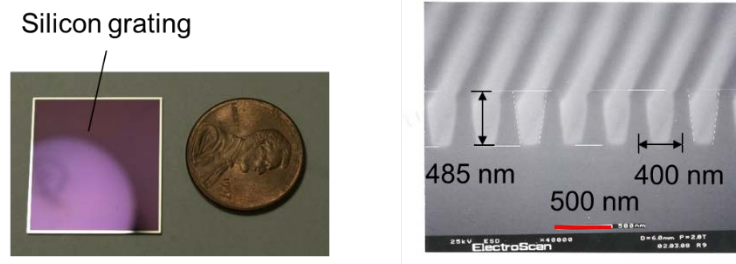

Figure 6-2 Silicon grating and SEM image

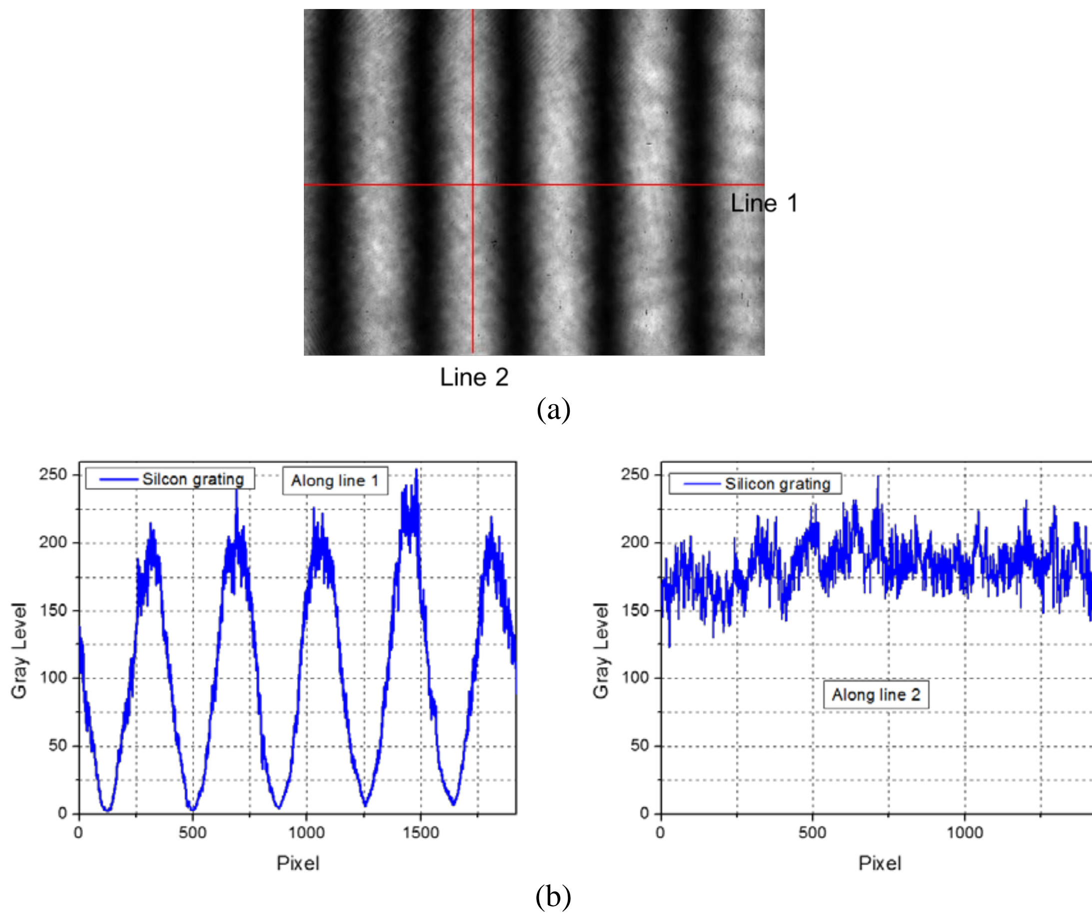

Figure 6-3 Silicon grating: (a) fringe pattern and (b) gray level distribution

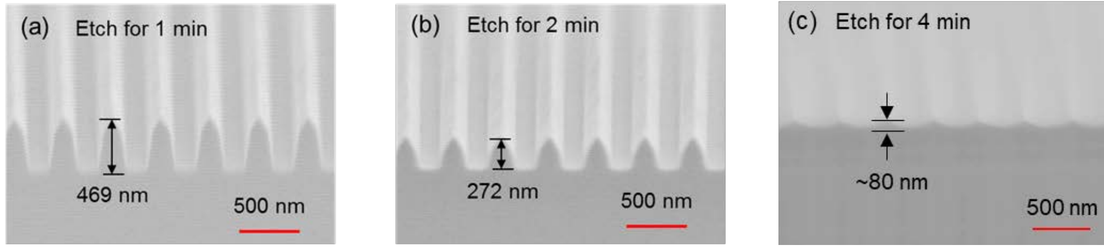

Figure 6-4 Silicon SEM images after etching for: (a) 1 min, (b) 2 min and (c) 4 min

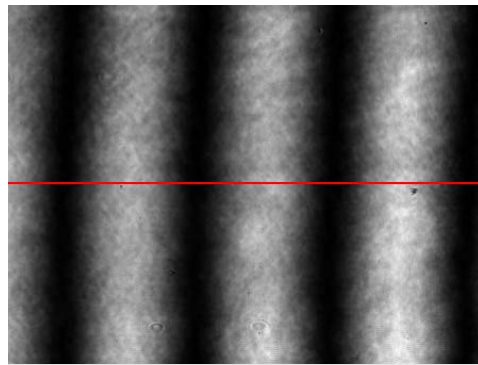

(a)

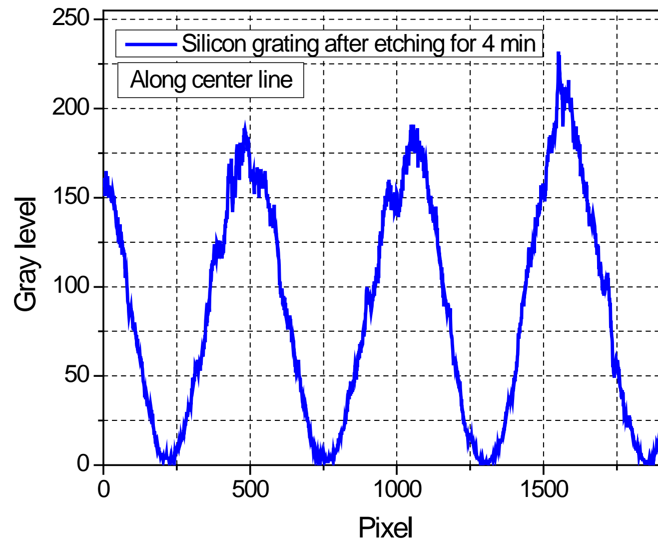

(b)

Figure 6-5 Silicon grating after etching for 4 min: (a) fringe pattern (b) gray level distribution

It is to be noted that the semiconductor fabrication process produced deep and square shape gratings (Figure 6-2). In spite of high quality, the gratings are not suitable for replication. In order to reduce the aspect ratio for ease of replication, the silicon was etched by the reactive ion etching process (Oxford ICP Etcher). Figure 6-4 shows the grating profiles after etching. The grating height is about 80 nm after etching for 4 min. The aspect ratio of height to pitch is 1:5 and it is low enough for grating replication. The etched grating was tested in MMI system. The fringe pattern and gray level distribution are shown in Figure 6-5. The good fringe quality is maintained after etching.

The typical bi-thermal loading experimental procedure, shown in Figure 5-10, was employed to utilize this etched silicon grating. Compared to the current disposable grating mold which is made by epoxy on a glass substrate, the rigid silicon grating mold is much more robust and the specimen grating replication can be replicated inside the environmental chamber. Different from the specimen grating molds mentioned in previous sections which contain two layers of aluminum layers, only one thin aluminum layer is deposited on the etched silicon grating surface. During the replication process, the Al layer gratings is ready to be separated from Si grating mold after the high temperature curing epoxy is cured. Because there is very weak adhesion between Al layer and silicon grating surface. In such a way, the specimen grating (Al layer) maintains the high quality grating profile of Si grating mold. There is a disadvantage of the silicon grating for the deformation measurement application. It is a linear-line grating and not cross-line grating. It is only able to provide one field fringe pattern. Correct system tuning procedure is the key for its successful application in

MMI system. The system tuning procedure will be introduced in the following application section.

6.3. Improved O/DFM Algorithms

The optical/digital fringe multiplication (O/DFM) method was developed to provide contour maps with β times as many contours as the original interference pattern. The detailed algorithms can be found in Ref. [44]. One of its main advantages is that it utilizes data sites of optimum reliability and it is very effective to process fringe patterns which contain optical noise. The truncation and binarization steps were used in the algorithms and it results in a binarized fringe pattern. These steps were repeated for other pairs of complementary fringe patterns to obtain fringe pattern with higher multiplication factor β (>2). The O/DFM algorithms were improved to achieve higher β without this repeated truncation and binarization steps while maintain the main advantages.

The intensity distribution of a general interferogram (fringe pattern) can be expressed as a periodic function by the summation of a Fourier cosine series:

$$I(x,y) = I_a(x,y) + \sum_{n=1}^{\infty} C_n(x,y)\cos\left[n\phi(x,y)\right] \quad n = 1,\ 2,\ 3,..., \tag{6-1}$$

where I is the intensity distribution of the fringe pattern, I_a is the mean intensity, C_n is the coefficients of the harmonic series, (x, y) represents the coordination of a point on the fringe pattern, ϕ is the angular phase information of the fringe pattern which can be express as a function of the fringe order N at each point:

$$\phi\ (x,y) = 2\pi N(x,y) \tag{6-2}$$

A series of β shifted fringe patterns can be recorded with sequential changes of phase by a constant increment of $2\pi/\beta$, where β is called the fringe multiplication factor and it is an even number. In this advanced O/DFM method, $\beta = 2^{m}$ is considered, where m is a positive integer.

The phase shifted fringe patterns can be divided into two groups: the patterns of the first half and their complements. The intensity distribution of these patterns can be expressed as

$$\begin{aligned} I_i(x,y) &= I_a(x,y) + \sum_{n=1}^{\infty} C_n(x,y)\cos\left\{n\left[\phi(x,y) + 2i\pi/\beta\right]\right\} \\ I_i^{\pi}(x,y) &= I_a(x,y) + \sum_{n=1}^{\infty} C_n(x,y)\cos\left\{n\left[\phi(x,y) + \left(i+\frac{\beta}{2}\right)2\pi/\beta\right]\right\} \\ &= I_a(x,y) + \sum_{n=1}^{\infty} (-1)^n C_n(x,y)\cos\left\{n\left[\phi(x,y) + 2i\pi/\beta\right]\right\} \\ i &= 0,\ 1,\ 2,\ldots,\frac{\beta}{2}-1 \end{aligned} \qquad (6\text{-}3)$$

where I_i is the intensity distribution of the ith-shifted pattern, which is shifted by $2i\pi/\beta$ with respect to the original pattern. The term I_i^{π} is the intensity distribution of the corresponding complementary pattern, which is shifted by π with respect to the ith -shifted pattern.

6.3.1. O/DFM with $\beta = 2$

Two phase-shifted images are required. The intensity distribution I_{ri} is obtained by subtracting the complementary pair of fringe patterns and can be express as

$$\begin{aligned} I_{ri}(x,y) &= I_i(x,y) - I_i^{\pi}(x,y) I_a(x,y) \\ &= 2\sum_{n=1}^{\infty} C_{2n-1}(x,y)\cos\left\{(2n-1)\left[\phi(x,y) + 2i\pi/\beta\right]\right\} \end{aligned} \qquad (6\text{-}4)$$

For the location of $I_{ri} = 0$, the phase $\phi(x, y)$ is:

$$\phi(x, y) = \pi\left(\frac{2j+1}{2} - \frac{2i}{\beta}\right) \qquad j = 0,\ \pm 1,\ \pm 2,\ ... \tag{6-5}$$

Then, the fringe orders at $I_{ri}(x, y) = 0$ are

$$N(x, y) = \frac{2j+1}{4} - \frac{i}{\beta} = 0.5k \qquad k = 0,\ \pm 1,\ \pm 2,\ \pm 3,\ ... \tag{6-6}$$

The fringe pattern after applying O/DFM with $\beta = 2$ is defined as:

$$I_{O/DFM2} = \left|I_{ri}(x, y)\right| \tag{6-7}$$

from which the location of the fringe order $N(x, y) = \frac{1}{2}k$ can be accurately determined, i.e., the (x, y) points where $I_{ri}(x, y) = 0$.

6.3.2. O/DFM with $\beta = 2^m$

For $\beta = 2^m$ with positive integer m >1, the fringe pattern after applying O/DFM with factor β is derived based on:

$$\cos 2\theta = \cos^2\theta - \sin^2\theta \tag{6-8}$$

For O/DFM with $\beta = 4$, four phase-shifted (2π/β) images (I_0, I_1, I_2, and I_3) are required. By subtracting two pairs of complementary fringe patterns (i.e., I_0 and I_2, I_1 and I_3), it can be obtained that

$$\begin{cases} I_{r0} = 2\sum_{n=1}^{\infty} C_{2n-1}(x, y)\cos\left\{(2n-1)\left[\phi(x, y) + \pi/2\right]\right\} \\ I_{r1} = 2\sum_{n=1}^{\infty} C_{2n-1}(x, y)\cos\left\{(2n-1)\left[\phi(x, y) + \pi\right]\right\} \\ \quad = -2\sum_{n=1}^{\infty} C_{2n-1}(x, y)\sin\left\{(2n-1)\left[\phi(x, y) + \pi/2\right]\right\} \end{cases} \tag{6-9}$$

Then,

$$I_{r0}{}^2 - I_{r1}{}^2 = 4\sum_{n=1}^{\infty} C_{2n-1}(x,y)^2 \cos\{2(2n-1)[\phi(x,y)+\pi/2]\} \quad (6\text{-}10)$$

The fringe pattern after O/DFM with $\beta = 4$ is defined as:

$$I_{O/DFM\,4} = \left(\left|I_{r0}{}^2 - I_{r1}{}^2\right|\right)^{\frac{1}{2}} \quad (6\text{-}11)$$

From (6-11) the location of the fringe order $N(x,y) = \frac{1}{4}k$ can be accurately determined, i.e., the (x, y) points where $I_{O/DFM\,4}(x,y) = 0$.

For O/DFM with $\beta = 8$, eight phase-shifted ($2\pi/\beta$) images (I_0, I_1, I_2, I_3, …, I_8) are required.

$$\begin{cases} I_{r0}{}^2 - I_{r2}{}^2 = 4\sum_{n=1}^{\infty} C_{2n-1}(x,y)^2 \cos\{2(2n-1)[\phi(x,y)+\pi/2]\} \\ I_{r1}{}^2 - I_{r3}{}^2 = 4\sum_{n=1}^{\infty} C_{2n-1}(x,y)^2 \cos\{2(2n-1)[\phi(x,y)+\pi/2+\pi/4]\} \\ \qquad = -4\sum_{n=1}^{\infty} C_{2n-1}(x,y)^2 \sin\{2(2n-1)[\phi(x,y)+\pi/2]\} \end{cases} \quad (6\text{-}12)$$

Then,

$$\begin{aligned} &\left(I_{r0}{}^2 - I_{r2}{}^2\right)^2 - \left(I_{r1}{}^2 - I_{r3}{}^2\right)^2 \\ &= 16\sum_{n=1}^{\infty} C_{2n-1}(x,y)^4 \cos\{4(2n-1)[\phi(x,y)+\pi/2]\} \end{aligned} \quad (6\text{-}13)$$

The fringe pattern after O/DFM with $\beta = 8$ is defined as:

$$I_{O/DFM\,8} = \left(\left|\left(I_{r0}{}^2 - I_{r2}{}^2\right)^2 - \left(I_{r1}{}^2 - I_{r3}{}^2\right)^2\right|\right)^{\frac{1}{4}} \quad (6\text{-}14)$$

From (6-14) the location of the fringe order $N(x,y) = \frac{1}{8}k$ can be accurately determined, i.e., the (x, y) points where $I_{O/DFM\,8}(x,y) = 0$.

Using the same method, $I_{O/DFM\ \beta}$ can be obtained for β = 2^m, where m>3. A general form of fringe pattern after O/DFM with $\beta = 2^m$ (m >1) can be derived:

$$I_{O/DFM\,\beta} = \left(\left| \sum_{n=1}^{\infty} C_{2n-1}\left(x, y\right)^{\frac{\beta}{2}} \cos\left\{ \frac{\beta}{2}(2n-1)\left[\phi(x, y)+\pi/2\right] \right\} \right| \right)^{\frac{2}{\beta}} \qquad (6\text{-}15)$$

From (6-15) the location of the fringe order $N(x, y) = \frac{1}{\beta}k$ can be accurately determined, i.e., the (x, y) points where $I_{O/DFM\,\beta}(x, y) = 0$.

The algorithms were applied to the 16 phase-shifted fringe patterns considering three different optical noise levels. The results are shown in Figure 6-6. The improved O/DFM algorithms can well define the boundary of the fraction fringe while maintain the optical noise level (Figure 6-6b). However, the fringe won't be resolved with higher multiplication factor if the optical noise in the original fringe pattern is very large (Figure 6-6c). Therefore, it is critical to have the specimen grating to form the fringe patterns with less optical noise in order to achieve higher deformation resolution.

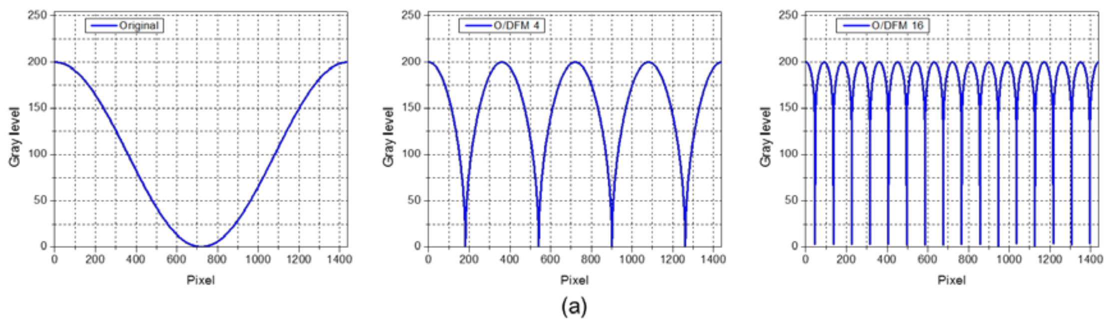

(a)

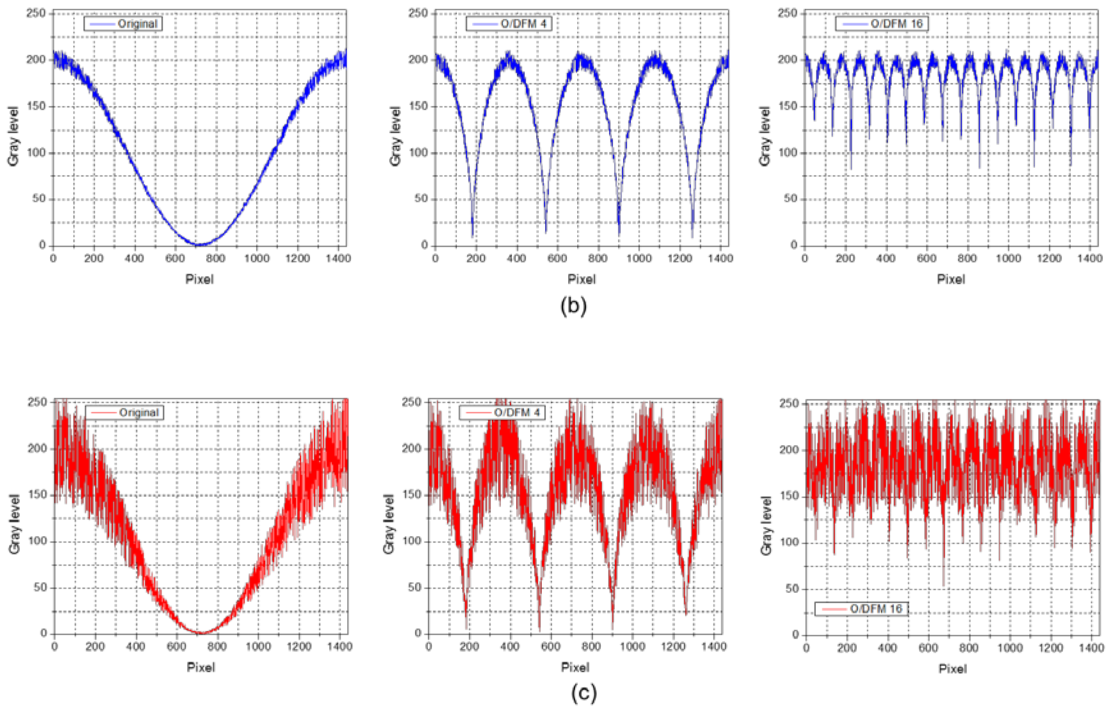

Figure 6-6 Intensity distributions after O/DFM processing for fringe patterns with different optical noise levels: (a) zero noise, (b) low, and (c) high

6.4. Application: Thermo-mechanical Deformation of Solder Bumps in a Server Processor

Thermo-mechanical deformation behavior of a server processor was studied using both advanced moiré interferometer and MMI systems. It is a flip chip package, shown in Figure 6-7. It mainly consists of a large die (31 mm $\times$ 25 mm $\times$ 0.8mm) mounted on a ceramic substrate with dimensions of 62.5 mm $\times$ 62.5 mm $\times$ 3mm through thousands of SnAg solder bumps. The cross section of the corner solder bump is shown in Figure 6-7 (b) and it is height is about 50 μm. For this large flip chip package, the solder bump at the corner would experience large shear deformation under the thermal loading condition. The advanced moiré system was employed to measurement global and local deformations of the package. The results were used to guide the

implementation of Si grating to measure the shear deformation of the corner solder bump in MMI system.

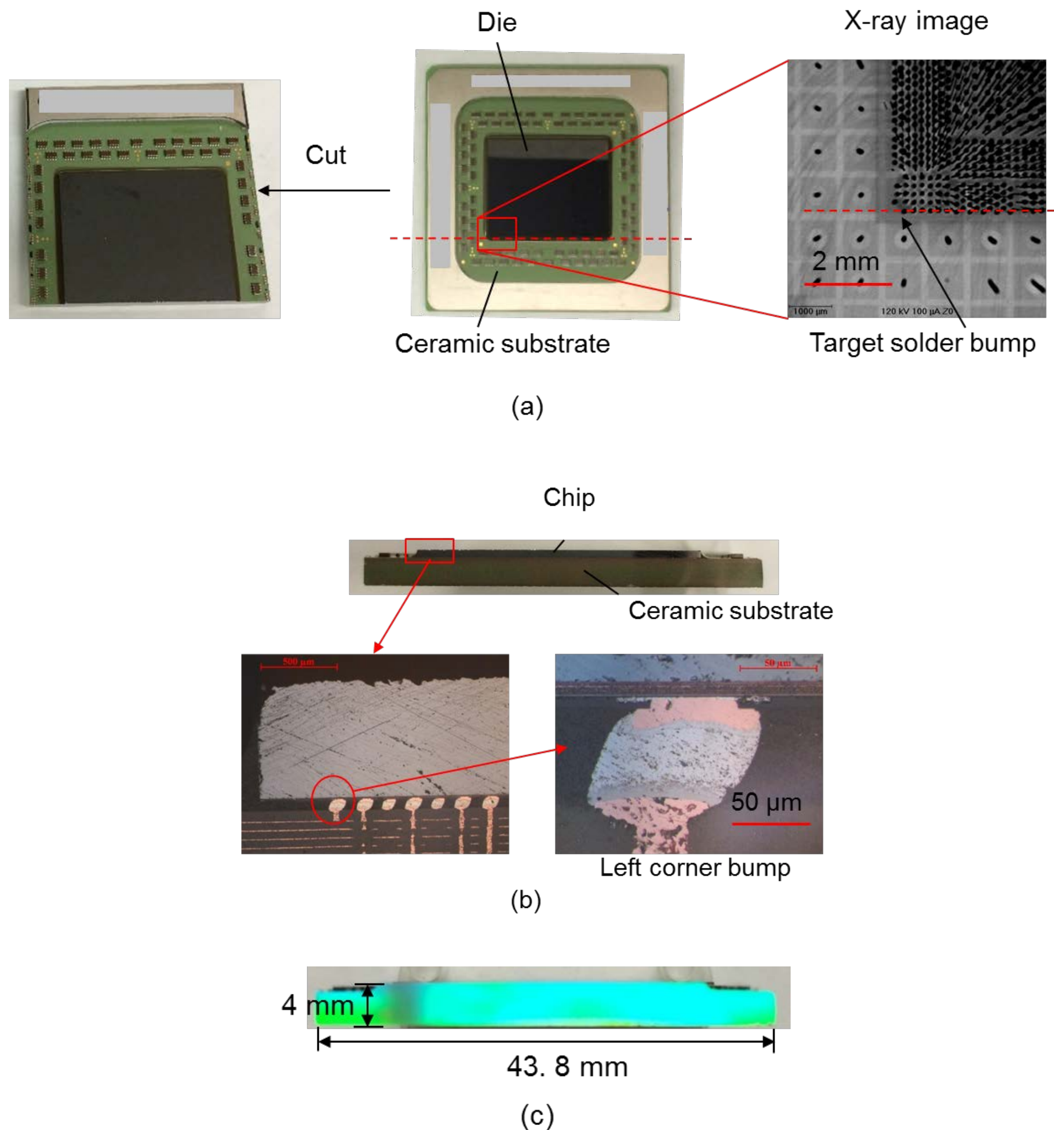

Figure 6-7 Structure of a server processor: (a) package before and after cutting, (b) cross sections and target corner bump, and (c) specimen grating on the cross section

The first experiment was conducted in the advanced moiré system, where the basic fringe contour interval is 417 nm/fringe. Specimen grating (f_s=1200 lines/mm) was replicated on the specimen cross section at room temperature 20 °C. The specimen

was placed in the conduction chamber. Fringe patterns were documented at 100 °C, representing the relative deformations cause by ΔT = +80 °C. The global deformation were shown in Figure 6-8, captured by the zoom lens. The local solder bump deformation were captured by microscope objective, shown in Figure 6-9. The corner solder bump location was marked on the fringe patterns. The O/DFM method proposed in previous section was used to process the fringe patterns to resolve the deformation at the small solder bump. The fringe pattern over the corner solder bump area is horizontal in the *V* field which means the shear component in *V* field is zero and shear strain can be calculated only from the *U* field fringe pattern. The *U* field fringe pattern was used to guide the system tuning in the MMI system when the Si grating was used.

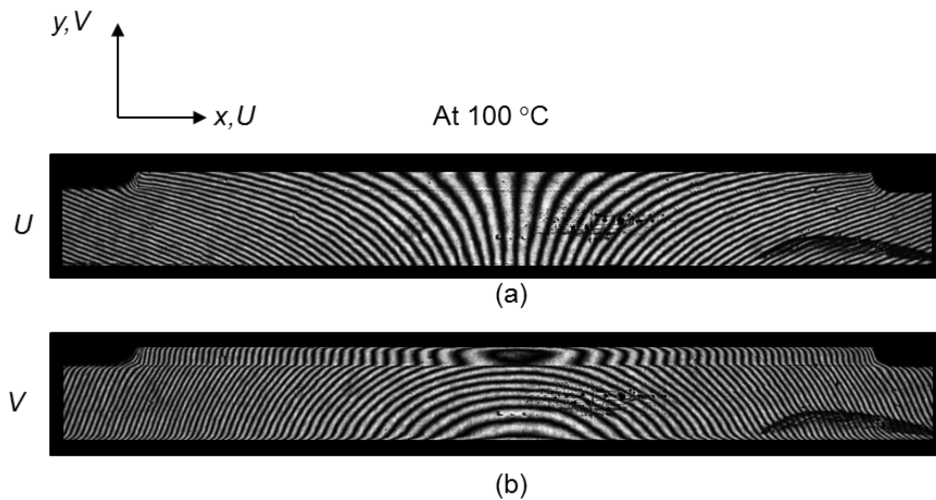

Figure 6-8 Global fringe patterns captured at 100 °C: (a) *U* field and (b) *V* field (contour interval: 417 nm/fringe)

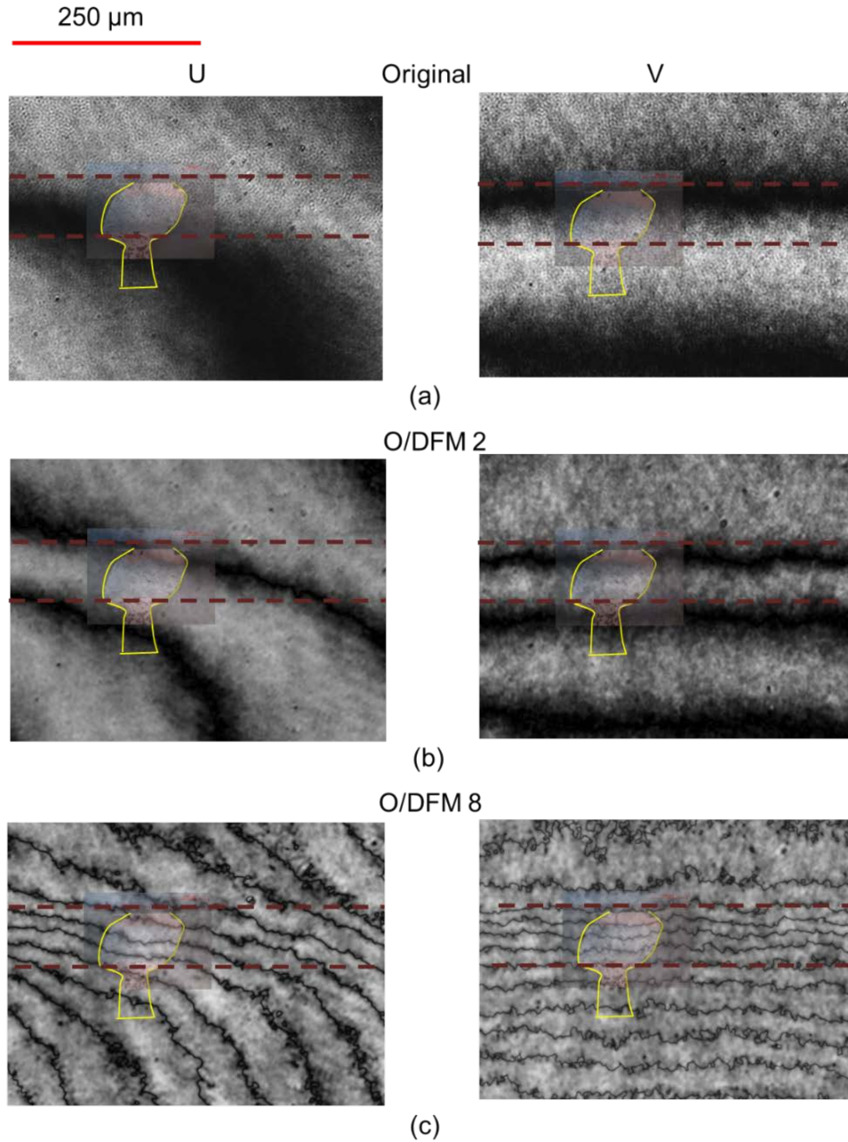

Figure 6-9 Fringe patterns at corner solder bump area: (a) original (417 nm/fringe), (b) O/DFM 2 (208 nm/fringe), (c) O/DFM 8 (52 nm/fringe)

The same specimen was tested in the MMI system using the Si grating (basic contour interval is 200 nm/fringe) with bi-thermal loading ΔT = -80 °C. The linear-line specimen gratings were replicated on an ULE glass substrate and also on a small area round the corner solder bump at 100 °C using the procedures described in Figure 5-10. The Si grating was adjusted that the grating line direction was perpendicular to the ceramic substrate during the grating replication. It was used to capture the *U* field

fringe pattern in the MMI system. After specimen grating replication, the measurement was conducted at room temperature 20 °C. The grating on the ULE glass was used to tune the MMI system first. Then, the specimen with the deformed specimen grating was placed on the MMI system. Any rigidly body rotation can alter the fringe pattern in the moiré system and introduce error in the measurement of shear deformation while only one filed of fringe pattern is available. In this experiment, rigid body rotation was applied to the specimen in such a way that the fringe pattern obtained in MMI system was similar to the *U* fringe pattern (with O/DFM 2) shown in Figure 6-9 (b). It means the shear strain can be calculated from the obtained *U* field fringe pattern in MMI system.

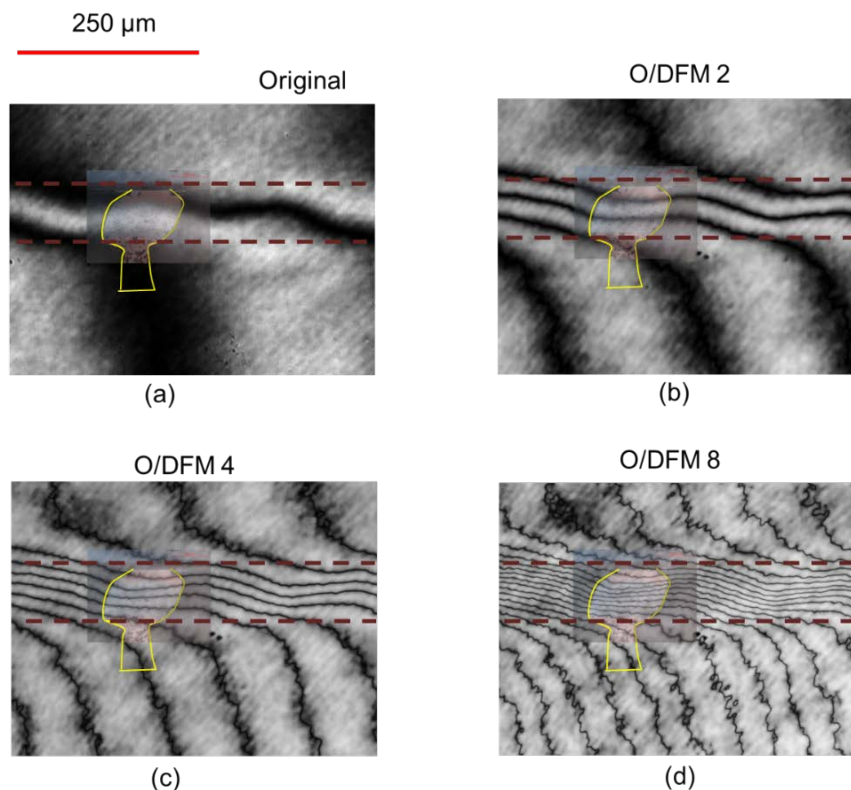

Figure 6-10 Fringe pattern captured in MMI system: (a) original (200 nm/fringe), (b) O/DFM 2 (100 nm/fringe), (c) O/DFM 4 (50 nm/fringe), and (d) O/DFM 8 (25 nm/fringe)

The result is shown in Figure 6-10a and the O/DFM method was used to enhance the resolution. Fringe pattern in Figure 6-10c has the similar contour interval to the U field fringe pattern in Figure 6-9c. But, it shows much better quality. O/DFM with factor 8 was applied to same fringe pattern (Figure 6-10a) and the displacement resolution of 25 nm/fringe was achieved. The shear strain at the corner solder bump is about -0.7% under the bi-thermal loading ΔT = -80 °C.

6.5. Conclusion

A high frequency grating (2500 lines/mm) was fabricated on a silicon substrate using lithography first. The square profile was subsequently modified by reactive-ion etching so that it can be used to produce a specimen grating by replication. Secondly, the algorithms of the optical/digital fringe multiplication method were improved to further enhance the measurement resolution of the immersion microscopic moiré interferometry. The system and the noise-free grating were used to analyze thermal deformations of micro-solder bumps. With the basic contour interval of 200 nm, the displacement resolution of 25 nm was achieved with the multiplication factor of 8.

Chapter 7 Contributions and Future Works

7.1. Dissertation Contributions

The moiré interferometry was advanced for investigating the rate-dependent deformation behavior of single grain SnAgCu solder and micromechanical deformations of microstructures in advanced packaging. The most significant contributions made in this dissertation are summarized below:

- The mechanical/optical configuration of moiré interferometry for real-time observation of thermal deformations was enhanced to provide measurement capabilities required for the analyses. Two most notable advancements are (1) development of a conduction-based thermal chamber for a wide range of ramp rates with accurate temperature control, and (2) implementation of microscope objectives in the imaging system to observe a microscopic field of view.
- A unique experimental study was conducted to measure the temperature dependent anisotropic CTE values of SAC305 grains. The accurate CTE values and the *c*-axis direction were determined from the theoretical relationship between the CTE values and the engineering strains which were measured by the advanced moiré interferometry system.
- A unique experimental study was conducted to quantify the highly anisotropic SAC305 solder grain's thermo-mechanical behavior under thermal cycling condition using a novel copper-steel specimen frame to provide well controlled loading. Detailed deformation evolutions and accumulated deformations were documented for the solder grains with different grain orientations. This can

lead more accurate anisotropic constitutive properties of Sn-based Pb-free solder alloys.

- An advanced immersion microscopic moiré interferometry system based on an achromatic configuration was developed and implemented for higher displacement sensitivity and spatial resolution.
- A high frequency silicon-based grating (2500 lines/mm) mode was fabricated to provide excellent fringe pattern quality and improved O/DFM algorithms were proposed. MMI system and the noise-free grating were used to analyze thermal deformations of micro-solder bumps. With basic contour interval of 200 nm, the displacement resolution of 25 nm was achieved with the multiplication factor of 8.

7.2. Future Works

The contributions by this dissertation can be extended in several directions. Some of them are described below:

Constitutive properties of SAC solder grain

There is lack of material properties for SAC solder grain's anisotropic elasticity, plasticity and creep. The advanced moiré interferometry system can be employed to document the micro/nano deformations of the solder grain under the well-controlled mechanical/thermal loading. Meanwhile, the method introduced in Chapter 3 and Chapter 4 can be used to fabricate a single solder grain specimen which is very critical to quantify the anisotropic mechanical properties. The detailed deformation evolutions and accumulated deformation data for solder grains with different orientations,

documented in Chapter 4, can be further utilized by the solder community to verify and improve their constitutive models and properties.

Reliability assessment of advanced electronic package

Both advanced moiré interferometry system and immersion-based microscopic moiré system provide high deformation resolution and spatial resolution. They are very useful tools for the thermo-mechanical deformation analyses. They can be effectively used to evaluate the mechanical design of new electronic components and subassemblies and facilitate FEA modeling for higher accuracy.

Appendix I: Fringe Evolutions during Thermal Cycles

Specimen 1:

Before 1st cycle

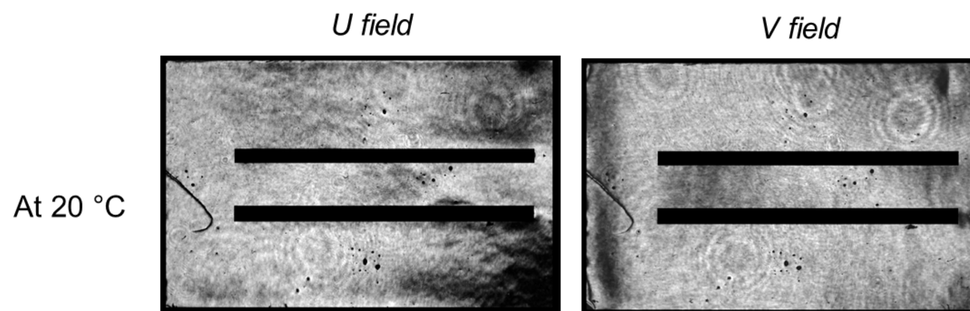

1st cycle

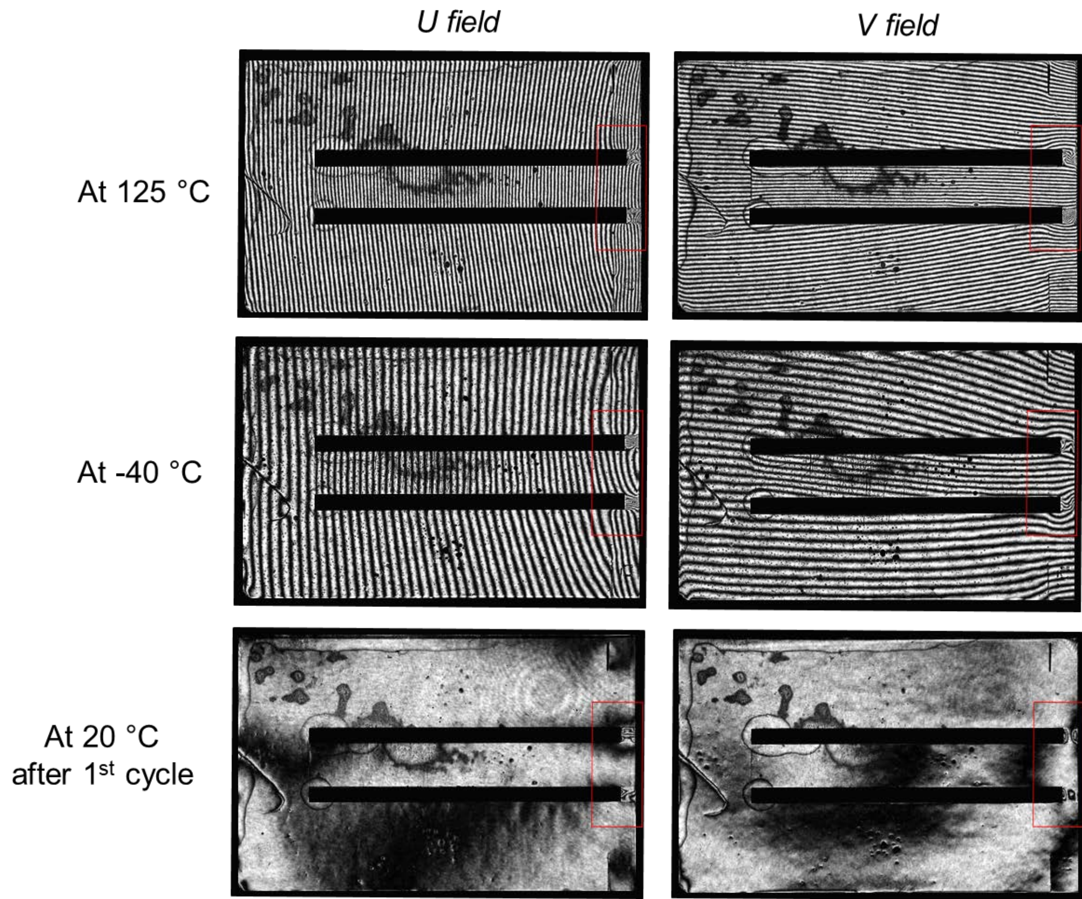

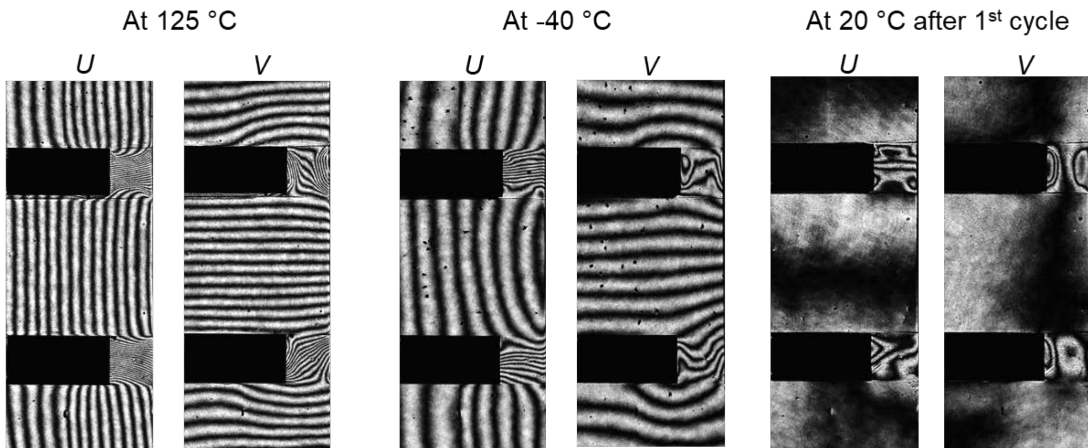

(a)

2nd cycle

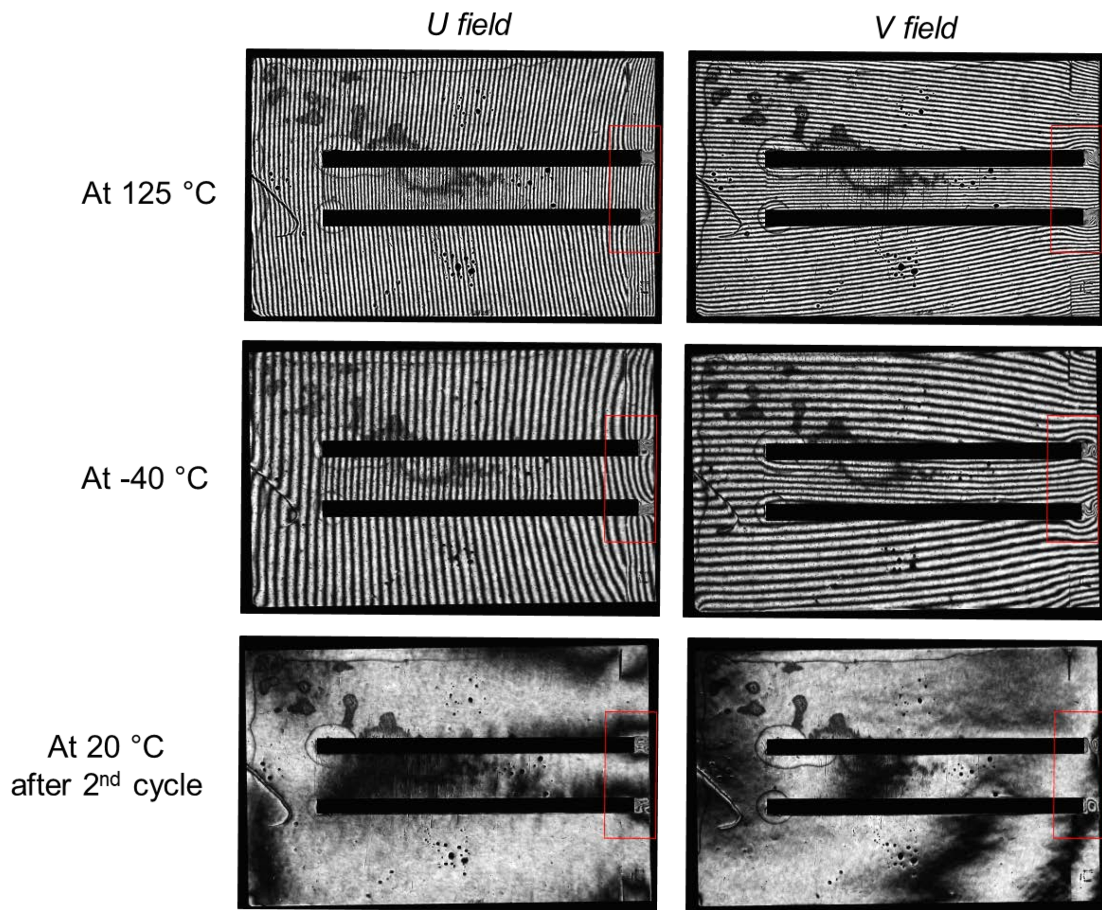

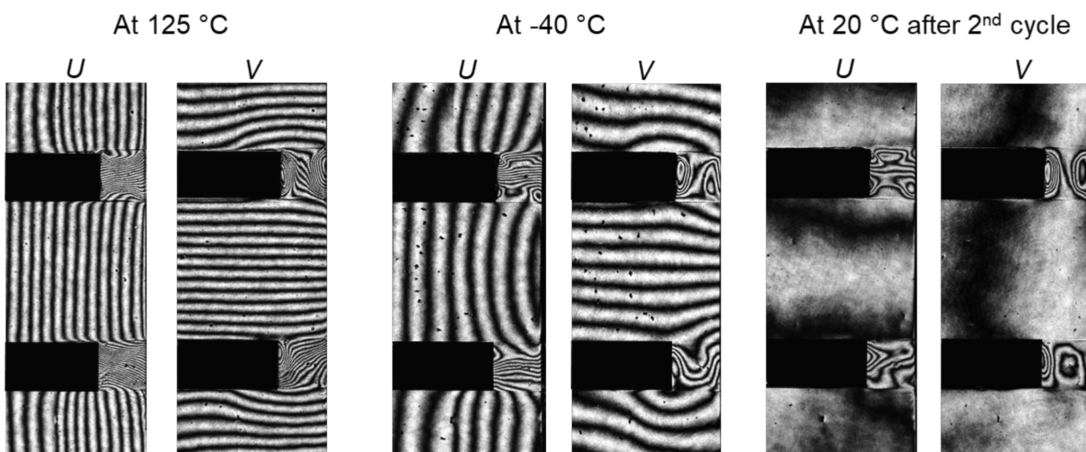

3rd cycle

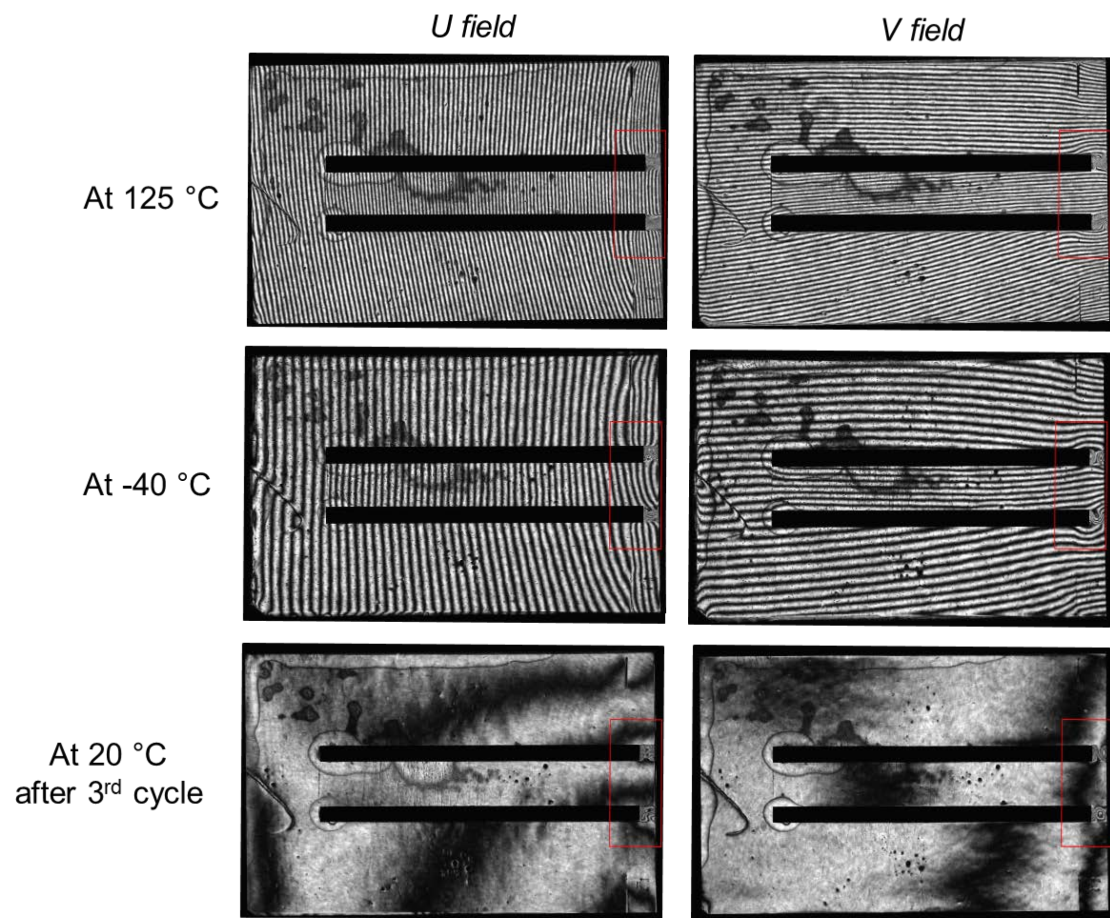

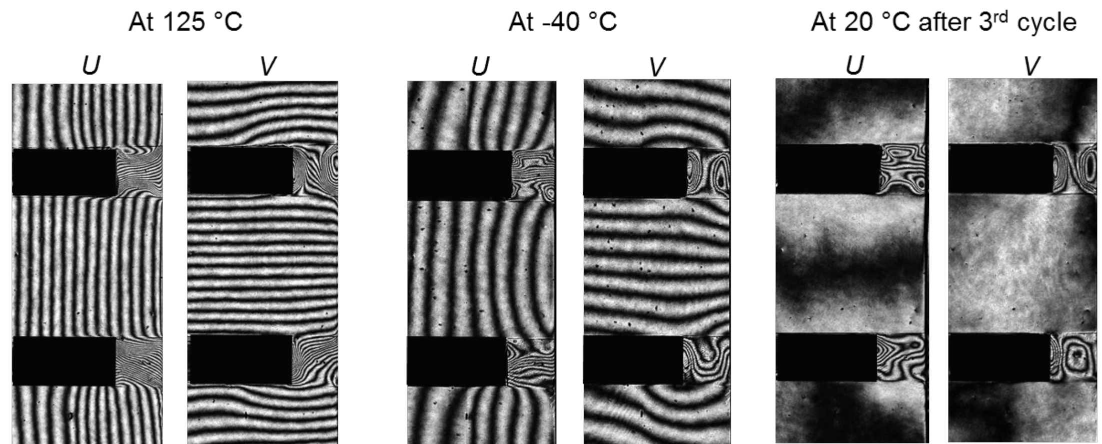

4th cycle

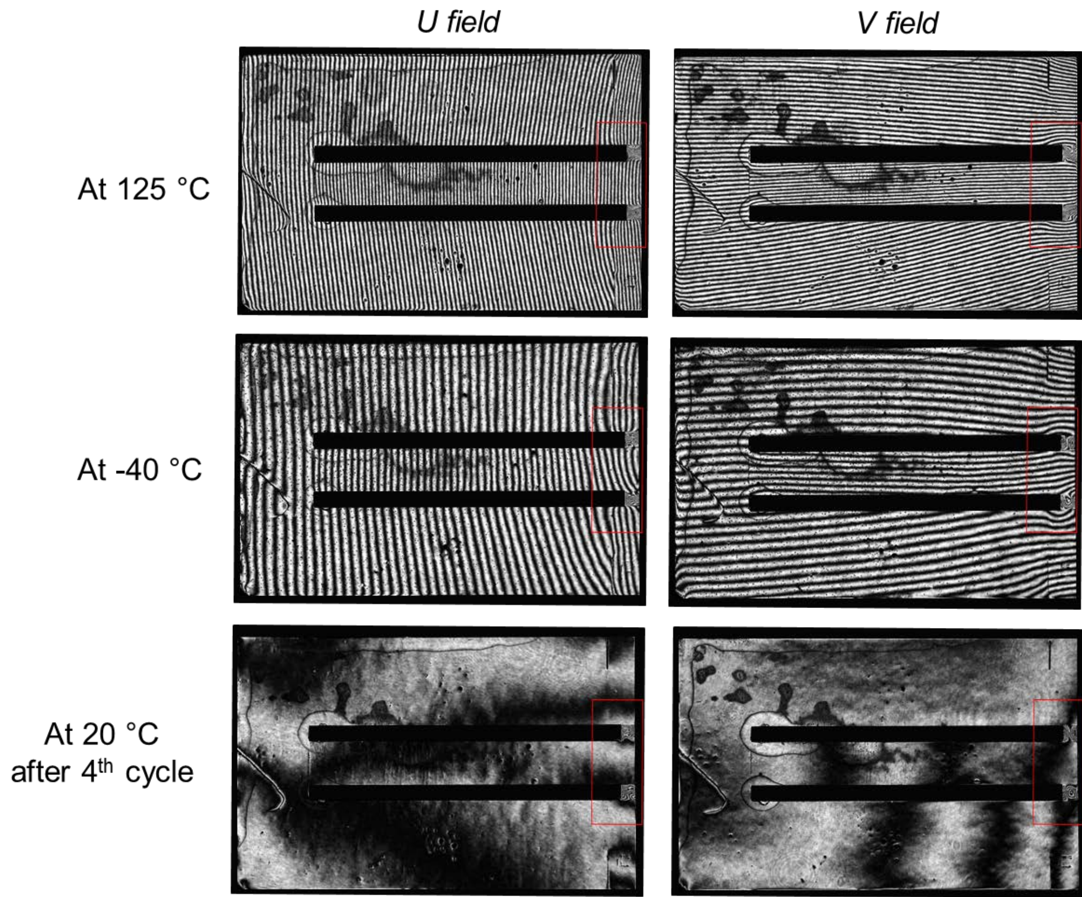

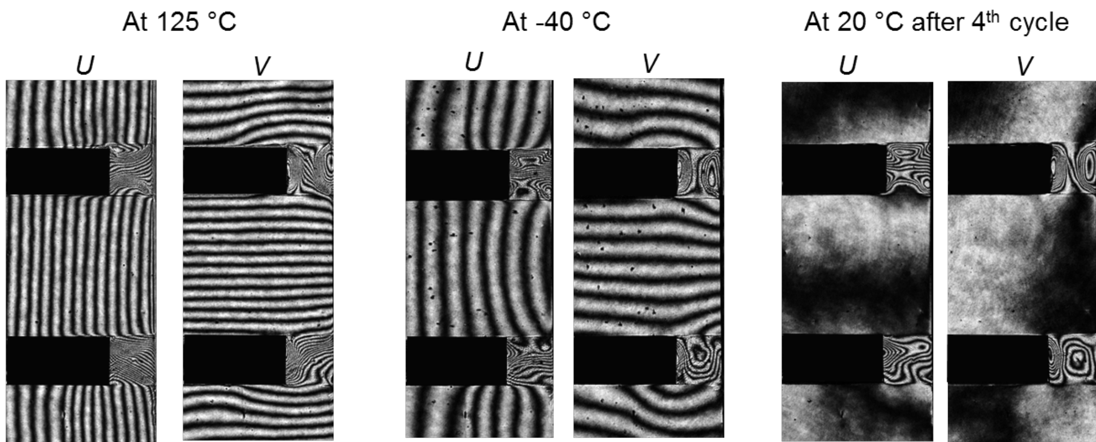

5th cycle

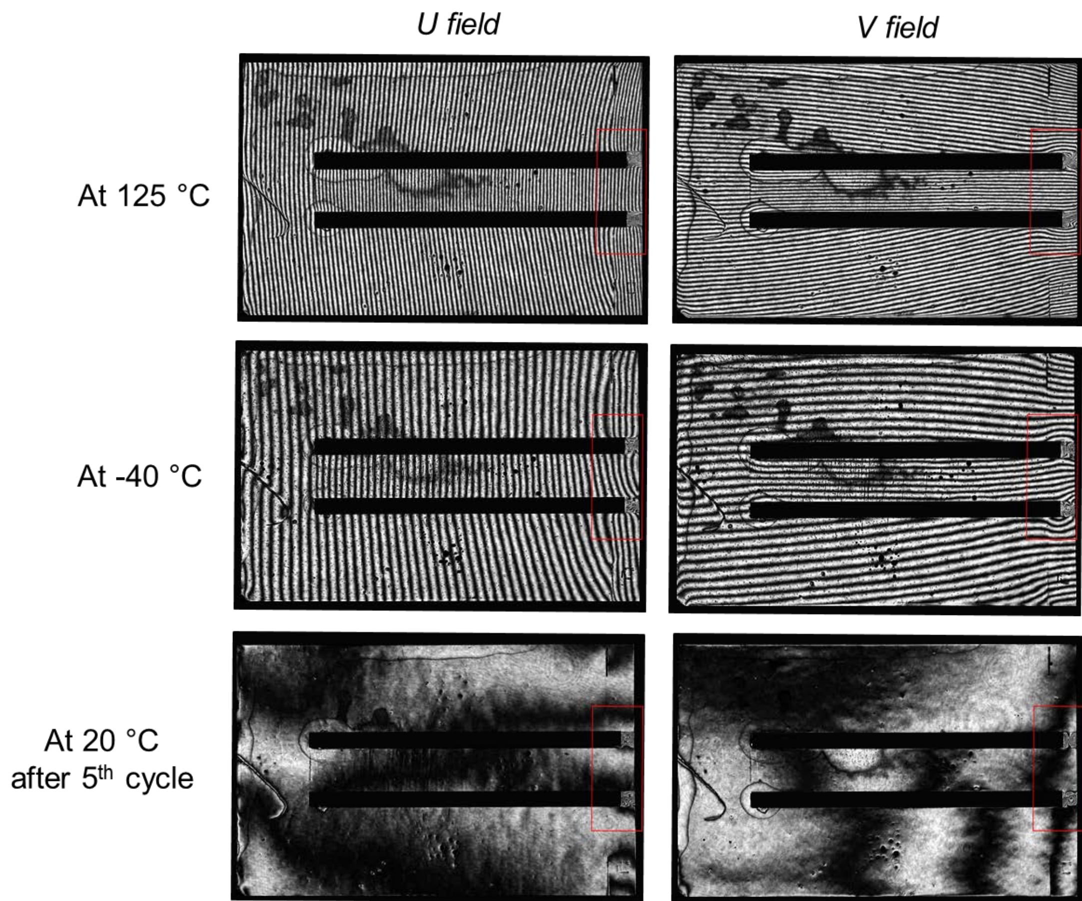

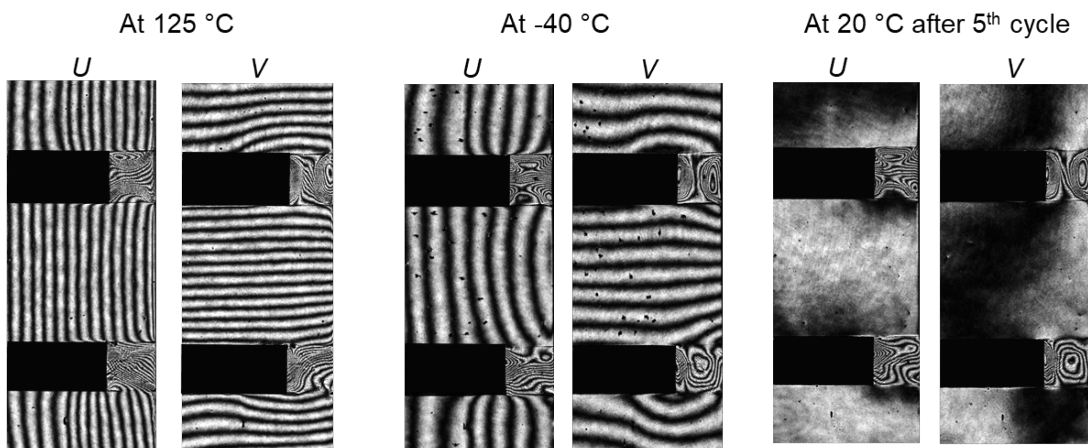

6th cycle

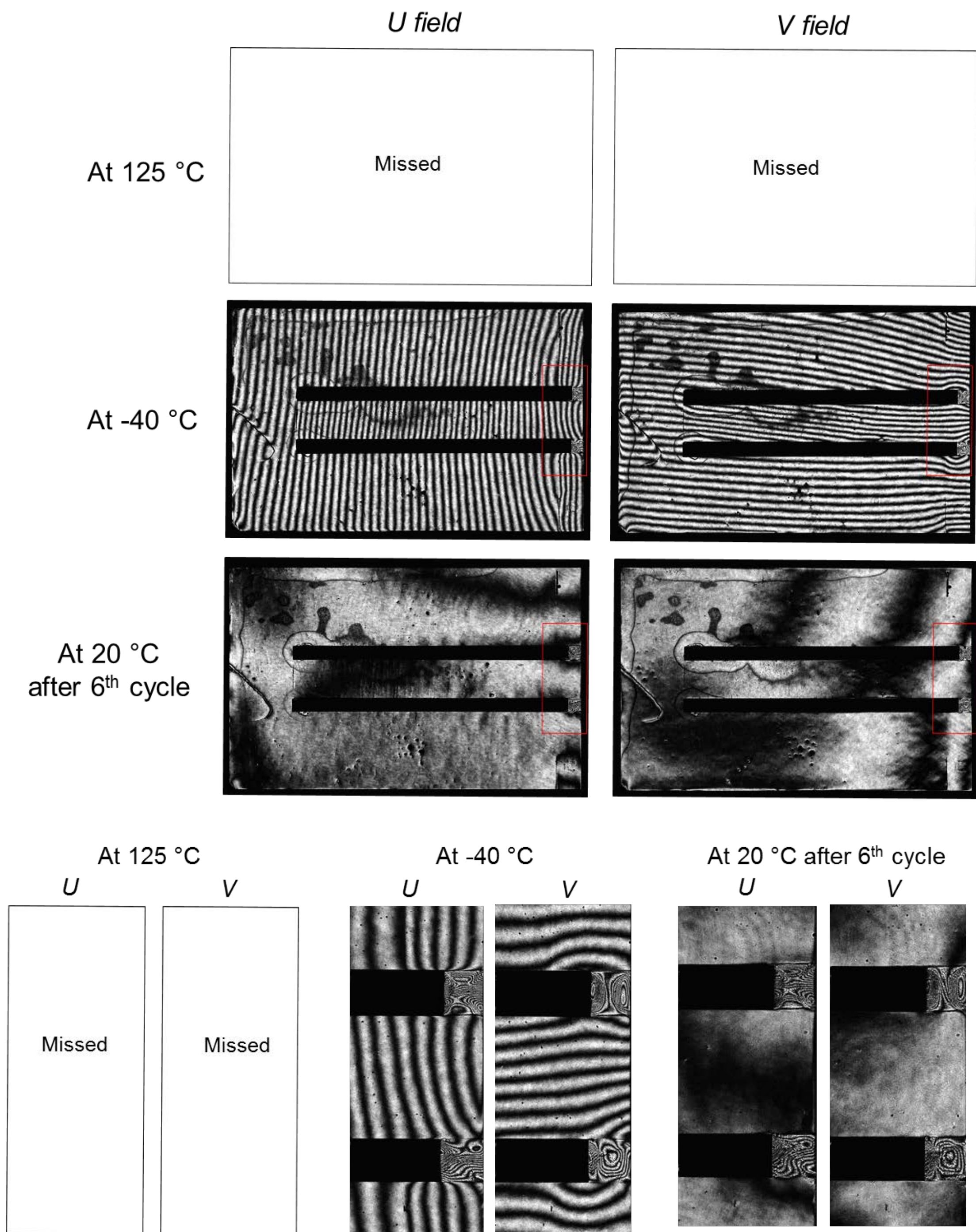

Specimen 2:

Before 1st cycle

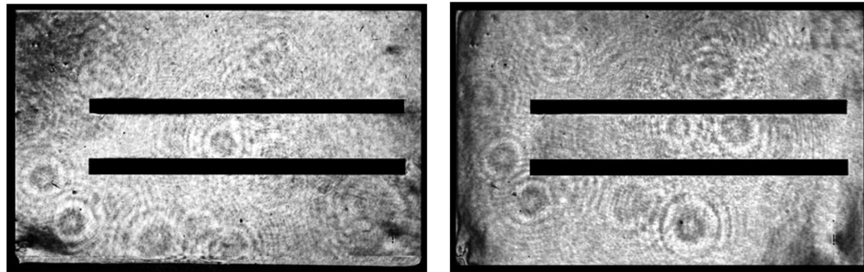

1st cycle

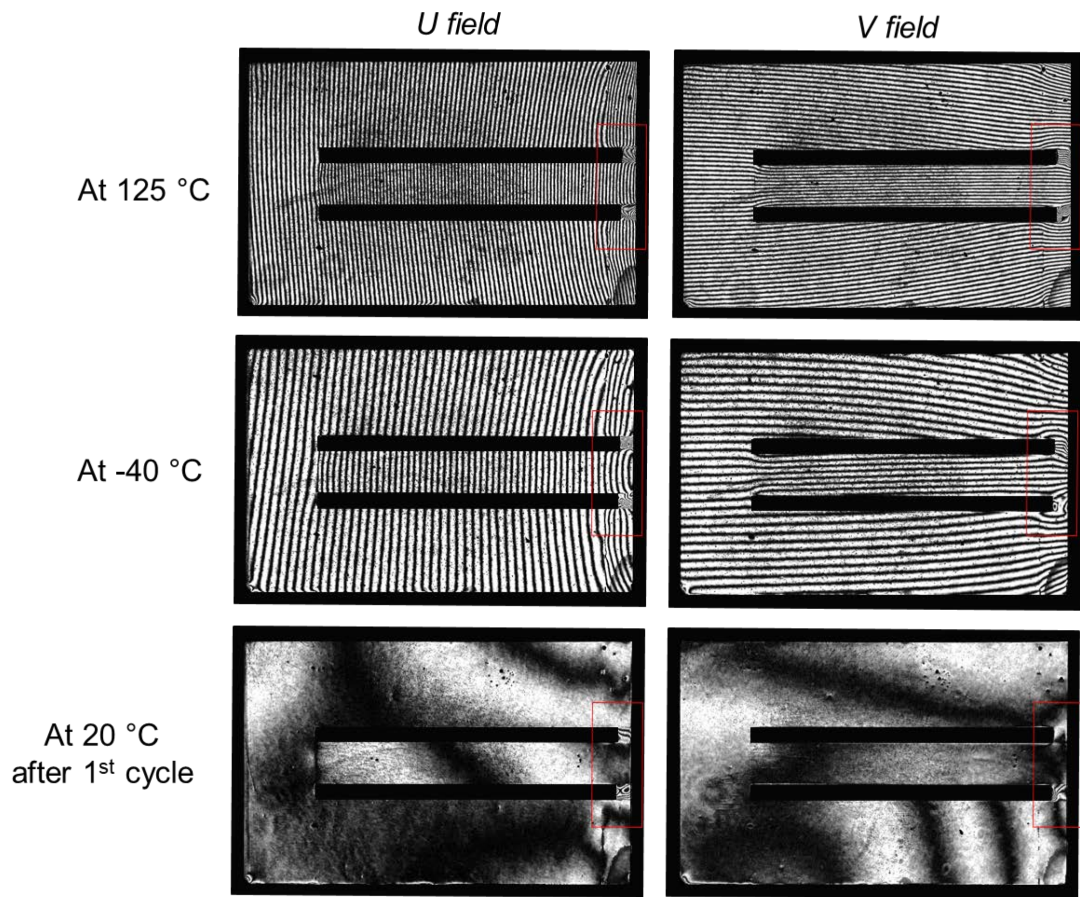

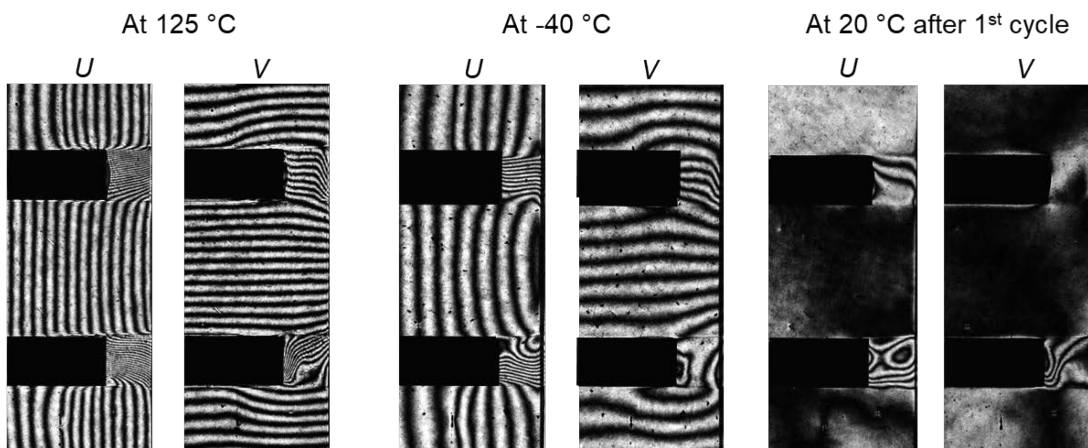

2nd cycle

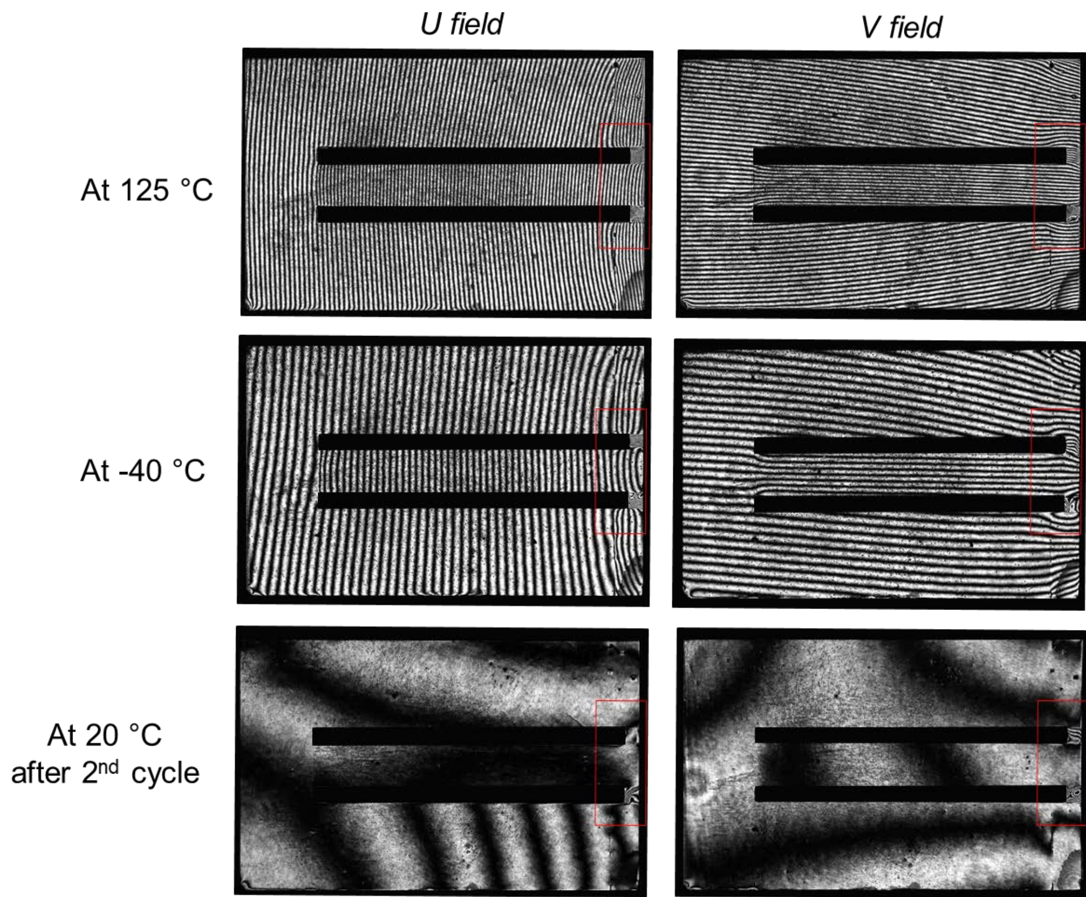

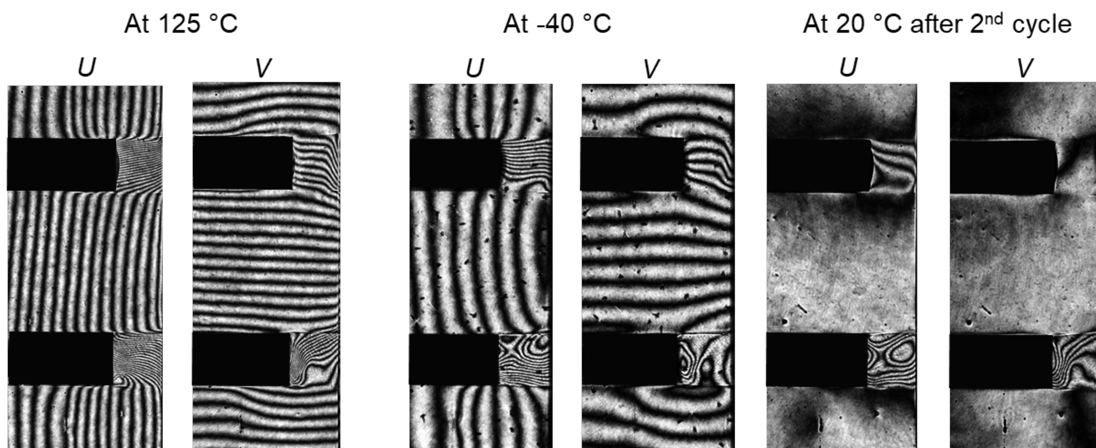

3rd cycle

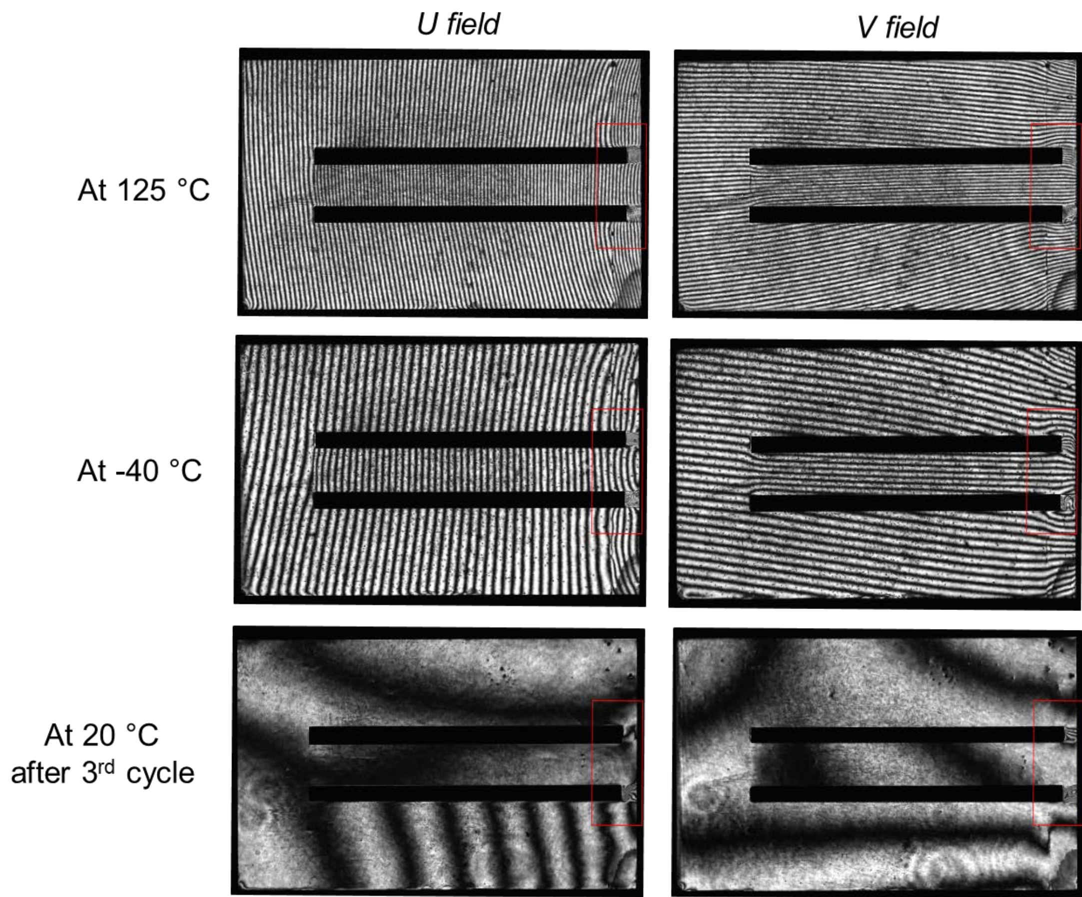

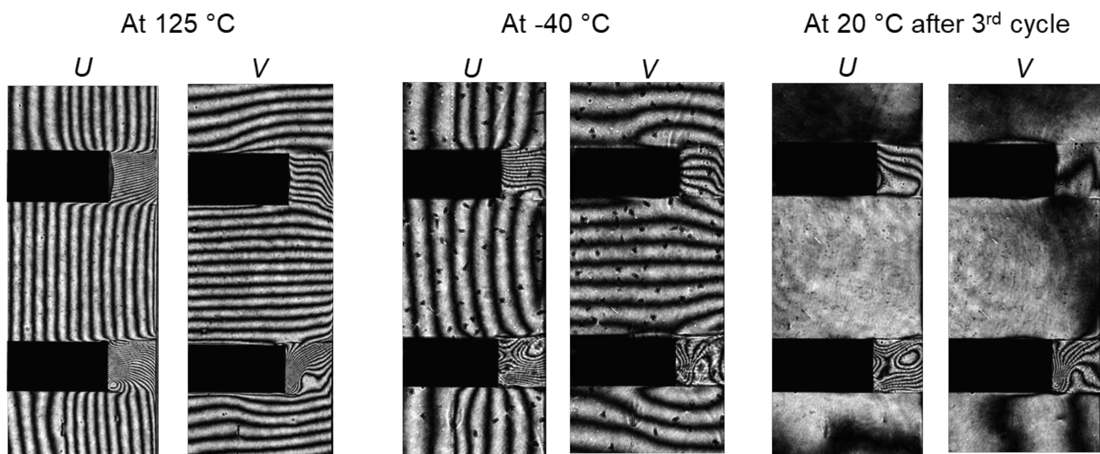

4th cycle

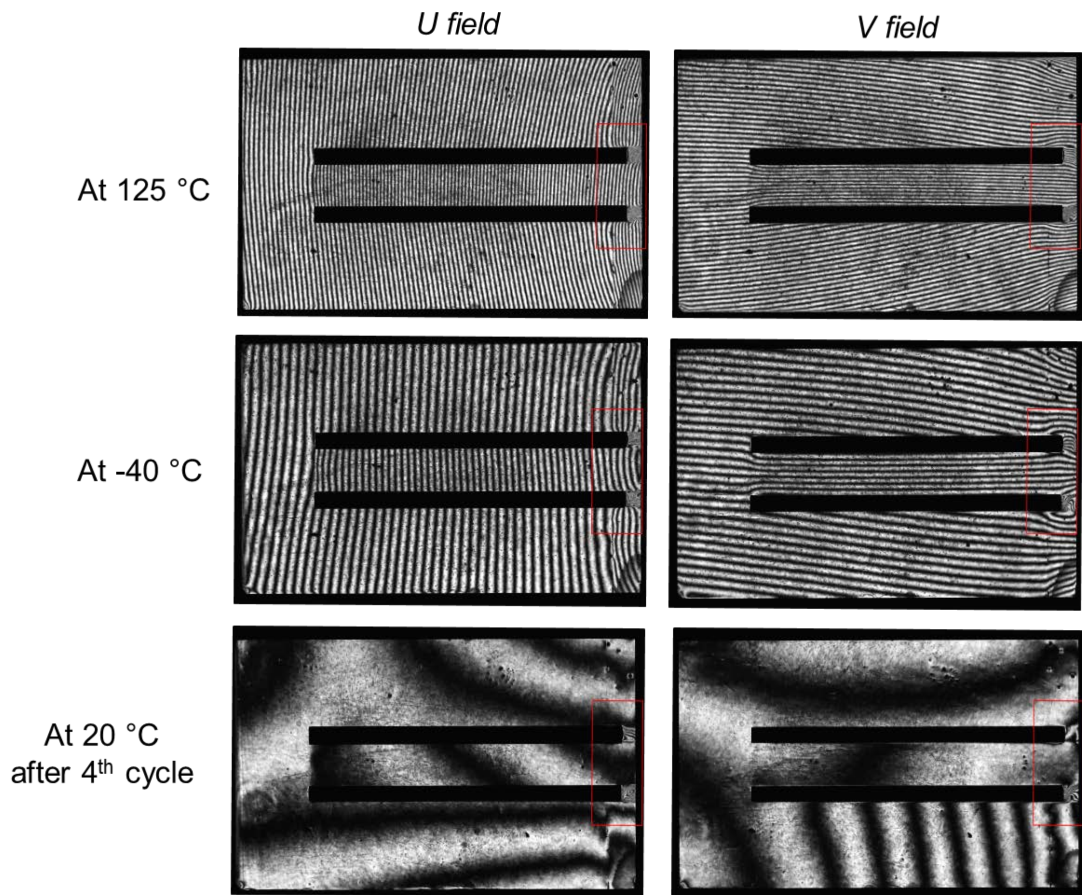

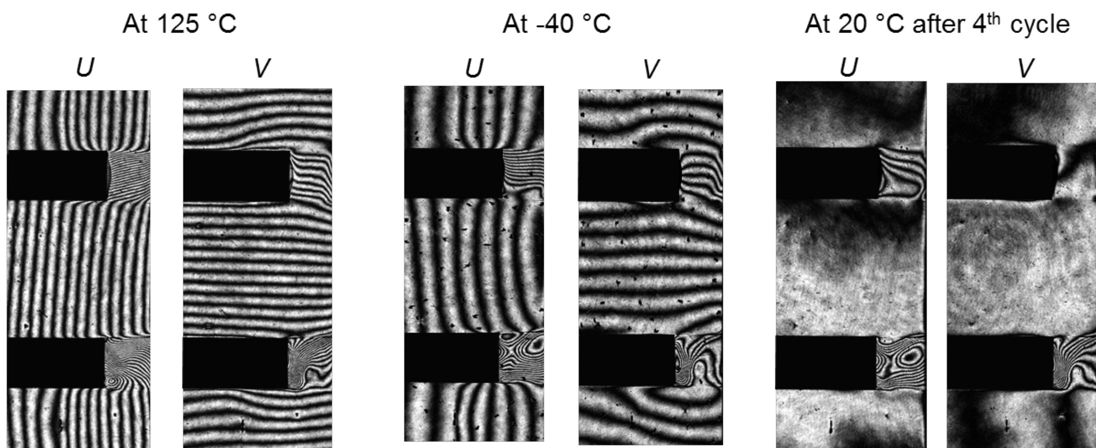

5th cycle

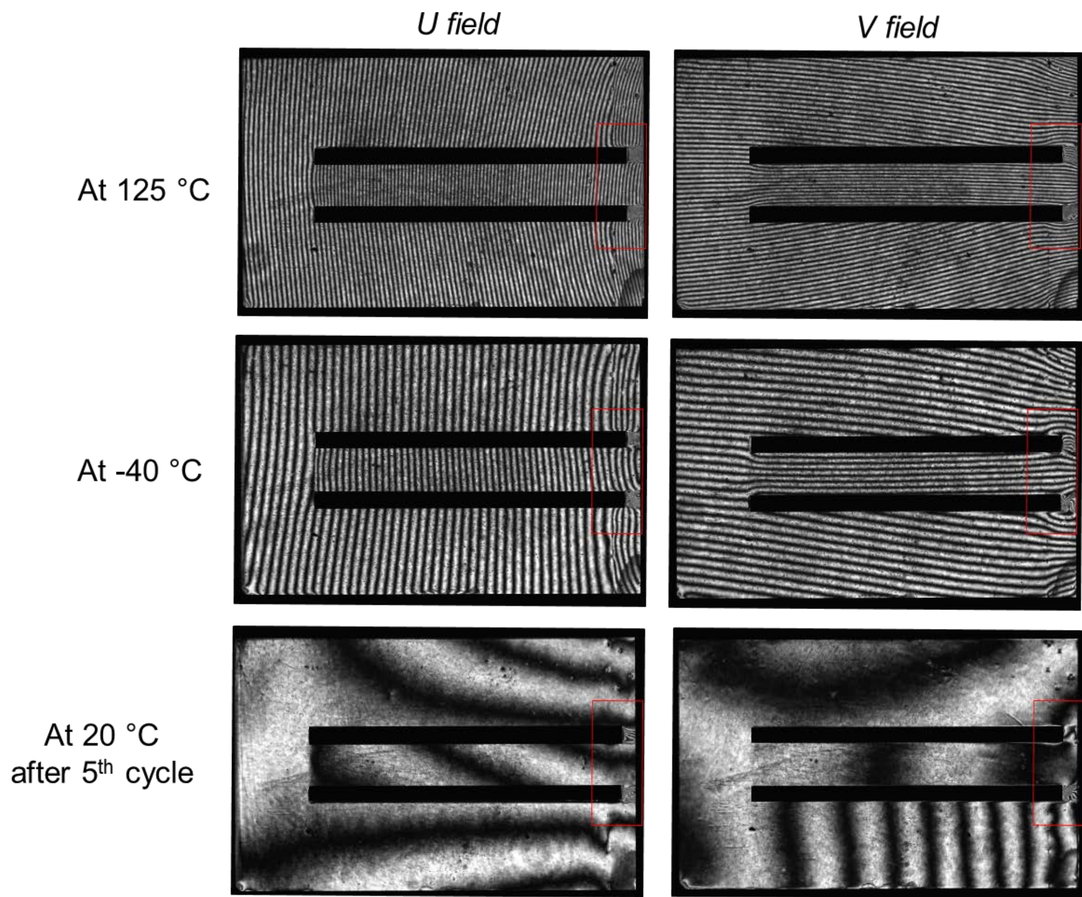

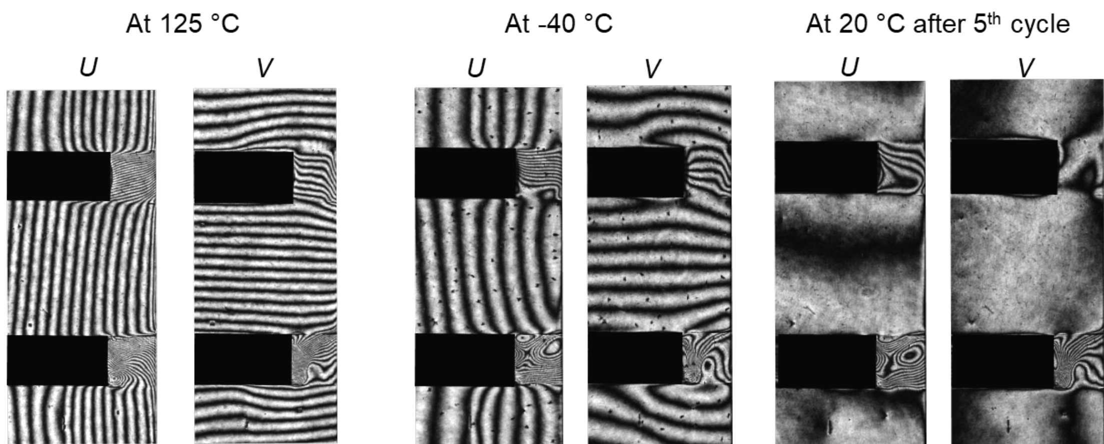

6th cycle

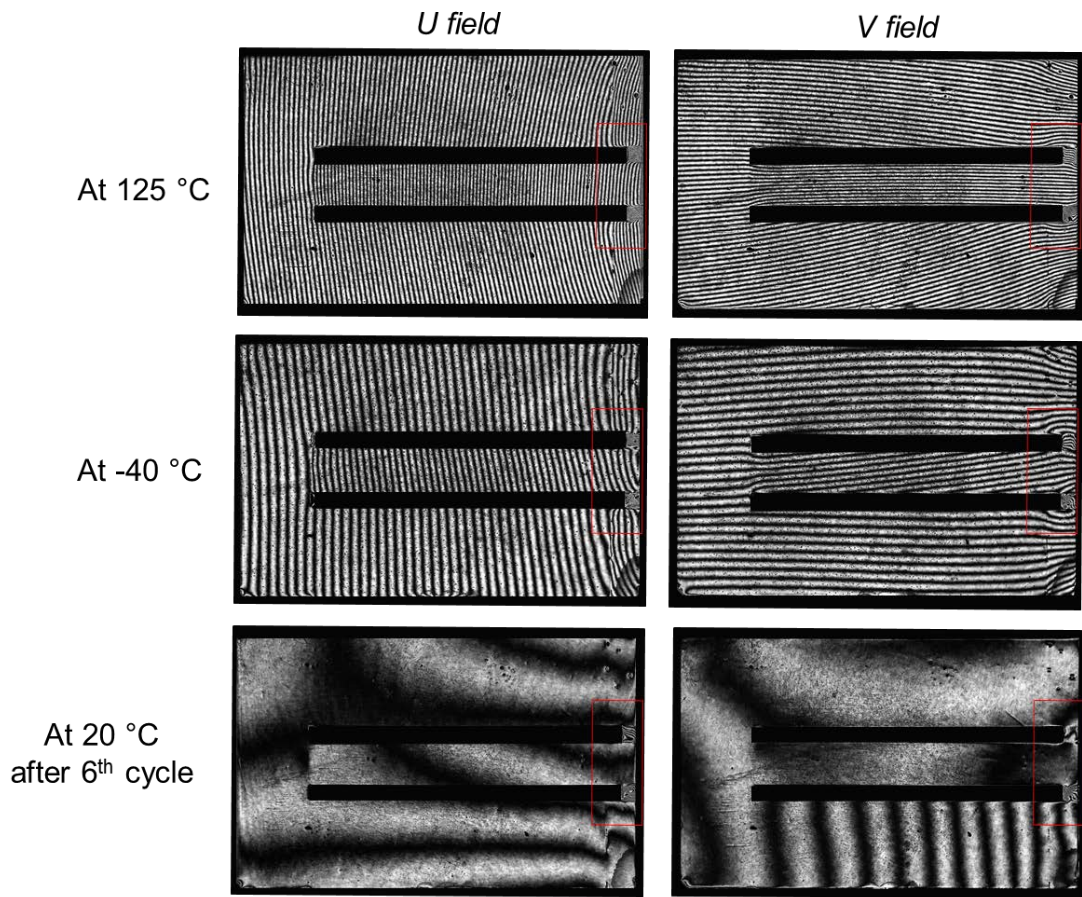

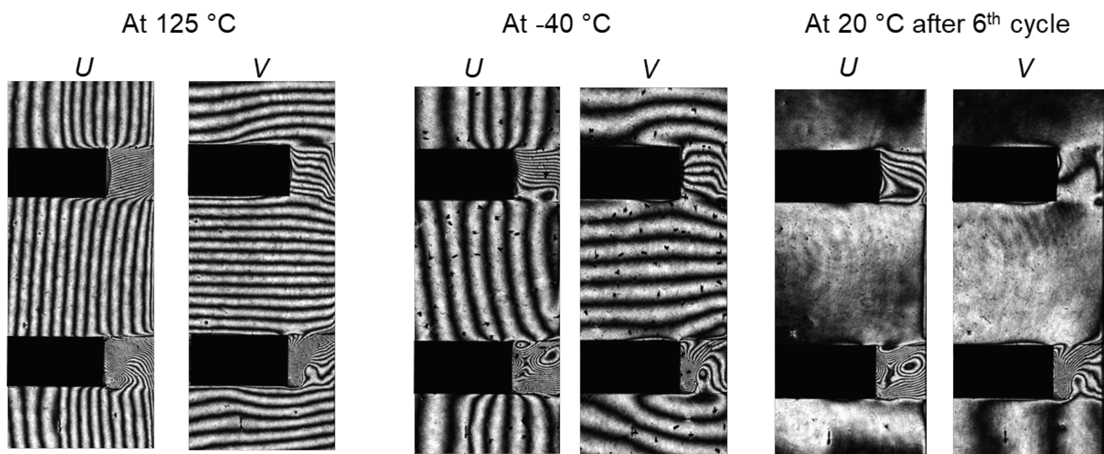

Appendix II: Constitutive Properties of SAC305 Solder

Solder materials show a temperature and time dependent behavior. The main available empirical constitutive models for the SAC305 solder are summarized below, where SAC305 solder is characterized as the isotropic material.

Partitioned model

In this model, the elasticity, time-independent plasticity and time-dependent creep are modeled separately to describe the solder behavior. The total strain ε can be expressed as[1]:

$$\varepsilon = \varepsilon_{el} + \varepsilon_{pl} + \varepsilon_{pcr} + \varepsilon_{scr} \tag{A-1}$$

where ε_{el}, ε_{pl}, ε_{pcr} and ε_{scr} are elastic strain, plastic strain, primary strain and secondary creep strain.

For the plasticity, Ramberg-Osgood strainpla hardening model is used [1]:

$$\varepsilon_{pl} = C_{pl}\left(T\right)\sigma^{n(T)} \tag{A-2}$$

For the primary creep, the generalized exponential model can be used [1]:

$$\varepsilon_{Sat} = C_1\sigma^{C_2};\ d = C_3\sigma^{C_4}\exp\left(-\frac{Q_1}{RT}\right) \tag{A-3}$$

$$\frac{\left(\varepsilon_{Sat} - \varepsilon_{pr}\right)}{\varepsilon_{Sat}} = \exp\left(-dt\right) \tag{A-4}$$

There are two main models to describe the secondary creep:

(1) Garofalo creep mode [1, 43, 75-77]:

$$\left(\frac{d\varepsilon}{dt}\right)_{\sec} = A_G\left(\sinh\left(\alpha\sigma\right)\right)^{n_G}\exp\left(-\frac{Q_2}{RT}\right) \tag{A-5}$$

(2) Double power creep model [1, 45]:

$$\left(\frac{d\gamma}{dt}\right)_{\sec} = A_L \left(\frac{\tau}{G(T)}\right)^{n_L} \exp\left(-\frac{Q_L}{RT}\right) + A_H \left(\frac{\tau}{G(T)}\right)^{n_H} \exp\left(-\frac{Q_H}{RT}\right) \quad \text{(A-6)}$$

Time hardening creep model is a form of combined primary and secondary creep [78]:

$$\varepsilon_{cr} = K\sigma^{n_e} t^q \exp\left(-\frac{Q_1}{RT}\right) + B\sigma^{m_e} t \exp\left(-\frac{Q_2}{RT}\right) \quad \text{(A-7)}$$

where ε_{pr} is equivalent primary creep strain, ε_{Sat} is equivalent primary saturated creep strain, d is decay, σ is equivalent stress, T is temperature, t is time, Q_i is activation energy, R is universal gas constant, τ is shear stress, γ is shear secondary creep strain, $G(T)$ is temperature dependent shear modulus, ε_{cr} is creep strain, C_i, n_i, A_i, K, B, m_e and q are model constants.

Unified Anand model

The plasticity and creep behavior are unified in the constitutive model. The total strain is:

$$\varepsilon = \varepsilon_{el} + \varepsilon_p \quad \text{(A-8)}$$

Flow equation

$$\dot{\varepsilon}_p = A(e^{-Q/RT})\left[\sinh\left(\xi \frac{\sigma}{s}\right)\right]^{1/m} \quad \text{(A-9)}$$

Equivalent stress

$$\sigma = cs \quad \text{(A-10)}$$

$$\sigma_o = cs_o \quad \text{(A-11)}$$

Evolution equation

$$\dot{s} = \left\{ h_o \left| \left(1 - \frac{s}{s^*} \right) \right|^a sign\left(1 - \frac{s}{s^*} \right) \right\} \dot{\varepsilon}_p \quad \text{(A-12)}$$

$$s^* = \bar{s} \left[\frac{\dot{\varepsilon}_p}{A} e^{Q/RT} \right]^n \quad \text{(A-13)}$$

where ε_p is inelastic strain, $\dot{\varepsilon}_p$ is the inelastic strain rate, σ is the equivalent stress for the steady plastic flow, s is an internal variable, s^* is the saturation value of s. Nine model constants are list in Table II-1.

Table II-1 Anand Model Constants

Parameter	Represented Property
s_o	Initial value of deformation resistance
Q/R	Q: Activation energy, R: Universal gas constant
A	Pre-exponential factor
ξ	Stress multiplier
m	Strain rate sensitivity of stress
h_o	Hardening/Softening constant
$\bar{S}$	Coefficient for deformation resistance saturation value
n	Strain rate sensitivity of saturation value
a	Strain rate sensitivity of hardening or softening

Anand model and Garofola secondary creep models are widely used in the packaging community. The existing data are shown in Table 4-2, Table II-2 to Table II-5.

Table II-2 Plastic model constants for SAC305 $\tau = C_{pl}\gamma_{pl}{}^n$ [56]

Shear modulus γ_{pl} (GPa)	C_{pl} (MPa)	n
19.305-0.0686*T (C)	51.0-0.18*T(°C)	0.23

Table II-3 Generalized exponential primary creep model constants for SAC305[1]

C_1 (MPa)	C_2	C_3	C_4	Q_1(J/mol)
1.85E-4	1.49	4.1E-2	3.9	39526

Table II-4 Garofalo secondary creep model constants for SAC305

	Vianco [75]	Darveaux [76]	Cuddalorepatta [1]	Punch [77]
C (sec^{-1})	2631	5.77E5	6.07	1.789677E10
α (MPa^{-1})	0.0453	0.0231	0.18	3.3490
n	5	7	2.3	6.83444
Q(J/mol)	52.4	57883	55793	87217.8

Table II-5 Anand model constants for SAC305

Parameter	Units	Punch [77, 79]	Mysore [78]	Motalab [80]	Motalab [80]
S_o	MPa	1.0665	2.15	21.00	18.07
Q/R	1/K	10,413.3	9970	9320	9096
A	1/sec	1.4283E8	17.994	3501	3484
ξ	-	1.472	0.35	4	4
m	-	0.141446	0.153	0.25	0.2
H_o	MPa	5023.9	1525.98	180,000	144,000
$\overline{S}$	MPa	20.2976	2.536	30.2	26.4
n	-	0.032472	0.028	0.01	0.01
a	-	1.120371	1.69	1.78	1.9

References

[1] G. Cuddalorepatta, "Evolution of the microstructure and viscoplastic behavior of microscale SAC305 solder joints as a function of mechanical fatigue damage," Ph.D. Dissertation, University of Maryland, College Park, 2010.

[2] C. Basaran and J. Jiang, "Measuring intrinsic elastic modulus of Pb/Sn solder alloys," *Mechanics of Materials,* vol. 34, pp. 349-362, 2002.

[3] H. Tang and C. Basaran, "Influence of microstructure coarsening on thermomechanical fatigue behavior of Pb/Sn eutectic solder joints," *International Journal of Damage Mechanics,* vol. 10, pp. 235-255, 2001.

[4] S. Mukherjee, B. Zhou, A. Dasgupta, and T. R. Bieler, "Multiscale modeling of the anisotropic transient creep response of heterogeneous single crystal SnAgCu solder," *International Journal of Plasticity,* vol. 78, pp. 1-25, 2016.

[5] D. W. Henderson, J. J. Woods, T. A. Gosselin, J. Bartelo, D. E. King, T. Korhonen, M. Korhonen, L. Lehman, E. Cotts, and S. K. Kang, "The microstructure of Sn in near-eutectic Sn–Ag–Cu alloy solder joints and its role in thermomechanical fatigue," *Journal of Materials Research,* vol. 19, pp. 1608-1612, 2004.

[6] T. R. Bieler, H. Jiang, L. P. Lehman, T. Kirkpatrick, E. J. Cotts, and B. Nandagopal, "Influence of Sn grain size and orientation on the thermomechanical response and reliability of Pb-free solder joints," *IEEE Transactions on components and Packaging Technologies,* vol. 31, pp. 370-381, 2008.

[7] T.-K. Lee, B. Zhou, L. Blair, K.-C. Liu, and T. R. Bieler, "Sn-Ag-Cu solder joint microstructure and orientation evolution as a function of position and thermal cycles in ball grid arrays using orientation imaging microscopy," *Journal of Electronic Materials,* vol. 39, pp. 2588-2597, 2010.

[8] D. A. Shnawah, M. F. M. Sabri, and I. A. Badruddin, "A review on thermal cycling and drop impact reliability of SAC solder joint in portable electronic products," *Microelectronics Reliability,* vol. 52, pp. 90-99, 2012.

[9] S. Park, R. Dhakal, L. Lehman, and E. J. Cotts, "Grain deformation and strain in board level SnAgCu solder interconnects under deep thermal cycling," *IEEE Transactions on components and Packaging Technologies,* vol. 30, pp. 178-185, 2007.

[10] H. Chen, B. Yan, M. Yang, X. Ma, and M. Li, "Effect of grain orientation on mechanical properties and thermomechanical response of Sn-based solder interconnects," *Materials Characterization,* vol. 85, pp. 64-72, 2013.

[11] T. Bieler, H. Jiang, L. Lehman, T. Kirkpatrick, and E. Cotts, "Influence of Sn grain size and orientation on the thermomechanical response and reliability of Pb-free solder joints," in *Electronic Components and Technology Conference, 2006. Proceedings. 56th*, 2006, p. 6 pp.

[12] G. R. Halford, M. H. Hirschberg, and S. Manson, "Temperature effects on the strainrange partitioning approach for creep fatigue analysis," in *Fatigue at Elevated Temperatures*, ed: ASTM International, 1973.

[13] A. Dasgupta, C. Oyan, D. Barker, and M. Pecht, "Solder creep-fatigue analysis by an energy-partitioning approach," *ASME Journal of Electronic Packaging,* vol. 114, pp. 152-160, 1992.

[14] S. Mukherjee, M. Nuhi, A. Dasgupta, and M. Modarres, "Creep constitutive models suitable for solder alloys in electronic assemblies," *Journal of Electronic Packaging,* vol. 138, p. 030801, 2016.

[15] S. Mukherjee, "Multiscale modeling of the anisotropic creep response of SnAgCu single crystal," Ph.D. Dissertation, University of Maryland, College Park, 2015.

[16] S. Park, R. Dhakal, L. Lehman, and E. Cotts, "Measurement of deformations in SnAgCu solder interconnects under in situ thermal loading," *Acta materialia,* vol. 55, pp. 3253-3260, 2007.

[17] D. Post, B. Han, and P. Ifju, *High Sensitivity Moiré: Experimental Analysis for Mechanics and Materials*: Springer Science & Business Media, 1997.

[18] Y. Guo, C. K. Lim, W. T. Chen, and C. G. Woychik, "Solder ball connect (SBC) assemblies under thermal loading: I. Deformation measurement via moiré interferometry, and its interpretation," *IBM Journal of Research and Development,* vol. 37, pp. 635-648, 1993.

[19] M. Variyam and B. Han, "DMD^{TM} Package Model Calibration Using Interferometry," *TI Technical Journal,* pp. 1-9, 2001.

[20] B. Han and Y. Guo, "Determination of an effective coefficient of thermal expansion of electronic packaging components: A whole-field approach," *IEEE Transactions on Components, Packaging, and Manufacturing Technology: Part A,* vol. 19, pp. 240-247, 1996.

[21] D. Zou, J. Wang, W. Yang, and S. Liu, "CTE-measurement and delamination growth by a real time Moire technique," in *Electronic Components and Technology Conference, 1997. Proceedings., 47th*, 1997, pp. 1124-1127.

[22] B. Han, "Recent advancements of moiré and microscopic moiré interferometry for thermal deformation analyses of microelectronics devices," *Experimental Mechanics,* vol. 38, pp. 278-288, 1998.

[23] J.-H. Zhao, X. Dai, and P. S. Ho, "Analysis and modeling verification for thermal-mechanical deformation in flip-chip packages," in *Electronic Components & Technology Conference, 1998. 48th IEEE*, 1998, pp. 336-344.

[24] B. Han and P. Kunthong, "Micro-mechanical deformation analysis of surface laminar circuit in organic flip-chip package: an experimental study," *Transactions-american Society of Mechanical Engineers Journal of Electronic Packaging,* vol. 122, pp. 294-300, 2000.

[25] S. Cho and B. Han, "Observing Real-Time Thermal Deformations In Electronic Packaging," *Experimental Techniques,* vol. 26, pp. 25-29, 2002.

[26] S.-J. Ham, W.-S. Kwon, K.-W. Paik, and S.-B. Lee, "In-situ moire measurement of adhesive flip-chip bonded assembly under thermal cycling condition," in *Polymers and Adhesives in Microelectronics and Photonics, 2002. Polytronic 2002. 2nd International IEEE Conference on*, 2002, pp. 63-67.

[27] B. Han, "Thermal stresses in microelectronics subassemblies: quantitative characterization using photomechanics methods," *Journal of Thermal Stresses,* vol. 26, pp. 583-613, 2003.

[28] S. Cho, B. Han, and J. Joo, "Temperature dependent deformation analysis of ceramic ball grid array package assembly under accelerated thermal cycling condition," *Transactions-American Society of Mechanical Engineers Journal of Electronic Packaging,* vol. 126, pp. 41-47, 2004.

[29] J. Joo, S. Cho, and B. Han, "Characterization of flexural and thermo-mechanical behavior of plastic ball grid package assembly using moiré interferometry," *Microelectronics Reliability,* vol. 45, pp. 637-646, 2005.

[30] D.-S. Kim, B. Han, A. Yadur, and P. J. Gromala, "Electronic control package model calibration using moiré interferometry," in *Thermal, mechanical and multi-physics simulation and experiments in microelectronics and microsystems (eurosime), 2014 15th international conference on*, 2014, pp. 1-5.

[31] B. Wu, D.-S. Kim, B. Han, A. Palczynska, and P. J. Gromala, "Thermal deformation analysis of automotive electronic control units subjected to passive and active thermal conditions," in *Thermal, Mechanical and Multi-Physics Simulation and Experiments in Microelectronics and Microsystems (EuroSimE), 2015 16th International Conference on*, 2015, pp. 1-6.

[32] B. Wu, D.-S. Kim, B. Han, A. Palczynska, A. Prisacaru, and P. J. Gromala, "Hybrid Approach to Conduct Failure Prognostics of Automotive Electronic Control Unit," in *Electronic Components and Technology Conference (ECTC), 2017 IEEE 67th*, 2017, pp. 476-482.

[33] G. Sharma, S. W. Yoon, M. Prashant, R. Emigh, S. J. Lee, K. Liu, and R. Pendse, "Performance & reliability characterization of eWLB (embedded wafer level BGA) packaging," in *Electronics Packaging Technology Conference (EPTC), 2010 12th*, 2010, pp. 211-216.

[34] S. Yoon, Y. Lin, S. Gaurav, Y. Jin, V. Ganesh, T. Meyer, P. C. Marimuthu, X. Baraton, and A. Bahr, "Mechanical characterization of next generation eWLB (embedded wafer level BGA) packaging," in *Electronic Components and Technology Conference (ECTC), 2011 IEEE 61st*, 2011, pp. 441-446.

[35] S. W. Yoon, J. A. Caparas, Y. Lin, and P. C. Marimuthu, "Advanced low profile PoP solution with embedded wafer level PoP (eWLB-PoP) technology," in *Electronic Components and Technology Conference (ECTC), 2012 IEEE 62nd*, 2012, pp. 1250-1254.

[36] A. Rodrigo, B. Isabel, C. José, C. Paulo, C. José, H. Vítor, and P. Nelson, "Enabling of Fan-Out WLP for more demanding applications by introduction of enhanced dielectric material for higher reliability," in *Electronic Components and Technology Conference (ECTC), 2014 IEEE 64th*, 2014, pp. 935-939.

[37] C.-Y. Chou, T.-Y. Hung, S.-Y. Yang, M.-C. Yew, W.-K. Yang, and K.-N. Chiang, "Solder joint and trace line failure simulation and experimental validation of fan-out type wafer level packaging subjected to drop impact," *Microelectronics Reliability,* vol. 48, pp. 1149-1154, 2008.

[38] B. Keser, R. Alvarado, M. Schwarz, and S. Bezuk, "0.35 mm pitch wafer level package board level reliability: Studying effect of ball de-population with varying ball size," in *Electronic Components and Technology Conference (ECTC), 2015 IEEE 65th*, 2015, pp. 1090-1095.

[39] Y. Kurita, T. Kimura, K. Shibuya, H. Kobayashi, F. Kawashiro, N. Motohashi, and M. Kawano, "Fan-Out Wafer-Level Packaging with highly flexible design capabilities," in *Electronic System-Integration Technology Conference (ESTC), 2010 3rd*, 2010, pp. 1-6.

[40] J. Xi, D. Yang, L. Bai, X. Zhai, F. Xiao, H. Guo, L. Zhang, and C. M. Lai, "Reliability of RDL structured wafer level packages," in *Electronic Packaging Technology (ICEPT), 2013 14th International Conference on*, 2013, pp. 1029-1032.

[41] D. Post, B. Han, and P. Ifju, *High sensitivity moiré: experimental analysis for mechanics and materials*: Springer Science & Business Media, 2012.

[42] E. Stellrecht, B. Han, and M. G. Pecht, "Characterization of hygroscopic swelling behavior of mold compounds and plastic packages," *IEEE Transactions on components and Packaging Technologies,* vol. 27, pp. 499-506, 2004.

[43] F. Garofalo, *Fundamentals of creep and creep-rupture in metals*: Macmillan, 1965.

[44] B. Han, "Interferometric methods with enhanced sensitivity by optical/digital fringe multiplication," *Applied optics,* vol. 32, pp. 4713-4718, 1993.

[45] J. Morris, H. Song, and F. Hua, "Creep properties of Sn-rich solder joints," in *Electronic Components and Technology Conference, 2003. Proceedings. 53rd*, 2003, pp. 54-57.

[46] D. Suryanarayana, R. Hsiao, T. Gall, and J. McCreary, "Flip-chip solder bump fatigue life enhanced by polymer encapsulation," in *Electronic Components and Technology Conference, 1990.., 40th*, 1990, pp. 338-344.

[47] Y. Tsukada, Y. Mashimoto, T. Nishio, and N. Mii, "Reliability and Stress Analysis of Encapsulated Flip Chip Joint on Epoxy Base Printed Circuit Board," *Proceedings of ASME/JSME Joint Conference for Advanced in Electronics Packaging,* pp. 827-835, 1992.

[48] B. Han and Y. Guo, "Thermal deformation analysis of various electronic packaging products by moiré and microscopic moiré interferometry," *Journal of Electronic Packaging,* vol. 117, pp. 185-191, 1995.

[49] V. Deshpande and D. Sirdeshmukh, "Thermal expansion of tetragonal tin," *Acta Crystallographica,* vol. 14, pp. 355-356, 1961.

[50] V. Deshpande and D. Sirdeshmukh, "Thermal expansion of tin in the β–γ transition region," *Acta Crystallographica,* vol. 15, pp. 294-295, 1962.

[51] J. J. Sundelin, S. T. Nurmi, and T. K. Lepistö, "Recrystallization behaviour of SnAgCu solder joints," *Materials Science and Engineering: A,* vol. 474, pp. 201-207, 2008.

[52] D. Post, B. Han, and P. Ifju, *High Sensitivity Moiré: Experimental Analysis for Mechanics and Materials*. NY: Mechanical Engineering Series, Springer-Verlag, 1994.

[53] B. Wu and B. Han, "Advanced Mechanical/Optical Configuration of Real-Time Moiré Interferometry for Thermal Deformation Analysis of Fan-Out Wafer Level Package," *IEEE Transactions on Components, Packaging and Manufacturing Technology,* 2018.

[54] M. Mueller, S. Wiese, M. Roellig, and K.-J. Wolter, "Effect of composition and cooling rate on the microstructure of SnAgCu-solder joints," in *Electronic Components and Technology Conference, 2007. ECTC'07. Proceedings. 57th*, 2007, pp. 1579-1588.

[55] O. Engler and V. Randle, *Introduction to texture analysis: macrotexture, microtexture, and orientation mapping*: CRC press, 2009.

[56] Q. Zhang, "Isothermal mechanical and thermo-mechanical durability characterization of selected Pb-free solders," Ph.D. Dissertation, University of Maryland, College Park, 2004.

[57] M. Mathew, H. Yang, S. Movva, and K. Murty, "Creep deformation characteristics of tin and tin-based electronic solder alloys," *Metallurgical and Materials Transactions A,* vol. 36, pp. 99-105, 2005.

[58] S. Cho, "Development of Moiré Interferometry for Real-time Observation of Nonlinear Thermal Deformations of Solder and Solder Assembly," Ph.D. Dissertation, University of Maryland, College Park, 2005.

[59] J. H. Lau and Y.-H. Pao, *Solder joint reliability of BGA, CSP, flip chip, and fine pitch SMT assemblies*: McGraw-Hill Professional Publishing, 1997.

[60] Y. Kanda and Y. Kariya, "Evaluation of creep properties for Sn–Ag–Cu micro solder joint by multi-temperature stress relaxation test," *Microelectronics Reliability,* vol. 52, pp. 1435-1440, 2012.

[61] D. W. Henderson, T. Gosselin, A. Sarkhel, S. K. Kang, W.-K. Choi, D.-Y. Shih, C. Goldsmith, and K. J. Puttlitz, "Ag 3 Sn plate formation in the solidification of near ternary eutectic Sn–Ag–Cu alloys," *Journal of Materials Research,* vol. 17, pp. 2775-2778, 2002.

[62] Z. Wang, "Development and application of computer-aided fringe analysis," Ph.D. Dissertation
University of Maryland, College Park, 2003.

[63] Z. Wang and B. Han, "Advanced iterative algorithm for phase extraction of randomly phase-shifted interferograms," *Optics letters,* vol. 29, pp. 1671-1673, 2004.

[64] D. House and E. Vernon, "Determination of the elastic moduli of tin single crystals, and their variation with temperature," *British Journal of Applied Physics,* vol. 11, p. 254, 1960.

[65] J. Rayne and B. Chandrasekhar, "Elastic Constants of β Tin from 4.2 K to 300 K," *Physical Review,* vol. 120, p. 1658, 1960.

[66] B. Han and D. Post, "Immersion interferometer for microscopic moiré interferometry," *Experimental Mechanics,* vol. 32, pp. 38-41, 1992.

[67] D. Maystre, "I Rigorous Vector Theories of Diffraction Gratings," *Progress in optics,* vol. 21, pp. 1-67, 1984.

[68] C. Han and B. Han, "Phase-shifting in achromatic moiré interferometry system," *Optics express,* vol. 15, pp. 9970-9976, 2007.

[69] K. Creath, "V phase-measurement interferometry techniques," *Progress in optics,* vol. 26, pp. 349-393, 1988.

[70] C. Poon, M. Kujawinska, and C. Ruiz, "Automated fringe pattern analysis for moiré interferometry," *Experimental Mechanics,* vol. 33, pp. 234-241, 1993.

[71] J. M. Huntley, "Automated fringe pattern analysis in experimental mechanics: a review," *The Journal of Strain Analysis for Engineering Design,* vol. 33, pp. 105-125, 1998.

[72] K. Okada, A. Sato, and J. Tsujiuchi, "Simultaneous calculation of phase distribution and scanning phase shift in phase shifting interferometry," *Optics communications,* vol. 84, pp. 118-124, 1991.

[73] I.-B. Kong and S.-W. Kim, "General algorithm of phase-shifting interferometry by iterative least-squares fitting," *Opt. Eng,* vol. 34, pp. 183-188, 1995.

[74] C. Wei, M. Chen, and Z. Wang, "General phase-stepping algorithm with automatic calibration of phase steps," *Optical Engineering,* vol. 38, 1999.

[75] P. T. Vianco, "Fatigue and creep of lead-free solder alloys: Fundamental properties," *ASM International,* pp. 67-106, 2005.

[76] R. Darveaux and C. Reichman, "Mechanical properties of lead-free solders," in *Electronic Components and Technology Conference, 2007. ECTC'07. Proceedings. 57th*, 2007, pp. 695-706.

[77] D. Herkommer, M. Reid, and J. Punch, "In-situ optical creep observation and constitutive modelling of joint-scale SAC solder shear samples," in *Electronics Packaging Technology Conference, 2008. EPTC 2008. 10th*, 2008, pp. 506-515.

[78] K. Mysore, G. Subbarayan, V. Gupta, and R. Zhang, "Constitutive and aging behavior of Sn3. 0Ag0. 5Cu solder alloy," *IEEE Transactions on Electronics Packaging Manufacturing,* vol. 32, pp. 221-232, 2009.

[79] C. Burke and J. Punch, "A comparison of the creep behaviour of joint-scale SAC105 and SAC305 solder samples under shear conditions," in *Thermal, Mechanical and Multi-Physics Simulation and Experiments in Microelectronics and Microsystems (EuroSimE), 2012 13th International Conference on*, 2012, pp. 1/10-10/10.

[80] M. Motalab, Z. Cai, J. C. Suhling, and P. Lall, "Determination of Anand constants for SAC solders using stress-strain or creep data," in *Thermal and Thermomechanical Phenomena in Electronic Systems (ITherm), 2012 13th IEEE Intersociety Conference on*, 2012, pp. 910-922.